Advection in photodissociation regions and its effects on the intensities of rotational lines of H(_2)O

Meltem Akyilmaz Yabaci

How to cite:

Akyilmaz Yabaci, Meltem (2008) Advection in photodissociation regions and its effects on the intensities of rotational lines of H(_2)O. Doctoral thesis, Durham University.

Advection in photodissociation regions and its effects on the intensities of rotational lines of H_2O

Meltem AKYILMAZ YABACI

A thesis submitted in partial fulfillment
of the requirements for the degree of
Doctor of Philosophy

Durham University

Department of Physics
Durham University

September 2008

Advection in photodissociation regions and its effects on the intensities of rotational lines of H_2O

Meltem AKYILMAZ YABACI

Abstract

A parameter based study has been carried out in order to investigate advection in photodissociation regions (PDRs) by using plane-parallel, semi-infinite assumption. The PDR material has been assumed to be advected from the molecular cloud towards the cloud surface with an initial flow velocity of $1\,\mathrm{km\,s^{-1}}$. The flow velocity, number density and mass density of the gas have been computed self-consistently as a function of visual extinction A_v. The total cloud size has been assumed to be $A_v = 10$ mag. The models have been constructed for the radiation and density parameters, $\chi = 10, 10^3, 10^5$ with respect to Draine field and $n_H = 10^4, 10^5, 10^6\ \mathrm{cm^{-3}}$, respectively. In addition to 9 models characterized by these parameters, another model with $\chi = 10^2$ and $n_H = 10^4\,\mathrm{cm^{-3}}$ has been studied in order to compare the results to the previously obtained by Bergin et al. (2003). The rotational line intensities of o-H_2O and p-H_2O have been computed.

The effects of advection in PDR structure, abundance profiles and line intensities of H_2O have been investigated. The lower density, lower radiation models among the models studied have been found to be effected by advection, significantly. H_2O abundance profile has been found to be effected by advection even in the models in which the PDR structure and the location of H/H_2 transition zone are the least effected compared to the other models. The intensity of o-H_2O have been found to be sensitive to the order of magnitude of the flow velocity. It is concluded that the comparison of these results to the data from future observations with Herschel HIFI can provide information about the characteristics of the flow in nonequilibrium PDRs.

This thesis includes observational work of depletion of NO in pre-protostellar cores, L1544 and L183. NO has been found to show depletion characteristics intermediate between the C-containing and N-containing species.

Declaration

I confirm that no part of the material offered has previously been submitted by myself for a degree in this or any other University. Where material has been generated through joint work, the work of others has been indicated.

Meltem AKYILMAZ YABACI
Durham, September 2008

To my husband Onur YABACI,

for his love, support and companionship.

Acknowledgements

I would like to express my deepest gratitude for the support and guidance that my supervisor Prof. David Flower has provided during the production of this thesis and the work presented here. His expertise has been great help in solving most of the problems I encountered and his understanding of the problems has been invaluable.

I am grateful to the lecturers in our Atomic and Molecular Physics Group in Durham for their support and kindness throughout the years I have been a member of the group. Most thanks should go, however, to Dr. Simon Gardiner, for his help in many cases.

I would like to thank my collaborators Prof. Malcolm Walmsley and Dr. Pierre Hily-Blant, from whom I learnt a great deal about radio observations and data reduction. It has been a great experience to have worked with them at IRAM-30m telescope site. I gratefully acknowledge my dept to Prof. Cecilia Ceccarelli, who kindly provided her escape probability code and assisted the analysis of results in the final stage calculations presented in this work. I would also like to thank Karin Öberg for providing her preliminary results which I used for comparison. I am indebted to Particle Physics and Astronomy Research Council (now Science and Technology Facilities Council) and BP for the scholarship they provided through Dorothy Hodgkin Postgraduate Award (DHPA) Scheme. The scheme has supplied financial support for my studies and several trips to summer schools and conferences.

Finally, I would like to thank my parents Hursit Akyilmaz, Yuksel Akyilmaz, my sister Melda Akyilmaz and my brother Tayfun Akyilmaz for all their understanding and encouragement for my studies. My deepest acknowledgement goes to my husband Onur Yabaci, without whom, the completion of this thesis would not have been possible. There are many more people who generously gave their support through their friendship over the time I spent in Durham and I am deeply grateful for all they have provided which made my time very enjoyable.

Contents

List of Figures

List of Tables

Chapter 1

Introduction

1.1 Interstellar medium and PDRs

The interstellar medium (ISM) of our Galaxy has long been thought to be empty. The first observational evidence of the existence of material between the stars came in 1920s. By the late 1930s, it was generally accepted that the space between stars was not empty. Although, the density of ISM is lower than that of the best vacuum environment created on Earth, today, we know that ISM contains a wide variety of chemical species in neutral, ionized, gas and solid forms and it is home to many interesting physical and chemical processes.

The star and planet formation take place in the ISM, therefore, it is one of the places to look for answers to the questions regarding the origins of life. Stars do not only form in the ISM, but they also interact with the interstellar material during their evolutionary stages. At the end of their lifetime, they deposit some or all their mass back into the ISM, enriching the molecular complexity. In addition to the atoms, there are more than 140 molecules detected in the ISM or circumstellar shells (`http://www.astro.uni-koeln.de/site/vorhersagen/molecules/`). Some of these molecules contain as many as 13 atoms and have complex structures. In addition to the interesting problems that ISM studies provide the researchers with, astronomers need more accurate information about the ISM since the radiation from the observed objects pass through the ISM before reaching the observer's detection system. For these reasons, ISM of the galaxies have become an interesting and important area of research in astrophysics in the last several decades.

According to the 3-phase model of the ISM (McKee and Ostriker, 1977), ISM is made up of four components that form the three phases, i.e., cold, warm and hot phases. Each of these are characterized by the total number density of hydrogen, $n_{\rm H}$, temperature, T, and ionization state. Cold phase is also called *Cold Neutral Medium* (CNM) and characterized by $n_{\rm H} \sim 30\,{\rm cm}^{-3}$, $T \sim 100$ K and the material it contains is mostly neutral. This phase fills a very small volume of the ISM, however, contains most of the mass of the ISM. Warm phase consists of *Warm Ionized Medium* (WIM) and *Warm Neutral Medium* (WIM). As the names imply, the components WIM and WNM have similar density and temperature with $n_{\rm H} \sim 0.3\,{\rm cm}^{-3}$, $T \sim 8000$ K, but they differ in their states of ionization. The hot phase consists of *Hot Ionized Medium* (HIM) with a low density, $n_{\rm H} \sim 3 \times 10^{-3}\,{\rm cm}^{-3}$ and high temperature, $T \sim 10^6$ K, and it fills most of the volume of the ISM.

As mentioned above, most of the ISM mass is in neutral regions. The material in the ISM interacts with the photons, i.e. the radiation, from the stars. The photodissociation regions, or photon dominated regions (PDRs) are where the material is exposed to far ultraviolet photons (FUV) ($6\mathrm{eV} < h\nu < 13.6\,\mathrm{eV}$) from stars. The molecular material interacts with FUV photons and this interaction results in photodissociation of molecules, ionization of neutral species and initiates various other physical and chemical processes. Therefore, FUV photons dominate the chemistry and thermal balance making the PDRs valuable observational tools to understand the interaction of stellar radiation with the ISM material and evolution of the neutral ISM of galaxies. This includes one important aspect of studying the PDRs, i.e., understanding the star formation process. Understanding the key processes in the evolution of star forming clouds is linked to the understanding of the effects of FUV radiation in the neutral regions, i.e., the PDRs.

Water molecule is an important coolant, therefore, it plays a key role in star formation process. It is an abundant molecule in a variety of regions including the planetary atmospheres, PDRs, molecular clouds and Galactic center. However, because of its large abundance in our own atmosphere, water is difficult to observe from ground based observing facitilities. Therefore, water has been one of the key science topics of many past and future observing facilities, the Infrared Space Observatory (ISO), the Submillimeter Wave Astronomy Satellite (SWAS), Herschel Space Observatory and Atacama Large Millimeter / submillimeter Array (ALMA).

1.2 Motivation and outline

Most PDR models are based on equilibrium assumptions, i.e., they assume steady-state, stationary conditions. However, various authors emphasized that nonequilibrium models which include advection flows are necessary in order to explain some observations (Bertoldi and Draine, 1996; Störzer and Hollenbach, 1998). Advection is defined as the flow of gas and the flow is considered to be horizontal in one dimension in the work carried out in this thesis. The self-consistent dynamics has been applied to advection in ionization fronts by Henney et al. (2005) using CLOUDY code (Ferland et al., 1998). The line intensities and excitation characteristics of H_2O have been investigated by Poelman and Spaans (2005, 2006) in the PDR context. However, to the best of our knowledge, there is no PDR model that includes self-consistent dynamics applied to the calculation of rotational line intensities of H_2O.

With the above points in mind, the work presented in this thesis includes the modelling of PDRs, investigation of the effects of advection in the PDR structure, abundance profiles and line intensities of water. PDR modelling is complex if high-level of sophistication in the input considerations is sought. Including the complex physics and chemistry, radiative transfer, self-consistent dynamics, inhomogeneous effects in a single PDR code is very demanding and complicated numerical problems arise when some simplifying assumptions are not considered. Instead of attempting to create a single code for the aims of this work, three codes have been used. Meudon-PDR code

(Le Petit et al., 2006) has been used to obtain the input information, such as initial abundances, gas temperature and photodissociation fits to H_2 and CO. Advection code developed originally by Walmsley et al. (1999) has been modified and updated in order to include self-consistent dynamics and adapt the most recent chemistry. The output of Advection code has been coupled to the escape probability code provided by C. Ceccarelli (Ceccarelli et al., 2002; Faure et al., 2007) in order to calculate the rotational line intensities of H_2O.

In Chapter 2, a review on PDRs, general characteristics, details of important physical and chemical processes are provided. This chapter also includes information about PDR modelling and the available PDR codes which participated in PDR code comparison study (Röllig et al., 2007). The molecular structure and importance of observing H_2O are mentioned in Chapter 3. Also, a brief review on past observations of H_2O is given. Since the critical density, which is defined as the ratio of Einstein-A coefficient over the collisional de-excitation rate coefficient, is high for H_2O due to the large Einstein-A coefficients, the rotational levels are not in local thermodynamic equilibrium (LTE), therefore, one needs to use Large Velocity Gradient (LVG) method in order to calculate the line intensities. To this end, the *escape probability formalism* is used. The details of radiative transfer and escape probability formalism are given in Chapter 4. Modelling advection in PDRs, the input considerations of the models developed for this work, the approach taken, the details of self-consistent treatment of dynamics and other physical and chemical considerations taken into account in the models are given in

Chapter 5. The samples from the results of test runs are shown and the abundance profiles obtained running Advection code in *stationary mode* are compared to those obtained by running Meudon-PDR code. The results obtained are presented in Chapter 6 and based on the results, the effects of advection in PDRs are discussed in Chapter 7.

In addition to the theoretical work carried out to understand the effects of advection in PDR modelling, a part of this thesis involved observational work of pre-protostellar cores L1544 and L183 to investigate the spatial variation of NO molecule in these objects. Understanding the depletion of elements in early stages of star formation is crucial to reach information about the dynamical status of the protostellar objects. NO is a key molecule in nitrogen chemistry and according to the chemical models the abundance of NO more or less reflects the OH abundance. Observing OH is difficult, therefore, the dependence of NO abundance on position in the pre-protostellar cores was investigated to understand whether NO can be suggested as a tracer. This work has been published in Akyilmaz et al. (2007). Chapter 8 includes details of this observational work and the parts from the related publication. The conclusions are summarized and suggestions for future work are listed in Chapter 9.

Chapter 2

Photodissociation regions

2.1 Introduction

Photo-Dissociation Regions or Photon Dominated Regions (PDRs) are the regions where the interstellar gas is predominantly neutral and the energy balance and/or chemistry are dominated by the far ultraviolet (FUV) photons. Historically, the early observations of the massive star-forming regions Orion A and M17 in the fine structure lines [CII] 158 μm and [OI] 63 μm by Melnick et al. (1979), Storey et al. (1979), and Russell et al. (1980, 1981) pointed to predominantly neutral gas glowing in infrared(IR), outside HII regions. However, PDRs are not only the gas lying just outside of dense, luminous HII regions in the Galaxy. PDRs extend from the relatively warm region where the elements are in ionized form to the dense molecular clouds where the radiation field from hot stars is obscured in a great extent. Occupying a broad region that has different physical characteristics, various elements in ionized, atomic and molecular forms, PDRs are observable at

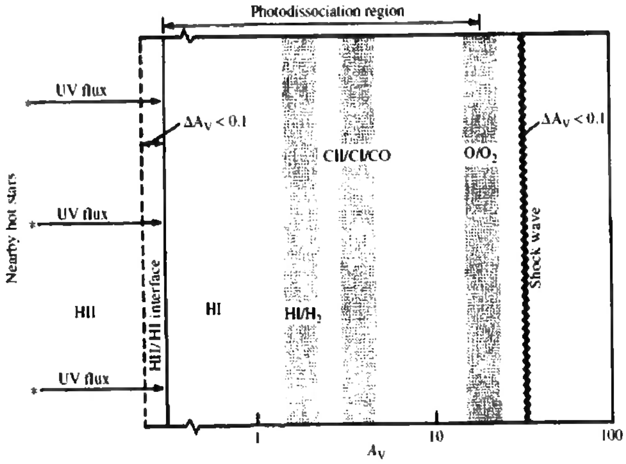

Figure 2.1: An illustration of a photodissociation region illuminated from the left by a strong FUV field. The PDR extends from the H^+/H region through the H/H_2 and $C^+/C/CO$ transitions until the O/O_2 boundary. It thus includes the predominantly neutral atomic surface layer as well as large columns of molecular gas (Tielens, 2005).

different wavelengths. Most of the nonstellar IR and the millimeter CO emission from a galaxy come from PDRs. The intense emission of [CII] 158 μm, [OI] 63 μm and 146 μm, H_2 rovibrational transitions, IR dust continuum and polycyclic aromatic hydrocarbon (PAH) emission features are examples of some of the resulting lines of photoreactions on the surfaces of interstellar clouds, (i.e., where the total visual extinction, $A_v < 1 - 3$) caused by FUV photons ($6\,\mathrm{eV} < h\nu < 13.6\,\mathrm{eV}$). In deeper regions, CO rotational and [CI] 370 μm, 609 μm transitions occur.

As illustrated in Figure 2.1, PDRs have a layered structure that consists of H, C^+ and O layers. They are often overlaid with HII gas and a thin HII/HI interface that absorbs the Lyman continuum photons. A layer of atomic hydrogen, which is also called *surface layer*, extends to a depth $A_v \sim 1 - 2$ corresponding to a hydrogen nucleus column density of $N_{\rm H} = 2-4\times 10^{21}\,{\rm cm}^{-2}$ from the ionization front. A layer of C^+ extends to a depth $A_v \sim 2 - 4$. Except for the oxygen locked up in CO, all the oxygen is in atomic form until very deep in the cloud, $A_v \sim 8$ and the layer of atomic oxygen extends to a depth $A_v \sim 10$. The PDR in the illustration is illuminated from the left by a strong FUV source, a hot star or interstellar radiation field (ISRF). The FUV flux penetrates through the PDR, causing first the ionization of the nearby species, e.g., H, C. The transition region of H^+/H is seen in the layer which corresponds to a total visual extinction value less than 0.1. In the surface layer, the temperature of the gas is higher than the dust temperature whereas deeper in the cloud dust temperature exceeds the gas temperature. The incident FUV flux is denoted by G_0 which is given in units of the average interstellar flux between $6\,{\rm eV} \lesssim h\nu \lesssim 13.6\,{\rm eV}$ of $1.6 \times 10^{-3}\,{\rm erg\,cm^{-2}\,s^{-1}}$ (Habing, 1968). G_0 usually takes values that range from the local average interstellar radiation field, i.e., $G_0 \sim 1.7$ (Draine, 1978), to $G_0 \gtrsim 10^6$. The densities n range between $\sim 10^3$–$10^7\,{\rm cm}^{-3}$ in the PDRs associated with the molecular gas (Hollenbach and Tielens, 1999).

2.2 Physical and chemical processes

2.2.1 Formation and destruction of H_2

The formation and destruction of H_2 are important because molecular chemistry is governed by the H_2, the most abundant molecule in the interstellar medium. The inefficiency of H_2 formation in the gas phase was proved in early sixties by Gould and Salpeter (1963). The formation of the interstellar H_2 mainly takes place on the surfaces of dust grains. An H atom with temperature T collides with a grain of temperature T_{gr} and sticks to the surface with a probability $S(T, T_{gr})$. The stuck H atom may migrate across the surface and find another H atom and form H_2 with a probability $\eta(T_{gr})$. Thus, the H_2 formation rate per unit volume is given by

$$R_f = \frac{1}{2} S(T, T_{gr}) \eta(T_{gr}) n_{gr} n_{\mathrm{H}} \sigma_{gr} v_{\mathrm{H}} \quad \mathrm{cm}^{-3}\,\mathrm{s}^{-1} \tag{2.1}$$

where n_{gr} is the number density of grains, n_{H} is the H atom density, σ_{gr} is the average grain cross section and v_{H} is the thermal speed of the H atoms (Hollenbach and Tielens, 1999). The formation rate derived for the interstellar clouds is given as $10^{-17} \lesssim R_f \lesssim 3 \times 10^{-17}\,\mathrm{cm}^3\,\mathrm{s}^{-1}$ (Jura, 1975), which is usually referred to as *standard rate* of formation of H_2 on the surfaces of interstellar grains. Although the above expression and the range of values for R_f are generally accepted, there have been more recent studies on observational constraints on the values of R_f in the PDRs (Habart et al., 2004; Gry et al., 2002; Tumlinson et al., 2002). Combining the FUSE results in the diffuse Chamaeleon clouds and the ISO observations of several PDRs, Habart et al. (2004) found that for a wide range of physical conditions, $1 \lesssim \chi \lesssim 10^4$, where χ denotes the scaling factor for Draine field (Draine, 1978), $100\,\mathrm{cm}^{-3} \lesssim n_{\mathrm{H}} \lesssim 10^5\,\mathrm{cm}^{-3}$, $50\mathrm{K} \lesssim T_{gas} \lesssim 600\mathrm{K}, 10\mathrm{K} \lesssim T_{dust} \lesssim 100\mathrm{K}$, H_2 forms efficiently with the rate $R_f \sim 4 \times 10^{-17}$–$1.5 \times 10^{-16}\,\mathrm{cm}^3\,\mathrm{s}^{-1}$. Habart et al. (2004) also emphasized that one of the uncertainities in their estimates might be due to the fact that steady-state PDR model was used. They suggested that the PDR models with lower H_2 formation rates but where advection is taken into account would be useful in calculating the H_2 line intensities.

The other aspects and details of H_2 formation on grains, e.g., thermal hopping, mobility of the atoms on the surface are beyond the scope of this thesis. For a model that treat the H_2 formation on grains in detail, the reader is referred to Cazaux and Tielens (2004) who also provided a review on the subject.

The main destruction mechanism of H_2 in PDRs is through the photodissociation of the molecule, which is discussed in Section 2.2.3 within the context of photodissociation of the interstellar molecules.

2.2.2 Heating and cooling

In order to determine the local temperature in a PDR, energy balance needs to be taken into account. Energy balance in PDRs is determined by the equilibrium between the heating and cooling terms. The major heating mechanisms are the photoelectric heating and the collisional de-excitation of vibrationally excited H_2.

Photoelectric heating process involves the small grains and polycyclic aromatic hydrocarbons (PAH). The role of photoelectric emission from grain surfaces in converting the FUV photon energy into the gas kinetic energy was studied by a number of authors (Watson, 1972; de Jong, 1977; Draine, 1978; Tielens and Hollenbach, 1985). The photoionization of PAHs by the FUV photons was studied by Lepp and Dalgarno (1988); Puget and Leger (1989); Verstraete et al. (1996). FUV photons are absorbed by small grains or PAHs creating energetic electrons with energies up to several eV. If these electrons diffuse in the grains, reach the surface and overcome the work function W of the grain, which is the binding energy of electrons to the grain, and any Coulomb potential ϕ_c if the grain is positively charged, they escape the grain with excess kinetic energy, thus, heat the surrounding gas.

Formation, photodissociation and collisional de-excitation of the molecules are the other important heating processes in PDRs. Undoubtedly, H_2 is the major contributor to heating the gas through these processes, since it is the most abundant molecular species in the ISM. The absorption of FUV photons pumps H_2 molecules into a bound level within an excited electronic state. About 10% of the time, this process results in photodissociation as discussed in Section 2.2.3 by fluorescence back to an unbound level of the ground electronic state, delivering about 0.25 eV to the gas (Tielens, 2005). The more probable event is the flourescence back to an excited vibrational state in the ground electronic state. At high densities, collisions with H atoms leads to de-excitation which heats the gas and thermalizes the rovibrational states. The further details of the heating processes summarized above are available in Tielens (2005).

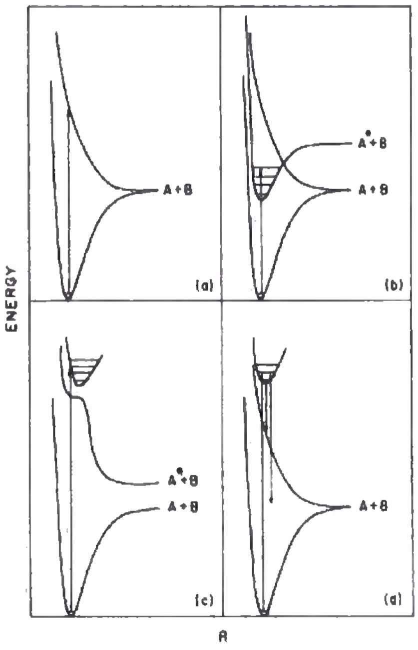

Figure 2.2: The illustration of the processes of a) direct photodissociation, b) predissociation, c) photodissociation through coupled states and d) spontaneous radiative dissociation for a diatomic molecule AB. The potential energy curves are shown as functions of internuclear distance R (van Dishoeck, 1987).

The cooling of the gas is dominated by the far-infrared (FIR) fine-structure emission lines of atoms and ions. The major coolants are [CII] 158 μm and [OI] 63 and 146 μm, [CI] 370 and 610 μm and [SiII] 35 μm emission lines (Röllig et al., 2007; Hollenbach and Tielens, 1999, and references therein).

2.2.3 Photodissociation of interstellar molecules

There is no doubt that the photodissociation of the molecules is one of the most important physical processes in the PDRs where the physics and chemistry are dominated by the FUV radiation. There are several mechanisms that lead to dissociation of molecules. These mechanisms are illustrated in Figure 2.2 for the diatomic molecules. In the simplest case, i.e., the direct dissociation process, the direct absorption from the ground electronic state into the repulsive part of an excited electronic state results in the dissociation of the molecule since spontaneous emission back into the lower state is a comparatively slow process. This mechanism is illustrated in Figure 2.2a. The indirect dissociation occurs through the discrete absorptions into bound electronic states. The spontaneous emission into the continuum of a lower-lying state may follow the absorptions into bound electronic states, as illustrated in Figure 2.2d. This is the mechanism for the photodissociation of the most abundant interstellar molecule H_2. The dissociation of polyatomic molecules occur through similar mechanisms but they are more complicated (van Dishoeck, 1987).

Photodissociation rates

For a direct photodissociation process, the rate of the photodissociation of a molecule is given by

$$k_{pd}^{cont} = \int \sigma_{ul}(\lambda) x_l I(\lambda) d\lambda \quad \mathrm{s}^{-1} \tag{2.2}$$

where subscripts u and l represent the upper and lower levels, respectively, σ is the cross section for the photodissociation, x_l is the fractional population in level l and I is the mean intensity of the radiation in photons cm^{-2} s^{-1} Å^{-1} as function of wavelength λ in Å. The rate of photodissociation by absorption into an individual level of a bound upper state u from the lower level l is given by

$$k_{pd}^{line} = \frac{\pi e^2}{mc^2}\lambda_{ul}^2 f_{ul}\eta_u x_l I(\lambda_{ul}) \quad \mathrm{s}^{-1} \tag{2.3}$$

where f_{ul} is the line absorption oscillator strength and η_u is the dissociation efficiency of the upper state level which ranges between zero and unity. Under the conditions of the interstellar medium, the radiation field is likely attenuated due to the existence of grains which scatter and/or absorb the photons. Assuming that the attenuation in the lines and continuum are separable, the photodissociation rate of an interstellar molecule through line absorption is given by

$$k_{pd} = \sum_{u,l} \frac{\pi e^2}{mc^2}\lambda_{ul}^2 f_{ul}\eta_u x_l I^{\circ}(\lambda_{ul})\theta_{ul}(N_l(X))\theta_c(A_v) \tag{2.4}$$

where $\theta_c(A_v)$ is the attenuation in the continuum at a depth A_v, θ_{ul} is the line shielding function which depends on the lower state column density N_l of species X at that depth inside the cloud (van Dishoeck, 1987). The line shielding function may be expressed by

$$\theta_{ul}(N_l) = \frac{dW_{ul}}{dN_l} / \frac{\pi e^2}{mc^2} f_{ul}\lambda_{ul}^2 \tag{2.5}$$

where W_{ul} is the equivalent width of the line in wavelength units (van Dishoeck, 1987, and references therein).

The photodissociation and photoionization rate calculations for many interstellar molecules have been carried out by various authors solving the radiative transfer equation, and the rates for the reactions are available at these sources and UMIST database.

Photodissociation of H_2

As mentioned in Section 2.2.1 the main destruction mechanism of H_2 in the PDRs is photodissociation and understanding this process is crucial in determining the structure of the atomic to molecular hydrogen transition zone. In this section, the photodissociation of H_2 will be reviewed in detail.

The photodissociation mechanism is often referred to as the Solomon process as P.M. Solomon was first to suggest the existence of a dominant destruction mechanism for interstellar H_2 initiated by photons (Osterbrock and Ferland, 2006; Draine and Bertoldi, 1996). Field et al. (1966) discussed the photodissociation of H_2 by giving the details of the molecular structure and the transition mechanisms. Stecher and Williams (1967) have estimated the photodissociation rate and discussed the importance of self-shielding of H_2. The process has been studied and reviewed by a number of authors Jura (1974), Black and Dalgarno (1977), Shull (1978), Federman et al. (1979), de Jong et al. (1980), van Dishoeck and Black (1986), Abgrall et al. (1992), Heck et al. (1992), Le Bourlot et al. (1995), Lee et al. (1996) and Draine and Bertoldi (1996). Using a time-dependent model with H_2 photodissociation including the self-shielding, the transition from atomic to molecular H_2 has been examined in order to investigate the evolutionary stage of molecular clouds (Goldsmith et al., 2007).

Figure 2.3 shows the energy level diagram of H_2, the ground state de-

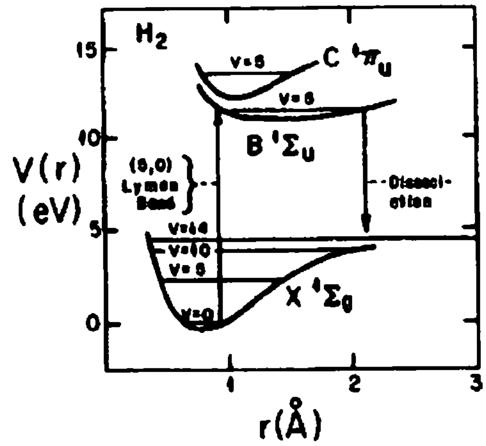

Figure 2.3: Energy level diagram for H_2 molecule. This figure also illustrates the photodissociation of H_2 by photoexcitation into excited electronic states followed by decays into unbound levels of ground electronic state (Spitzer, 1978).

noted by $X^1\Sigma_g$ and the first two excited singlet states denoted by $B^1\Sigma_u$ and $C^1\Pi_u$, respectively. The thin horizontal lines represent the vibrational energy levels for different values of vibrational quantum number v. The Lyman ($B^1\Sigma$-$X^1\Sigma$) and Werner ($C^1\Sigma$-$X^1\Sigma$) bands are two families of electronic transitions in the 912 Å–1100 Å range. Absorption of the photons in a line of one of these bands leaves the molecule in an excited state. This process is followed by decays into bound rovibrational levels within the ground electronic state $X^1\Sigma_g$ about 90% of the time and into unbound levels in the $X^1\Sigma_g$ continuum about 10% of the time[1]. The latter results in the dissociation of the molecule (Osterbrock and Ferland, 2006).

---

[1] The probability of dissociation by photoexcitation is given between 10% –15% in Tielens (2005).

Self-shielding of H_2

The photodissociation rate of H_2 is sensitive to the *self-shielding* since the FUV lines become optically thick when the H_2 column density $N(H_2)$ exceeds 10^{14} cm^{-3}. The photodissociation rate of H_2 is given by a sum of the photoexcitation rates for all levels within $B^1\Sigma$ and $C^1\Pi$ multiplied by the probability that each will be followed by a transition down to an unbound level within the ground electronic state $X^1\Sigma$. The rate R_d is approximately given by

$$R_d \approx 3.4 \times 10^{-10} \beta(\tau) G_0 \exp(-\tau_{LW}) \quad \mathrm{s}^{-1} \tag{2.6}$$

where G_0 denotes the radiation field to which PDR is exposed, $\beta(\tau)$ is the escape probability that takes into account the Lyman-Werner band self-shielding and τ_{LW} is the optical depth within these bands (Osterbrock and Ferland, 2006).

2.2.4 PDR chemistry

Similarly to various other processes that take place in photodissociation regions, PDR chemistry is governed by the FUV photons interacting with the atomic and molecular gas. FUV radiation heats the gas supplying the energy for endothermic reactions and initiates the processes of photoionization and photodissociation. PDR chemistry has been studied in detail by a number of authors: Sternberg and Dalgarno (1995), Tielens and Hollenbach (1985), van Dishoeck and Black (1988), Hollenbach et al. (1991), Fuente et al. (1993); Fuente et al. (2005), Le Bourlot et al. (1993), Jansen et al. (1995), Lee et al.

(1996), Bakes and Tielens (1998), Walmsley et al. (1999), Savage and Ziurys (2004) and Teyssier et al. (2004). One common aspect of the PDR chemistry shown by these models is the existence of several distinct chemical zones also confirmed by the observations (Jansen et al., 1995). These zones are controlled by specific sets of gas-phase reactions (Sternberg and Dalgarno, 1995). The sizes and locations of the different zones are determined by the cloud density, the intensity of FUV radiation and the gas-phase elemental abundances.

The distinct layers are, in order of cloud depth, HI zone and H/H_2 transition layer, CII and SII zones and SiII and SI Zones. The first zone and layer exist at the outer edge of PDRs where the gas temperature may exceed 1000 K in dense clouds. In hot gas, hydrogen is mainly atomic and the endothermic reactions take place which initiate the oxygen, nitrogen and sulphur chemistries. CII zone is generally more extended than the HI zone due to the self-shielding of the H_2 molecules. Si is ionized by the photoreactions and charge exchange reactions with S. SiII and SI layer is present deeper in the cloud, i.e., this layer is more extended than CII or SII layers. Sternberg and Dalgarno (1995) present a detailed discussion of the PDR chemistry as well as the sets of reactions that dominate each layer for a model where the assumed density is $n = 10^6\,\mathrm{cm}^{-3}$ and the radiation intensity scaling factor is $\chi = 2 \times 10^5$.

2.3 PDR models

Modelling the photodissociation regions have attracted a considerable interest from astrophysicists as PDRs are valuable observational tools. In order to interpret the observed line intensities, input from theoretical models is necessary. To this extent, many PDR models have been developed over last several decades. The first numerical quantitative model was presented by Black and Dalgarno (1977) and Black et al. (1978). The advances in computer technology allowed the astrophysicists involved in PDR modelling to develop more sophisticated computer codes which could treat the problems specific to the astrophysical region of interest. In this section, PDR models will be reviewed with an emphasis on the PDR codes participated the *code comparison-benchmarking* study held in Leiden, 2004. The common model inputs, i.e., model geometries, chemical and physical considerations will be described.

2.3.1 Model geometries

PDR models usually consider plane-parallel or spherical geometries chosen conveniently for the problem of interest. Most PDR models assume a plane-parallel geometry, illuminated from one side only or from both sides of the cloud. In order to investigate the physics and chemistry of a PDR that has a layered structure, this geometry provides simplified and efficient treatment of radiative transfer problem. The plane-parallel, semi-infinite slab models have been successful in studying the conversion of FUV radiation into the atomic and molecular line emission, however, taking into account the

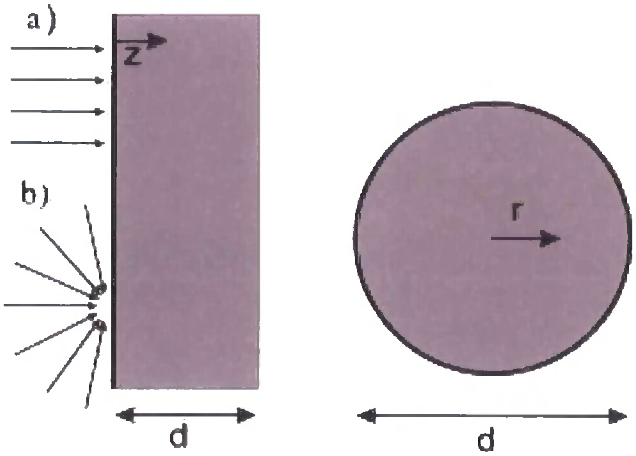

Figure 2.4: Most commonly used geometrical setups for PDR models, plane-parallel or spherical. The illumination can be assumed a) uni-directional b) isotropic (Röllig et al., 2007).

spherical geometry may be necessary for more realistic description of PDRs in multiphase clouds where the dense clumps are embedded (Störzer et al., 1996).

Figure 2.4 illustrates the common assumptions for the geometry of a model PDR. The choice between the directional and isotropical illumination effects the attenuation with optical depth (Röllig et al., 2007). For plane-parallel models, the cloud can be assumed to be illuminated either on one side or on both sides. The illumination can be considered to be uni-directional or isotropic. For spherical models, assuming uni-directional illumination breaches the spherical symmetry giving rise to numerical complications. Thus, isotropic illumination is assumed for spherical PDR models.

The dust scattering and clumpy clouds are other considerations that some PDR models take into account.

2.3.2 Physical considerations

In addition to geometrical classification, the PDR models are often classified as steady-state, stationary or time-dependent and nonstationary. Initially, the models were constructed with steady-state, stationary assumption. Steady-state, stationary models ignore any flow through the PDR and consider thermal and chemical balance[2]. This assumption holds when the timescale for formation of H_2 on grains is short compared to the dynamical timescale or the time scales for a rapid change of significant amount in FUV flux. Time-dependent effects on chemical abundances and temperature in a PDR may be significant in several cases. A strong FUV radiation source, for example, an O or B star suddenly turning on in a cloud or a photodissociation shell expanding around the central star of a planetary nebula or clumps moving in PDRs producing rapid shadowing effects are examples of such phenomena (Hollenbach and Tielens, 1999). The flow of the neutral gas through a PDR may introduce nonstationary effects on the overall structure of the PDR if the time scale of the flow is short compared to the chemical time scales for formation and destruction of the chemical species. Such effects are the main interest of this thesis and therefore advection will be discussed in more detail in Chapters 6 and 7.

---

[2] These models sometimes are called *equilibrium* PDR models.

Other main considerations are thermal balance and radiative transfer. The local temperature of the cloud is determined by taking into account the equilibrium between heating and cooling terms. Heating and cooling in PDRs have been covered in Section 2.2.2. The most common method in solving the radiative transfer problem is the escape probability method which is discussed in Chapter 4. Gas temperature can be assumed to have a fixed value or can be varied. Dust temperature is also important as the rates of some grain reactions depend on the dust temperature. Cosmic ray ionization rate, correlation of visual extinction with total column density of hydrogen $N_{\mathrm{H_{total}}}$, photodissociation and formation rates of H_2 are among other considerations in PDR modelling.

2.3.3 Chemical considerations

PDR models have a set of input considerations regarding the initial abundances of chemical species and a list of chemical reactions. The standard assumptions include the rate coefficients taken from databases (e.g., UMIST) and initial considerations for the chemical networks and species that need to be included. The problem of interest specifies other requirements such as including PAHs, gas-grain reactions, grain surface reactions, etc. Table 2.1 summarizes assumptions regarding physical and chemical processes used in PDR code comparison study.

		Model Parameters
A_{He}	0.1	Elemental He abundance
A_{O}	3×10^{-4}	Elemental O abundance
A_{C}	1×10^{-4}	Elemental C abundance
ζ_{CR}	$5 \times 10^{-17}\,\mathrm{s}^{-1}$	CR ionization rate
A_v	$6.289 \times 10^{-22}\,N_{\mathrm{H_{total}}}$	Visual extinction
τ_{UV}	$3.02A_v$	FUV dust attenuation
v_b	$1\,\mathrm{km\,s}^{-1}$	Doppler width
$D_{\mathrm{H_2}}$	$5 \times 10^{-18}.\frac{\chi}{10}\,\mathrm{s}^{-1}$	H_2 dissociation rate
R	$3 \times 10^{-18}T^{1/2}\,\mathrm{cm}^3\,\mathrm{s}^{-1}$	H_2 formation rate
$T_{\mathrm{gas,fix}}$	$50\,\mathrm{K}$	Gas temperature for constant temperature models
$T_{\mathrm{dust,fix}}$	$20\,\mathrm{K}$	Dust temperature for constant temperature models
n	$10^3, 10^{5.5}\,\mathrm{cm}^{-3}$	Total density
χ	$10, 10^5$	FUV intensity, Draine (1978)

Table 2.1: The most important model parameters used in PDR code comparison study as given in Röllig et al. (2007).

2.3.4 PDR codes

As outlined in the previous sections, there are many input parameters and initial considerations taken into account in PDR modelling. The choice of parameters and accompanying assumptions depend heavily on the astrophysical region and process of interest. This fact gives rise to the existence of variety of PDR codes designed for specific tasks. Each code has its own input sets and initial assumptions that require very detailed treatment for some processes while compromising from the same level of sophistication for others. This may lead to the discrepancy in the output results of different PDR codes, although they are all capable of providing the set of information desired by their developers. The reasons that lead to the divergence in the outputs from different models needed to be understood to obtain the same output for the same input set using different models, and therefore, to produce reliable model outputs for interpretation of the observational data from future facilities. In order to tackle this goal, a PDR-benchmarking workshop was held in Leiden, Netherlands in 2004 and the results are presented recently by Röllig et al. (2007). The important characteristics of the participating codes are reviewed briefly in Appendix A. The reader should note that there is a broad range of choices for input that determines the characteristics of a PDR code and the ones outlined here are only the most commonly referred descriptions. The output information of PDR codes is usually given as *quantity over total visual extinction* A_v or *optical depth*, except for emitted intensities, opacities at line centers and excitation diagram of H_2. Further details regarding PDR codes participated in the workshop are available at `http://www.ph1.uni-koeln.de/pdr-comparison`.

2.4 Observations of PDRs

The observations of PDRs have been reviewed extensively by Hollenbach and Tielens (1999). As mentioned in Section 2.1, PDRs can be observed at variety of wavelengths. The physical conditions in the gas can be determined by comparing the observational results to the theoretical model predictions. More recent studies on comparing the PDR models to the observations have been provided by various authors (e.g., Poelman and Spaans (2005, 2006); Bergin et al. (2003); Spaans and van Dishoeck (2001); Snell et al. (2000)) in the context of observations of H_2O. The future observations with Herschel HIFI and PACS will make it possible to explore PDRs in the wavelengths obscured to the ground-based and airborne observing facilities.

Chapter 3

Water

3.1 Introduction

Water is an important molecule for astrophysicists since it is a key ingredient in many important physical and chemical processes in a wide variety of astrophysical environments. Despite the importance of obtaining observational data for water molecules, the difficulties in observing water have limited the information available so far. The future observing facilities HIFI (Heterodyne Instrument for the Far Infrared) and PACS (Photodetector Array Camera and Spectrometer) onboard Herschel Space Observatory are expected to resolve these issues and provide the astrophysicists with the data that could not be obtained before. One of the investigations carried out for this thesis involves water and the calculations of rotational line intensities. Therefore, this chapter is devoted to the water molecule, observations and molecular structure.

3.2 Importance of observing water

H_2O is an abundant interstellar molecule which plays a key role in star formation and various other physical and chemical processes. It exists both in gas phase and solid phase in the interstellar medium of the galaxies. It has an important role in various areas of the molecular clouds, PDRs, shocked regions and accretion discs. Because it bears oxygen, which is the most abundant heavy element, H_2O is a suitable molecule for testing the astrochemistry models. Determination of its spatial distribution and its abundance is crucial in modelling the physics and chemistry of the molecular clouds. Due to its high abundance and large dipole moment it is an important coolant of the molecular gas in the interstellar medium.

The star formation takes place in cold molecular clouds where the gas is sufficiently cool for gravitational collapse to occur. Because H_2O is an important coolant of the interstellar gas, it plays an important role in the evolution of the star forming clouds and star formation process itself.

Another important characteristics of H_2O is its broad range of excitation temperatures. The lowest excitation temperature of H_2O is around 10 K and this value can be as high as 2000 K for higher levels. Therefore, it can be observed to obtain kinematical information about various regions of astrophysical interest. The energy level diagram of H_2O is illustrated in Figure 3.1.

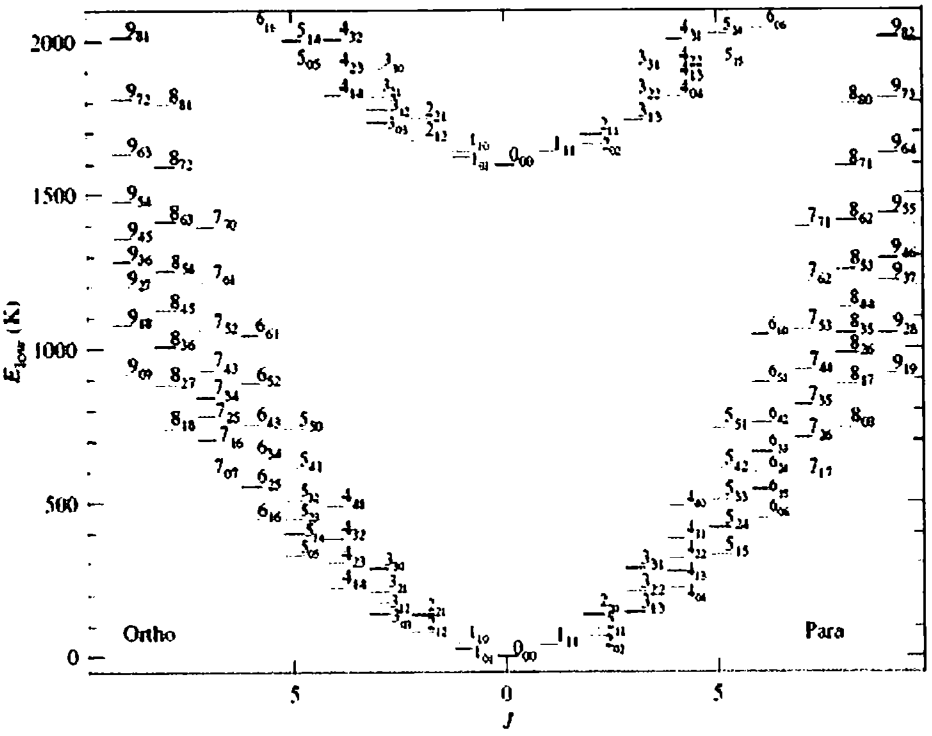

Figure 3.1: The rotational energy level diagram of ortho- and para-H_2O (Tielens, 2005). The energies of the low-lying rotational levels are shown on y-axis.

3.3 Observations of interstellar water

H_2O is one of the first interstellar molecules that was observed at radio wavelengths. The idea of observing the $6_{16} \rightarrow 5_{23}$ rotational transition dates back to 1955. This transition was observed from the directions of SgrB2, Orion Nebula and the W49 (Cheung et al., 1969, and references therein).

However, H_2O is difficult to observe from ground based instruments due to its large abundance within our own atmosphere. The H_2O existent in Earth's atmosphere blocks the lines originating between low-lying rotational levels and hence becomes a major difficulty in observing the H_2O from the ground-based facilities.

Several attempts were made to observe interstellar H_2O by using airborne facilities. In order to investigate whether the oxygen in molecular clouds is locked up in gas-phase H_2O Knacke et al. (1988) observed the $1_{01} \rightarrow 2_{02}$ line of H_2O at $3801.42\,\mathrm{cm}^{-1}$ by the NASA Kuiper Airborne Observatory which reached 12.5 km altitude. They have reported the detection of interstellar H_2O in the Orion molecular cloud as well as the statistical evidence for the presence of additional weaker lines at the source.

The two ground-state rotational transitions of H_2O are impossible to observe from ground-based and airborne facilities. However, the telluric water lines become narrow enough at higher altitudes $\sim$ 40km which can be reached by stratospheric balloons. Tauber et al. (1996) carried out the first balloonborne observations of the lowest lying $1_{10} \rightarrow 1_{01}$ transition of ortho-H_2O at 557 GHz from the 'hot-core' of Orion. The emission line at this frequency was found to be optically thick implying that H_2O is abundantly present in the core of the object.

The space missions, the Submillimeter Wave Astronomy Satellite (SWAS) and the Infrared Space Observatory (ISO) made it possible to observe blocked transitions of H_2O. ISO carried out observations of water towards various objects of astrophysical interest. ISO was the first space based observational facility to use H_2O as a tool for systematic diagnosis of the physics and chemistry in the ISM and in the stellar and planetary astmospheres. The data were obtained with the Long Wavelength Spectrometer (LWS) and the Short Wavelength Spectrometer (SWS) on board the ISO. Among these studies were the observations of pure rotational H_2O absorption lines towards Orion-IRc2 (Wright et al., 2000), detection of H_2O vapor in Titan's atmosphere (Coustenis et al., 1998) and in the upper atmospheres of Saturn, Uranus and Neptune (Feuchtgruber et al., 1997), detection of far-infrared rotational emission lines of H_2O vapor towards giant and supergiant stars (Neufeld et al., 1999; Tsuji, 2000, 2001), the discovery of widespread H_2O vapor absorption in the $2_{12} \rightarrow 1_{01}$ 179.5 μm transition toward the Sgr B2 molecular cloud (Cernicharo et al., 1997).

Determining the abundance of gas-phase H_2O was one of the primary science goals of SWAS to provide crucial constraints on astrochemical models. SWAS has detected gas-phase H_2O in a diverse range of astronomical objects and the abundance of H_2O vapor has been found to vary by more than a factor of 10^5 (Melnick and Bergin, 2005). According to the chemical models the gas-phase H_2O accounts for most of the gas-phase O for $T > 300$ K (Elitzur and de Jong, 1978; Neufeld et al., 1995, e.g.,). At lower temperatures, the abundance of H_2O was predicted to be more than 100 times lower than that in the warmer gas. The observations are in good agreement with the models for the warm gas $T > 300$ K, however this is not the case for the colder gas $T < 30$ K. The abundance of gas-phase H_2O is 100-1000 times below the predictions of chemical models (Melnick and Bergin, 2005). For example, the abundance of H_2O vapor in star-forming regions observed by SWAS is significantly below the limits set in TMC-1 and L134N (Roberts and Herbst, 2002). Clumpiness of the molecular clouds, time-dependent chemistry and freeze-out, as well as photodissociation have been suggested to be important to explain the low abundances in dense quiescent objects (e.g., Spaans and van Dishoeck (2001); Casu et al. (2001)).

Future facility HERSCHEL will be able to provide high resolution observations of H_2O. Table 3.1 lists the rotational transitions of water which will be observed by the instruments HIFI and PACS onboard Herschel.

3.4 Molecular structure of H_2O

H_2O exists in two forms, ortho and para, which behave as two different species since they are not radiatively coupled. Two hydrogen nuclei spins are aligned,

Transition	HIFI Frequency(GHz)	PACS Wavelength (μm)
p-H_2O		
$1_{11} \rightarrow 0_{00}$	1113.343	
$2_{02} \rightarrow 1_{11}$	987.927	
$2_{11} \rightarrow 2_{02}$	752.033	
$2_{20} \rightarrow 1_{11}$		100.98
$3_{13} \rightarrow 2_{02}$		138.53
$4_{04} \rightarrow 3_{13}$		125.35
$5_{15} \rightarrow 4_{04}$		95.63
$6_{06} \rightarrow 5_{15}$		83.28
o-H_2O		
$1_{10} \rightarrow 1_{01}$	556.936	
$3_{12} \rightarrow 2_{21}$	1153.127	
$2_{12} \rightarrow 1_{01}$		179.53
$2_{21} \rightarrow 1_{10}$		108.07
$3_{03} \rightarrow 2_{12}$		174.63
$4_{14} \rightarrow 3_{03}$		113.54
$5_{05} \rightarrow 4_{14}$		99.49
$6_{16} \rightarrow 5_{05}$		82.03

Table 3.1: Transitions of gas phase p-H_2O and o-H_2O that will be observed by Herschel Space Observatory.

i.e., the total nuclear spin is one, in case of ortho-H_2O (o-H_2O) whereas they are antialigned and the total nuclear spin is zero in case of para-H_2O (p-H_2O). The ratio of nuclear spin statistical weights of ortho- and para- which is also called 'ortho to para ratio' is 3:1. Molecules can be classified based on the values of the moments of inertia. In three dimensional coordinate system, there are three moments of inertia corresponding to the rotational axes of the molecules. The axes are chosen by some set of geometrical conventions. The z-axis is chosen to be the highest order axis of rotational symmetry, the

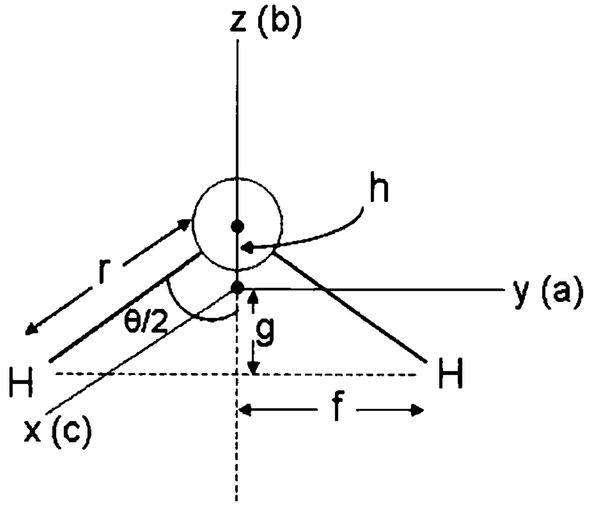

Figure 3.2: The illustration of geometrical conventions for the rotational axes for H_2O molecule. Based on Figure 6.5. of Bernath (2005).

x-axis is out of plane for a planar molecule (Bernath, 2005). The axes can also be labeled based on the magnitudes of the moments of inertia. Figure 3.2 illustrates the labeling scheme of the axes for H_2O molecule. The axes are chosen so that

$$I_A \leq I_B \leq I_C \tag{3.1}$$

holds. The values of f, g and h seen in Figure 3.2 can be calculated to be 0.7575 Å, 0.5213 Å, 0.0652 Å using the values r = 0.958 Å, θ = 104.5°,

$m_{\mathrm{H}} = 1.00$ u and $m_{\mathrm{O}} = 16.00$ u where u is the atomic mass unit. For H_2O;

$$I_A = I_y = m_{\mathrm{O}} h^2 + 2 m_{\mathrm{H}} g^2 \tag{3.2}$$

$$I_B = I_z = 2 m_{\mathrm{H}} f^2 \tag{3.3}$$

$$I_C = I_x = I_z + I_y = m_{\mathrm{O}} h^2 + 2 m_{\mathrm{H}} (g^2 + f^2) \tag{3.4}$$

The corresponding values for moments of inertia I_A, I_B and I_C are 0.6115 u Å^2, 1.148 u Å^2 and 1.760 u Å^2, respectively. The classification of polyatomic molecules based on the values of their moments of inertia is as follows:

$$\begin{array}{ll}
I_B = I_C, I_A = 0 & \text{linear molecules} \\
I_A = I_B = I_C & \text{spherical tops} \\
I_A < I_B = I_C & \text{prolate symmetric tops} \\
I_A = I_B < I_C & \text{oblate symmetric tops} \\
I_A < I_B < I_C & \text{asymmetric tops}
\end{array} \tag{3.5}$$

H_2O molecule is an asymmetric top. The rotational levels of asymmetric tops are labelled by $J_{K_a K_c}$ where J is the total angular momentum quantum number while K_a and K_c are just labels for the asymmetric tops associated with the projection of J on inertial A and inertial C axes, respectively [1]. The

---

[1] Sometimes K_{-1} and K_{+1} are used to label the asymmetric top levels because of the values that asymmetry parameter κ takes for oblate and prolate symmetric top limits.

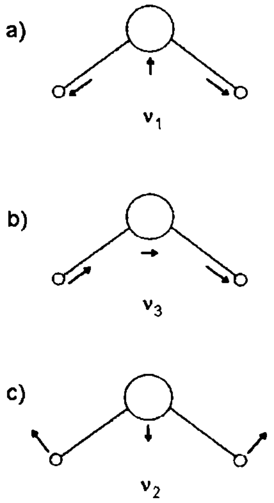

Figure 3.3: The vibrational modes of H_2O molecule. a) symmetric stretching, b) antisymmetric stretching, c) bending mode.

sum of K_a and K_c is J or $J+1$. These two become good quantum numbers only in the limit of prolate or oblate symmetric tops.

Figure 3.3 shows the three vibrational modes of H_2O molecule which correspond to the

symmetric stretching mode ν_1 3657 cm^{-1}
bending mode ν_2 1595 cm^{-1}
antisymmetric stretching mode ν_2 3756 cm^{-1} .

The calculation of rotational line intensities arising from the lower level transitions require using the escape probability formalism. For H_2O, the critical density, which is used in determining whether the collisions dominate the de-excitation process, is high ($10^8\,\mathrm{cm}^{-3}$), therefore, the level populations are not in local thermodynamic equilibrium (LTE). In order to determine the line intensities, the radiative transfer treatment is necessary. This will be discussed in more detail in Chapter 4.

Chapter 4

Radiative transfer and LVG code

4.1 Introduction

Interpreting the observed molecular line intensities require taking into account the optical depth of the observed lines and solving the radiative transfer equation. If the lines are optically thin, the local thermodynamic equilibrium (LTE) holds and the emitted flux is easily related to the line-of-sight integral of the rate of emission per unit volume of the gas. However, this is not usually applicable since most of the strong emission lines are optically thick, or, at least, they have optical depths of the order of 1, which means they may be reabsorbed in the region where they are emitted. In this case, it is necessary to solve the radiative transfer equation in order to predict the line intensities. This is usually done by using *large velocity gradient* (LVG) approximation due to the complexity of the problem. If there is a large velocity gradient in the medium, the problem is simplified as emitted photon is either absorbed locally or it escapes the medium under such conditions. The escape probability method is one of the most commonly used methods in solving the radiative transfer equations for predictions of line intensities. In this work, the LVG code developed by C. Ceccarelli (see for details, Ceccarelli et al. (2002)) has been used to calculate the flux of the transitions from rotational levels of H_2O. The concepts behind LVG approach, i.e., the radiative transfer equation and the escape probability method will be described in this chapter.

4.2 The radiative transfer equation

Consider a two-level system. In thermal equilibrium,

$$\frac{n_u}{n_l} = \frac{g_u}{g_l} \exp\left[-\frac{E_{ul}}{kT}\right] \tag{4.1}$$

where subscripts u and l denote the upper and lower levels, respectively, n is the population density, g is the statistical weight, k is the Boltzmann's constant, T is the temperature and $E_{ul} = E_u - E_l$ is the energy difference between the upper and lower levels.

The atom or molecule can undergo radiative de-excitation process through spontaneous emission or induced radiative transitions, of which the Einstein coefficients are denoted by A_{ul} and B_{ul}, respectively. The Einstein coefficient for the stimulated upwards transitions is denoted by B_{lu}. The rate of spontaneous transitions from upper to lower level per unit volume is given by $A_{ul}n_u$. The rate of induced radiative transitions per unit volume depends also on the radiation density u_ν at frequency ν of the line and it is given by $u_\nu B_{ul}n_u$. The rate of stimulated upwards transitions is $u_\nu B_{lu}n_l$. In equilibrium, the total rate of transitions from upper level to lower level should be equal to the rate of upwards transitions. That is,

$$A_{ul}n_u + u_\nu B_{ul}n_u = u_\nu B_{lu}n_l \tag{4.2}$$

The radiation density is given by a Planck distribution at temperature T,

$$u_\nu = \frac{8\pi h\nu^3}{c^3}\frac{1}{\exp[(h\nu)/(kT)] - 1} \tag{4.3}$$

where $h\nu = E_{ul}$. Using Equations 4.1 , 4.2 and 4.3 one can obtain the relationships between the Einstein coefficients:

$$B_{lu}g_l = B_{ul}g_u \tag{4.4}$$

and

$$B_{ul} = A_{ul}\frac{c^3}{8\pi h\nu^3} \tag{4.5}$$

The lines arising from the transitions between atomic or molecular energy levels are not infinitely sharp, i.e., the line profiles are determined by the physical effects such as random thermal and turbulent motions in the emitting gas. In this case, the line profile can be expressed as a *Doppler* profile

$$\phi_\nu = \frac{1}{\nu_0}(\frac{mc^2}{2\pi kT_D})^{\frac{1}{2}}\exp\left[-\frac{mc^2}{2kT_D}(\frac{\nu-\nu_0}{\nu_0})^2\right] \tag{4.6}$$

or, equivalently, a Gaussian profile

$$\phi_\nu = \frac{2}{\Delta\nu}\left(\frac{\ln 2}{\pi}\right)^{\frac{1}{2}} \exp\left[-4\ln 2(\frac{\nu-\nu_0}{\Delta\nu})^2\right] \tag{4.7}$$

where ν_0 is the frequency at the line centre, m is the mass of the atom or the molecule and T_D is the Doppler temperature (Flower, 2007). $\Delta\nu$ is the full width of the half maximum line intensity and it is given by

$$\Delta\nu = 2\nu_0\left(\ln 2/\left(\frac{mc^2}{2kT_D}\right)\right)^{\frac{1}{2}} \tag{4.8}$$

The relation between the density u_ν and the intensity of the radiation I_ν is

$$u_\nu = \frac{1}{c} I_\nu(\omega) d\omega \tag{4.9}$$

Using the above relations and the rate of transitions at frequency ν in a line, the change in the intensity of the radiation in a given direction can be found. The rate of upwards transitions at frequency ν is $u_\nu B_{lu} n_l \phi_\nu$. Similarly, the rate of stimulated transitions from upper level to lower is $u_\nu B_{ul} n_u \phi_\nu$. The change in the intensity of the radiation propagating in a given direction over an element of distance ds is given by

$$\frac{dI_\nu}{ds} = -\frac{h\nu}{c}\left[B_{lu}n_l - B_{ul}n_u\right]\phi_\nu I_\nu + \frac{h\nu}{4\pi}A_{ul}n_u\phi_\nu \tag{4.10}$$

The Equation 4.10 can be rewritten by using the relation between B_{ul} and

B_{lu} given in the Equation 4.4 as follows

$$\frac{dI_\nu}{ds} = -\frac{h\nu}{c}\left[\frac{n_l}{g_l} - \frac{n_u}{g_u}\right] B_{ul} g_u \phi_\nu I_\nu + \frac{h\nu}{4\pi} A_{ul} n_u \phi_\nu \tag{4.11}$$

The above relation is simplified by using the *opacity* κ_ν at the frequency ν in the line and the *spontaneous emission coefficient* j_ν. The opacity is

$$\kappa_\nu = \frac{h\nu}{c}\left(\frac{n_l}{g_l} - \frac{n_u}{g_u}\right) B_{ul} g_u \phi_\nu . \tag{4.12}$$

The emission coefficient j_ν is defined as the energy at a frequency ν emitted per unit time per unit solid angle per unit volume, i.e., the second term of the right-hand side of Equation 4.10

$$j_\nu = \frac{h\nu}{4\pi} A_{ul} n_u \phi_\nu . \tag{4.13}$$

Therefore Equation 4.10 becomes

$$\frac{dI_\nu}{ds} = -\kappa_\nu I_\nu + j_\nu . \tag{4.14}$$

Dividing the radiative transfer, Equation 4.10 by the opacity κ_ν yields

$$\frac{dI_\nu}{d\tau_\nu} = -I_\nu + S_\nu \tag{4.15}$$

where τ_ν is the *optical depth* at the frequency ν in the line. The *source function* S_ν is defined as the ratio of the emission coefficient to the opacity which is also named as *absorption coefficient*. The *optical depth* can be defined in terms of the opacity

$$d\tau_\nu = \kappa_\nu dx. \tag{4.16}$$

Under the conditions where thermal equilibrium applies, it is relatively easy to solve Equation 4.15 for a given intensity, since the source function S_ν simply becomes identical to the Planck function, B_ν:

$$B_\nu = \frac{2h\nu^3}{c^2}\frac{1}{\exp[(h\nu)/(kT)] - 1}. \tag{4.17}$$

However, mostly the conditions are far from thermal equilibrium and it is not easy to solve radiative transfer equation. One of the most commonly used approximations is the *escape probability method* which will be described in the next section.

4.3 The escape probability method

At any spatial point of the interstellar gas of interest, the photons are emitted, absorbed and scattered by both gas and the dust. The level populations depend on the radiation field at a given point, whereas the radiation depends on the level populations everywhere. This couples the statistical equilibrium equations with the radiative transfer equations. In order to simplify the problem one needs to decouple the statistical equilibrium equations from the radiative transfer. If the emitted photon is absorbed locally or it escapes the medium, then the local aspect of the problem is recovered. Such conditions may be present when there is a large velocity gradient in the medium. The basic idea behind this method is the introduction of a local multiplicative factor β describing the probability that a photon can escape the medium after it is emitted.

$$\beta = \frac{S_{\nu_0}(1 - e^{-\tau_{\nu_0}})}{S_{\nu_0}\tau_{\nu_0}} = \frac{1 - e^{-\tau_{\nu_0}}}{\tau_{\nu_0}} \tag{4.18}$$

Using Equation 4.16 and the relation between the source function S_ν and the opacity, the intensity of the radiation over the optical path length $d\tau_{\nu_0}$ is

$$\int j_{\nu_0} ds \equiv \int S_{\nu_0} d\tau_{\nu_0} = S_{\nu_0}\tau_{\nu_0} \tag{4.19}$$

where ν_0 is the frequency at the line centre. At distance s of the cloud, the intensity of the radiation is obtained by integrating the radiative transfer equation 4.15 at the line centre

$$I_{\nu_0} = S_{\nu_0}(1 - e^{-\tau_{\nu_0}}) + B_{\nu_0}(T_{bb})e^{-\tau_{\nu_0}} \tag{4.20}$$

where B_{ν_0} is the Planck function at frequency ν_0 and T_{bb} is the black body temperature of the background radiation field. From Equations 4.20 and 4.18, the values that β approaches in the optically thin and optically thick limits are clearly seen. In the optically thin limit, as $\tau_{\nu_0} \longrightarrow 0, \beta \longrightarrow 1 - 1/2\tau_{\nu_0}$, and $I_{\nu_0} \longrightarrow S_{\nu_0}\tau_{\nu_0} + B_{\nu_0}$, i,e., all the radiation produced within the source is emitted and the background radiation is unattenuated. In the optically thick case, as $\tau_{\nu_0} \longrightarrow \infty, \beta \longrightarrow 1/\tau_{\nu_0}$ and $I_{\nu_0} \longrightarrow S_{\nu_0}$, the radiation is reabsorbed at the point that it is emitted and the intensity of radiation becomes equal to the source function.

For a plane parallel, semi-infinite slab, the relation between the optical depth and the escape probability is given by

$$\beta(\tau) = \frac{1-\exp(-2.34\tau)}{4.68\tau} \qquad \tau < 7 \tag{4.21}$$

and

$$\beta(\tau) = \left[4\tau\left(\ln\left(\frac{\tau}{\sqrt{\pi}}\right)\right)^{1/2}\right]^{-1} \qquad \tau > 7 \tag{4.22}$$

At large optical depth, β scales with τ^{-1}(Tielens, 2005).

4.3.1 Collisional rates

In order to interpret the water line emission from observations, the detailed knowledge of collisional rate coefficients are required. The *escape probability code* used in this work to calculate the intensity from low lying rotational levels of H_2O includes rate coefficients for rotational de-excitation among the lowest 45 ortho- and 45 para- rotational levels of H_2O with both para- and ortho-H_2. The concept of collisional rate coefficient calculations is beyond the scope of this thesis, however, the reader is referred to Faure et al. (2007).

Chapter 5

Modelling advection in PDRs

5.1 Introduction

Most PDR models assume steady-state, stationary conditions and ignore advection flows. This assumption simplifies numerical modelling which is already complex if high-level of sophistication in treatment of radiative transfer and chemistry is desired. However, some famous PDRs (e.g. the one in M17 or Orion) cannot be described by equilibrium PDR models (Bertoldi and Draine, 1996) and uncertainities in explaining some processes (e.g. formation of H_2) may be due to ignoring advection flow in the models (Habart et al., 2004).

The possibility of the significant effects of advection in the structure of PDRs and molecular line intensities has been suggested by various authors. In fact, the studies of time-dependent models date back to late 1970s (Hill and Hollenbach, 1978; London, 1978). The effects of advancing H_2 front have been studied by London (1978) who concluded that advancing fronts produced larger column densities of vibrationally excited H_2 than stationary fronts. More sophisticated models were developed in last two decades to investigate the time-dependent and nonstationary effects in FUV irradiated regions of the ISM (Bertoldi and Draine, 1996; Lee et al., 1996; Störzer and Hollenbach, 1998, e.g.,). Bertoldi and Draine (1996) studied the flow of the gas through dissociation front (DF), PDR, and ionization front (IF) and highlighted the necessity of the development of models which include advection. Störzer and Hollenbach (1998) presented a parameter study of plane-parallel, semi-infinite PDRs where the IF is moving with a constant velocity and compared their results with observed data of Orion Bar. They have concluded that nonequilibrium effects are not imperative to explain the observed intensities of [CII] and [OI] fine structure lines, however, the intensities of CO low-J lines and H_2 lines can be enhanced compared to the equilibrium models.

The models by Bertoldi and Draine (1996) and Störzer and Hollenbach (1998) assumed constant velocity of either PDR material flowing towards IF/DF or IF/DF flowing through PDR. Self-consistent treatment of dynamics has been provided by Cloudy model (Henney et al., 2005; Ferland et al., 1998) to study the effects of advection in the hydrogen ionization front, on an HII region and high ionization parameter regions. Although these models differ in treatment of physical and chemical processes and the cases that they have been applied to are also different, they all agree on the emphasis on significant effects of advection in the structure and line intensities. Advection has received more attention in recent years and this was one of the points discussed in the Far-Infrared 2007 Workshop held in Bad Honnef, Germany. The future observations supporting this point, therefore, increasing the efforts in including advection in the PDR models will not be surprising.

Our approach of including the self-consistent dynamics is similar to that presented by Ferland et al. (1998) and Henney et al. (2005, 2007), however, they have applied their models in the problems of different context as mentioned above. Recent studies on line intensities and profiles of H_2O in PDRs are provided by Poelman and Spaans (2005, 2006), however, their models do not include self-consistent treatment of advection. The aim of this work has been to investigate the effects of advection of PDR material, in the structure of the PDR and in the line intensities of water for a range of density and radiation parameters.

This work has been carried out by means of a) modifying an existing PDR code to include self-consistent dynamics and updating the chemistry, b) making use of Meudon-PDR code to determine some of the input parameters c) coupling the output with an escape probability code to determine the line intensities.

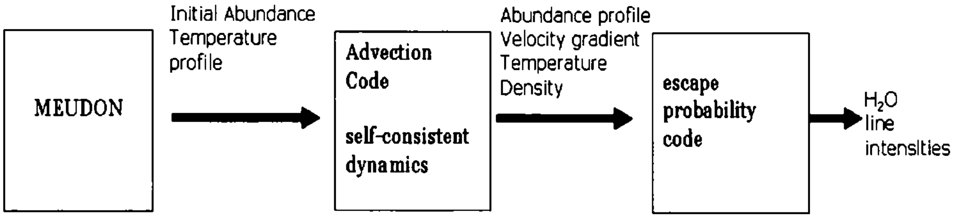

Figure 5.1: An illustration of the approach taken in this work in order to calculate the line intensities of H_2O from the PDRs where the material is advected.

5.2 Model description

The models developed here are based on the use of three different computer codes, one of which is modified and updated by the author of this thesis. As mentioned in Section 2.3.4, there is a broad range of initial considerations when setting up the input information for a PDR code. As illustrated in Figure 5.1 the approach taken here is making use of the capabilities and strengths of three codes to reach the final information desired as output, instead of attempting to develop a single code which treats the complex physics and chemistry in addition to the self-consistent dynamics. To this end, Meudon-PDR code has been run for the model parameters summarized in Table 5.1 as a first step. The input information for Advection code has been obtained using the output of Meudon-PDR code. Then, Advection code has been run for each of ten models for the low initial velocity in order to compare the abundance profiles with those of Meudon-PDR code. Fits to the photodissociation rates of H_2 and CO as functions of A_v have been obtained. After reaching the satisfactory consistency between the abundance profiles

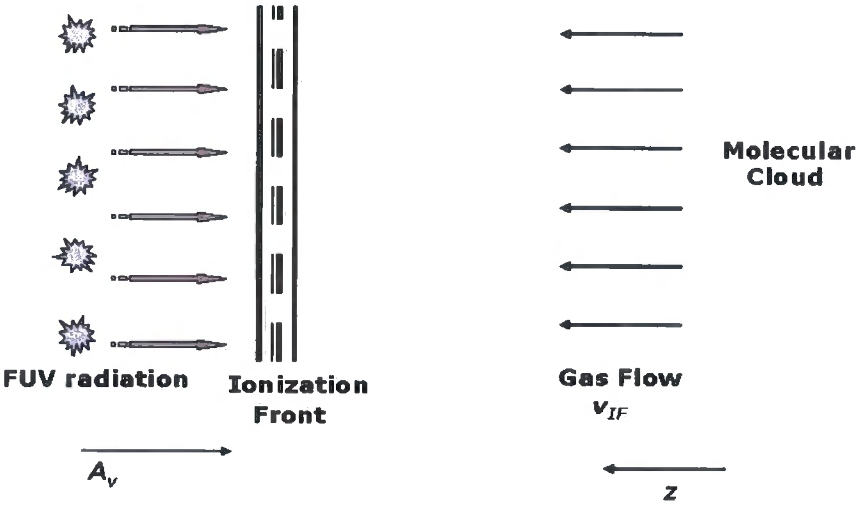

Figure 5.2: This figure illustrates a plane-parallel, semi-infinite PDR illuminated on the left side. The gas is assumed to be advected from molecular cloud and approaching ionization front with a velocity v_{IF}. The direction of movement is taken to be opposite to the direction of increasing extinction A_v.

produced by two codes, Advection code has been run for higher initial velocities. The resulting output has been coupled with escape probability code by Ceccarelli et al. (2002) in order to obtain the line intensities of H_2O for each model. In the following sections, the computational process will be described and the results will be presented in more detail.

5.2.1 Advection model

The original version of the Advection code and the assumptions that set up the model were described in Walmsley et al. (1999). The model described is similar to that adopted by Elitzur and de Jong (1978) and Störzer and Hollenbach (1998). As illustrated in Figure 5.2, a plane-parallel, semi-infinite PDR is assumed to be illuminated from one side. A unit volume of gas is assumed to be approaching the ionization front of an HII region at a constant velocity v_{IF} which is of order 1 km s^{-1} for a D-type ionization front[1]. The material is advected from deeper regions in the molecular cloud to the PDR region. The time-dependent equations for the chemical abundances are solved using a radiation field whose strength is determined by a time-dependent extinction A_v. The initial extinction is A_{v0} which is usually taken to be 10 magnitudes. The set of time-dependent ordinary differential equations are solved by the Gear method.

The original code described above, written in FORTRAN, has been modified in order to include self-consistent dynamics obtained by using the set of hydrodynamical conservation equations and the equations that come from model considerations. The set of differential equations obtained for this work and solved self-consistently are given in 5.2.2. The chemical rate equations have been modified and updated according to those in Meudon-PDR code version PDR_5II07 released in 2007. The grain size distribution has been taken into account in rate calculations of the reactions that involve grains. The input chemistry file has been updated to include a larger number of chemical species and reactions. The chemistry file *chimie06g.chi* released in Meudon-PDR, PDR_5II07 version has been adapted with a few exceptions

---

[1] D-type ionization front is where the flow velocity is subsonic at neutral end of the cloud.

discussed in 5.2.4. The minor updates to the code included the chemical timescale and rate calculations for formation and destruction of important species as well as the dynamical timescale and producing these as output information.

The original code did not include the self-consistent treatment of dynamics, the flow velocity was assumed to be constant. The core modification is the self-consistent treatment of dynamics which will be described in detail in the next section. Five differential equations were obtained for five variables total visual extinction A_v, gas temperature T, flow velocity v, number density of the gas n and mass density of the gas ρ. These equations are solved self-consistently in the modified code. The velocity gradient is calculated directly. The distance z is also calculated and listed in the output. As mentioned above, the chemistry subroutine of the code has been modified to adapt the chemical rate equations consistent with that of Meudon-PDR code.

5.2.2 Governing equations

We start with the conservation of mass. Consider a gas containing volume V enclosed by a closed surface S. The rate of change of mass in the volume V, plus the rate of outflow of mass through the surface should be equal to zero by the conservation of mass law. The rate of flow of mass into V is

$$-\int_s \rho \vec{v}.d\vec{s} \qquad (5.1)$$

where ρ is the mass density, $\overrightarrow{v}$ is the flow velocity, $d\overrightarrow{s}$ is the surface element. "$-$" sign refers to the flow which is in the opposite direction to $d\overrightarrow{s}$.

The rate of increase of mass in V is;

$$\frac{d}{dt}\int_{v}\rho dV \tag{5.2}$$

where dV is the volume element. Since V is fixed the above integral becomes

$$\int_{v}\frac{\partial\rho}{\partial t}dV$$

The summation of these two rates should be equal to zero which yields

$$\int_{v}\frac{\partial\rho}{\partial t}dV = -\int_{s}\rho\overrightarrow{v}.d\overrightarrow{s}. \tag{5.3}$$

Using the divergence theorem, one can rewrite the Equation 5.3 in the form

$$\int_{v}\left[\frac{\partial\rho}{\partial t} + \overrightarrow{\nabla}.(\rho\overrightarrow{v})\right] dV = 0. \tag{5.4}$$

This holds for any volume V. By the DuBois-Reymond Lemma, Equation 5.4 becomes

$$\frac{\partial\rho}{\partial t} + \overrightarrow{\nabla}.(\rho\overrightarrow{v}) = 0 \tag{5.5}$$

which is called the *continuity equation*. For one-dimensional flow in z-direction Equation 5.5 becomes

$$\frac{\partial\rho}{\partial t} + \frac{\partial}{\partial z}(\rho v) = 0 \tag{5.6}$$

Assuming that the first term of Equation 5.6 is equal to 0, i.e., we have steady-state case, the Equation 5.6 is reduced to

$$\frac{d}{dz}(\rho v) = 0. \tag{5.7}$$

Conservation of momentum

We have

- the rate of change of momentum inside the volume V, i.e., $\frac{\partial}{\partial t}\int_v \rho \vec{v} dV$
- the momentum flow across the surface element $d\vec{s}$.

The latter has two contributions

- the convection of momentum $\int_s \rho v \vec{v}.d\vec{s}$ and
- pressure forces $\int_s \vec{P}.d\vec{s}$ where P is the pressure.

The same argument explained when deriving the continuity equation applies here. Then we have,

$$\frac{\partial}{\partial t}\int_v \rho \vec{v} dV + \int_s \rho v \vec{v}.d\vec{s} + \int_s \vec{P}.d\vec{s} = 0. \tag{5.8}$$

Applying divergence theorem, Equation 5.8 yields;

$$\int_v \left[\frac{\partial}{\partial t}(\rho v) + \vec{\nabla}.(\rho v^2 + P)\right] dV = 0. \tag{5.9}$$

This is valid for any volume V, therefore Equation 5.9 gives

$$\frac{\partial}{\partial t}(\rho v) + \vec{\nabla}.(\rho v^2 + P) = 0. \tag{5.10}$$

For the steady-state case, the first term is zero. Rewriting the Equation 5.10 for one-dimensional flow in z-direction;

$$\frac{\partial}{\partial z}(\rho v^2 + P) = 0. \tag{5.11}$$

The pressure P can be expressed in terms of number density n, temperature T and Boltzmann's constant k_B, using the ideal gas law. Then, Equation 5.11 becomes

$$\frac{\partial}{\partial z}\left(\rho v^2 + n k_B T\right) = 0. \tag{5.12}$$

Correlation of extinction with the total hydrogen column density

The relation between the magnitude of visual extinction A_v and the total hydrogen column density N_{H} along the line of sight is given by

$$A_v = 5.35 \times 10^{-22} N_{\mathrm{H}} \tag{5.13}$$

where N_{H} is

$$N_{\mathrm{H}} = \int [n(\mathrm{H}) + 2\mathrm{n}(\mathrm{H}_2)]\, dz. \tag{5.14}$$

Combining Equations 5.13 and 5.14 one obtains;

$$A_v = 5.35 \times 10^{-22} \int n_{\mathrm{H}} dz \tag{5.15}$$

where $n_{\mathrm{H}} = n(\mathrm{H}) + 2\mathrm{n}(\mathrm{H}_2)$. Equation 5.15 can be expressed as

$$\frac{dA_v}{dz} = -5.35 \times 10^{-22} n_{\mathrm{H}}. \tag{5.16}$$

The minus sign in the last equation corresponds to the decrease in A_v as z increases, i.e., as the gas moves towards the ionization front.

Conservation of number density

In one dimension, the equation for the conservation of number density is given as

$$\frac{d}{dz}(nv) = \mathcal{N} \tag{5.17}$$

where $\mathcal{N}$ is the rate of increase of n owing to the chemistry.

Temperature

Temperature profiles (as a function of A_v) are obtained by using external fits to the temperature profile of corresponding Meudon-PDR model. Temperature of the Advection models usually takes one of the forms below or the combination of them:

$$T = \frac{T_0}{a + bA_v + cA_v^2} \tag{5.18}$$

$$T = dA_v^2 + eA_v + f \tag{5.19}$$

where T_0, a, b, c, d, e and f are simply the fit coefficients. In the models where Equation 5.18 applies at higher depths, T_0 is also the initial temperature at

A_{v_0}.

The list of the temperature profiles used for each model is given in Appendix B.

Self-consistent treatment

The equations described in the previous section can be expressed as time-derivatives by using the total time derivative given below

$$\frac{d}{dt} = \frac{\partial}{\partial t} + \overrightarrow{v}.\overrightarrow{\nabla} \tag{5.20}$$

We assume the steady-state case, i.e.,

$$\frac{\partial}{\partial t} = 0.$$

Then, the Equation 5.20 becomes

$$\frac{d}{dt} = \overrightarrow{v}.\overrightarrow{\nabla} \tag{5.21}$$

In one dimension, the Equation 5.21 becomes

$$\frac{d}{dt} = v\frac{d}{dz} \tag{5.22}$$

Let us start with the correlation of visual extinction A_v with N_{H}, Equation 5.16.

Using Equation 5.22, Equation 5.16 becomes

$$\frac{dA_v}{dt} = -5.35 \times 10^{-22} n_{\mathrm{H}} v \tag{5.23}$$

Time derivative of T is obtained directly from Equations 5.18 and 5.19, which yields

$$\frac{dT}{dt} = -\frac{T_0 \left(b \left(\frac{dA_v}{dt}\right) + 2cA_v \left(\frac{dA_v}{dt}\right)\right)}{\left(a + bA_v + cA_v^2\right)^2} \tag{5.24}$$

and

$$\frac{dT}{dt} = (2d)A_v \left(\frac{dA_v}{dt}\right) + e \left(\frac{dA_v}{dt}\right). \tag{5.25}$$

Now, applying Equation 5.22, the equation for conservation of momentum, Equation 5.12 becomes

$$v\frac{d\rho}{dt} + 2\rho\frac{dv}{dt} + \frac{k_B T}{v}\frac{dn}{dt} + \frac{k_B n}{v}\frac{dT}{dt} = 0 \tag{5.26}$$

Conservation of mass which is given in Equation 5.7 becomes

$$\frac{1}{v}\frac{d}{dt}(\rho v) = 0 \tag{5.27}$$

from which, one obtains

$$\frac{d\rho}{dt} = -\frac{\rho}{v}\frac{dv}{dt} \tag{5.28}$$

Substituting Equation 5.28 into Equation 5.26

$$\rho\frac{dv}{dt} + \frac{k_B T}{v}\frac{dn}{dt} + \frac{k_B n}{v}\frac{dT}{dt} = 0 \tag{5.29}$$

Now, using conservation of number density given in the Equation 5.17

$$\begin{aligned}\frac{1}{v}\frac{d}{dt}(nv) &= \mathcal{N}\\ \frac{1}{v}n\frac{dv}{dt}+\frac{dn}{dt} &= \mathcal{N}\\ \frac{dn}{dt} &= \mathcal{N}-\frac{n}{v}\frac{dv}{dt}\end{aligned} \tag{5.30}$$

Substituting the above equation into Equation 5.29

$$\begin{aligned}\rho\frac{dv}{dt}+\frac{k_BT}{v}\left(\mathcal{N}-\frac{n}{v}\frac{dv}{dt}\right)+\frac{k_Bn}{v}\frac{dT}{dt} &= 0\\ \frac{dv}{dt} &= \frac{\frac{k_BT\mathcal{N}}{\rho v}+\frac{k_Bn}{\rho v}\frac{dT}{dt}}{\frac{k_BTn}{\rho v^2}-1}\end{aligned} \tag{5.31}$$

Therefore, we obtain five ordinary differential equations, i.e., 5.23, 5.28, 5.30, 5.31 and 5.24, 5.25 that can be solved self-consistently for five unknowns, A_v, T, v, n and ρ. In addition to these, the time-dependent equations for chemical abundances for each species are solved, in terms of formation and destruction rates.

Some of the models have encountered a singularity problem, i.e., when the velocity becomes equal to the isothermal sound speed making the denominator of the Equation 5.31 zero or approaching zero, which is numerically very difficult to treat. The approach taken is assuming that the velocity keeps decreasing or increasing as a function of A_v, depending on its trend, as the material approaches the cloud surface. This enabled us to apply a fit to the velocity as a function of A_v effective from the point where the problem is encountered, and in this way, to obtain a velocity gradient in our output for escape probability code.

5.2.3 Meudon-PDR code

Meudon-PDR is one of the most sophisticated PDR codes available. Meudon-PDR code has been run for each model of which the basic characteristics are displayed in Table 5.1. Each model has produced abundance and temperature profiles. From Meudon-PDR output, the abundance values at $A_v = 10$ have been used as initial abundance values in the input file of Advection Code. Temperature profiles obtained from Meudon-PDR have been used to produce external fits to temperature as functions of visual extinction A_v. In addition to these, photodissociation of two most abundant molecules H_2 and CO in Advection code, have been treated using fits to the photodissociation rates as functions of A_v.

5.2.4 Physics and chemistry

The chemical processes involved in the chemistry file are listed below. The rate calculations of some reactions were adopted from Meudon-PDR code. The details of the calculations of the chemical reaction rates used in Meudon PDR are presented in Le Petit et al. (2006). The list of chemical species and reactions is also adopted from one of the chemistry files of Meudon-PDR code PDR_5II07 release, i.e., *chimie06g.chi*, with a few exceptions concerning reactions involving grains. The differences in the treatment of photodesorption of water ice are discussed in the following section. The treatment of formation of H_2 on grain surfaces also differ from that listed in Meudon-PDR chemistry file, which is described in Appendix C. The adsorption of H_2 on grain surfaces has been removed from the list as it was negligible. The list of chemical species and reactions includes the name and atomic composition of the species, the initial abundance and the enthalpy of formation in kcal mol^{-1}. The list also includes the chemical reactions, and the corresponding γ, α and β coefficients for each reaction to be used in the calculations. The photodesorption of H_2O ice has been considered to be the main destruction of solid phase H_2O, which will be referred often in the following sections. In the next section, the rate equation of photodesorption in the models will be described. The rate equations of other chemical reactions which are used in Advection Code are given in Appendix C.

Photodesorption

The rate calculation of photodesorption has been partly adopted from Meudon-PDR code. In addition to the photodesorption rate that depends on the FUV radiation, the contribution from secondary photons is taken into account in Meudon-PDR. Therefore, the total rate becomes the sum of two terms that account for contributions from radiation and the secondary photons.

$$k = \gamma\phi_{sec}\frac{\mathrm{n(H_2)}}{\mathrm{n(H)} + \mathrm{n(H_2)}}\delta^2 + Y(1 \times 10^{-8})\chi \mathrm{e}^{-2\mathrm{A_v}}\frac{\delta^2}{4}\ \mathrm{s}^{-1} \tag{5.32}$$

where ϕ_{sec} is the flux due to the secondary photons, Y is the photodesorption yield and δ is the mean distance between adjacent sites in the ice mantle which is taken to be 2.6 Å. The interactions of the cosmic rays with H_2 yield a total photon flux, ϕ_{sec}, the value of which is given as (Roberge, 1990),

$$\phi_{sec} = 1 \times 10^3 \left(\frac{\zeta}{1 \times 10^{-17}} \right) \mathrm{cm}^{-2}\,\mathrm{s}^{-1}. \tag{5.33}$$

where ζ is the cosmic ray ionization rate which is usually of the order of $10^{-17}\,\mathrm{s}^{-1}$. The photodesorption yield Y is simply taken to be equal to $\gamma = 5 \times 10^{-7}$ (see Walmsley et al. (1999)) in the test runs for comparison reasons that would allow consistency with the value in the released Meudon-PDR chemistry. In the actual runs however, Y has been taken from Westley et al. (1995).

$$Y = 3.5 \times 10^{-3} + 0.13\mathrm{e}^{-336/T_{gr}} \tag{5.34}$$

The reader is notified that there is a more recent study on the photodesorption yield of water ice by Öberg et al. (priv. comm.), however, the results of this work have not been published at the time that this thesis is being submitted. Preliminary work has been carried out in order to compare the grain temperature dependence of the photodesorption yield parameters given by Westley et al. (1995) and provided by K. Öberg , which will be presented in Section 7.2.1.

Grain temperature

The temperature of grains is discussed in detail in Hollenbach et al. (1991) and is given by

$$\begin{aligned} T_{gr} &= \left\{8.9 \times 10^{-11} \nu_0 G_0 e^{-1.8 A_v} + 2.7^5 \right. \\ &\quad +3.4 \times 10^{-2} \left[0.42 - \ln(3.5 \times 10^{-2} \tau_{100} T_0)\right] \\ &\quad \left. \times\, \tau_{100} T_0^6 \right\}^{0.2} \end{aligned} \tag{5.35}$$

where G_0 is the FUV flux in Habing units (Habing, 1968), ν_0 is the dust absorption frequency τ_{100} is the emission optical depth at 100 μm. T_0 is the equilibrium dust temperature at the slab surface due to the incident FUV field alone. T_0 is given by

$$T_0 = 12.2 G_0^{0.2}\,\mathrm{K}. \tag{5.36}$$

τ_{100} and T_0 are related as follows

$$\tau_{100} T_0^5 = 2.7 \times 10^2 G_0 \tag{5.37}$$

by taking into account the balance between the FUV flux incident on the slab surface and the outgoing flux of dust radiation from a slab of constant T_0. The reader is referred to Hollenbach et al. (1991) for derivation of the Equation 5.35.

5.2.5 Temperature profiles

Temperature is one of the important input considerations. The original code applied a fit to the temperature which assumed $T = 1000/(1 + 2A_v)$. In the modified version, the fits to the temperature profile have been obtained separately for each model using the temperature profile produced by running Meudon-PDR code for the corresponding model (see 5.2.2). The fit parameters are given in Appendix B. The plots of fits are shown in this section. For models 14, 15, 16, 24, 35, 36 the fits obtained are successful to produce temperature profiles almost identical to that produced by Meudon-PDR code as seen in Figures 5.3, 5.6, 5.9, 5.12, 5.7 and 5.10. For models 34, 54, 55 and 56, the best fits obtained produce temperature profiles which are still close to temperature predicted by Meudon-PDR code, however, these profiles have small discrepancies as seen in Figures 5.4, 5.5, 5.8 and 5.11.

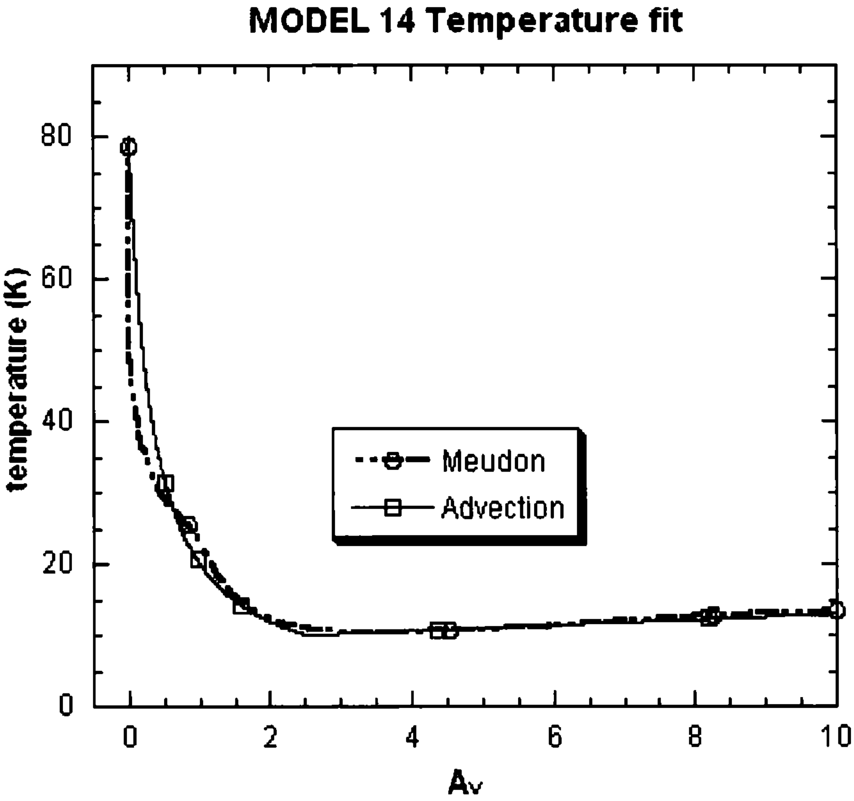

Figure 5.3: The temperature as a function of A_v for Model 14. Dashed line is the temperature produced by Meudon-PDR code. The solid line is the temperature fit obtained for Advection code.

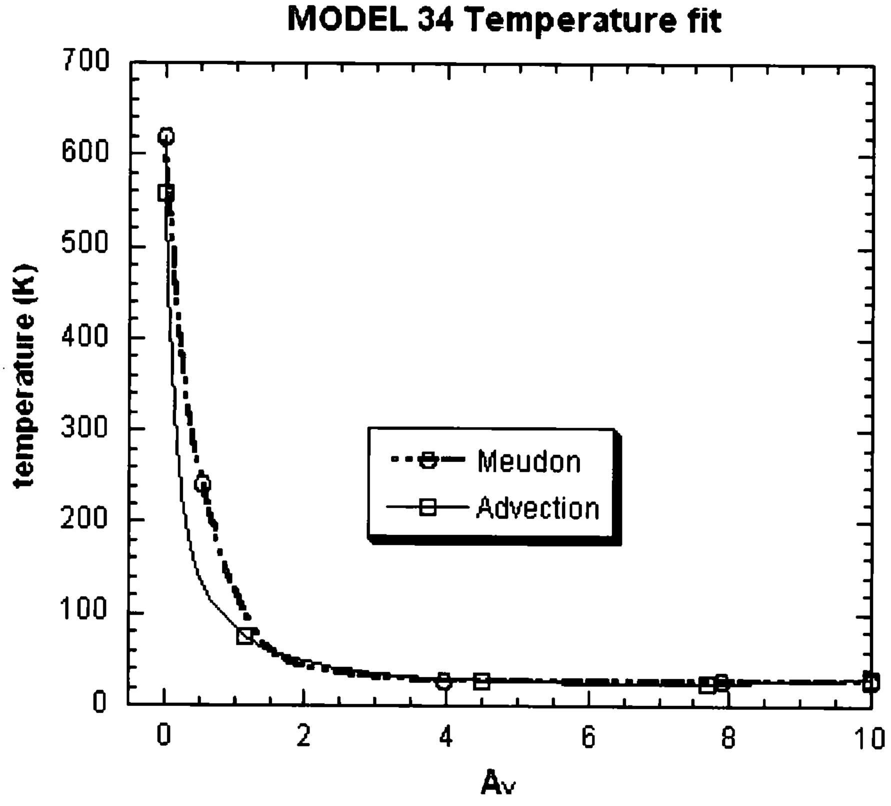

Figure 5.4: The temperature as a function of A_v for Model 34. Dashed line is the temperature produced by Meudon-PDR code. The solid line is the temperature fit obtained for Advection code.

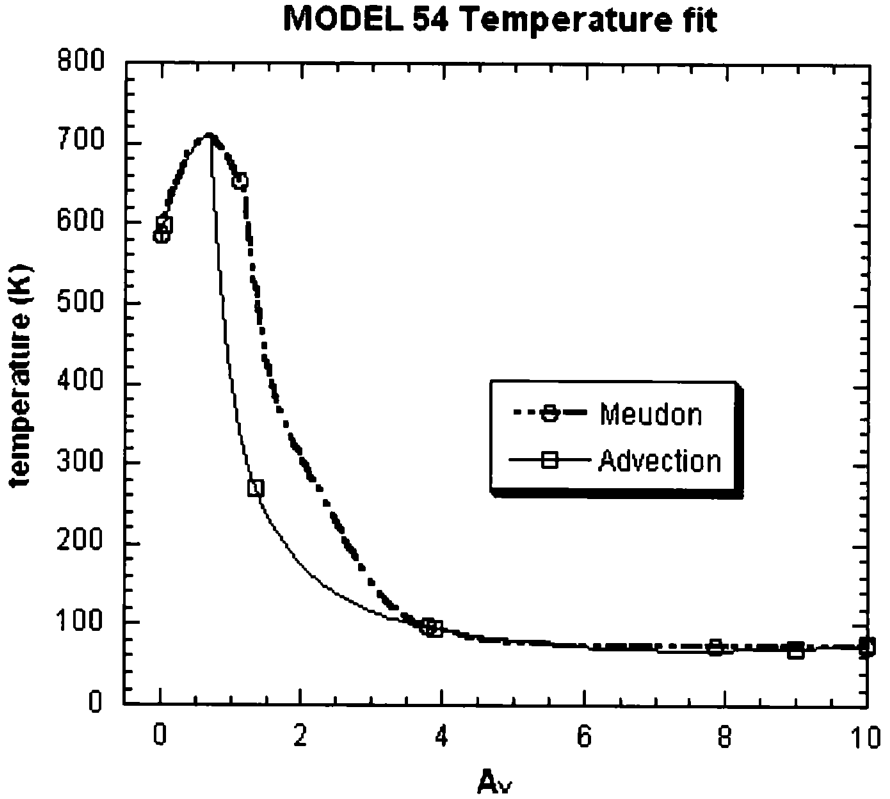

Figure 5.5: The temperature as a function of A_v for Model 54. Dashed line is the temperature produced by Meudon-PDR code. The solid line is the temperature fit obtained for Advection code.

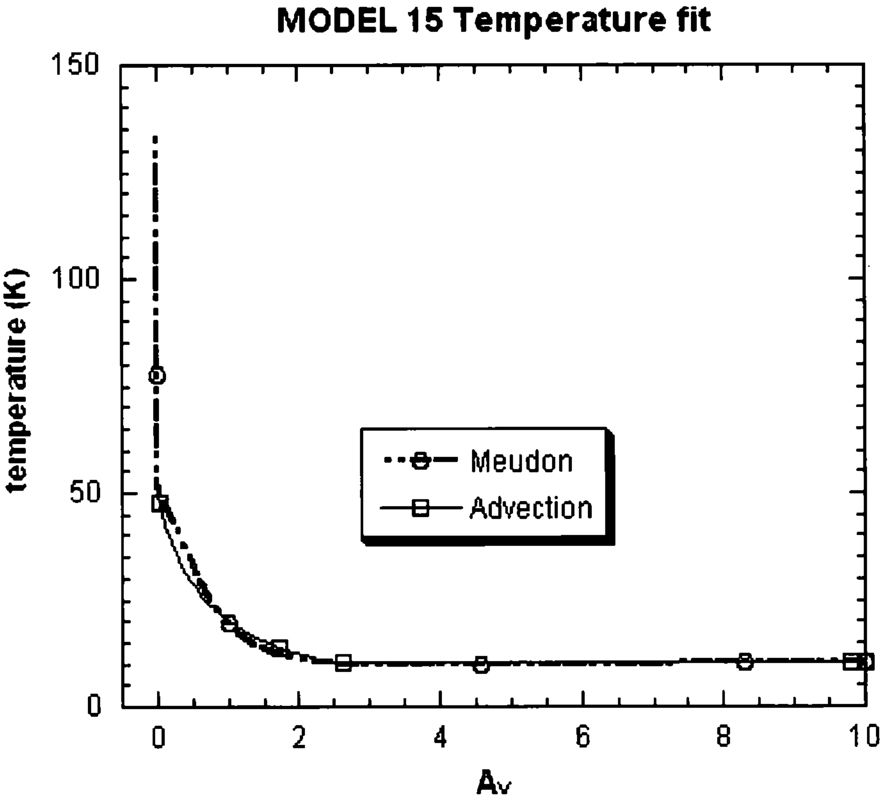

Figure 5.6: The temperature as a function of A_v for Model 15. Dashed line is the temperature produced by Meudon-PDR code. The solid line is the temperature fit obtained for Advection code.

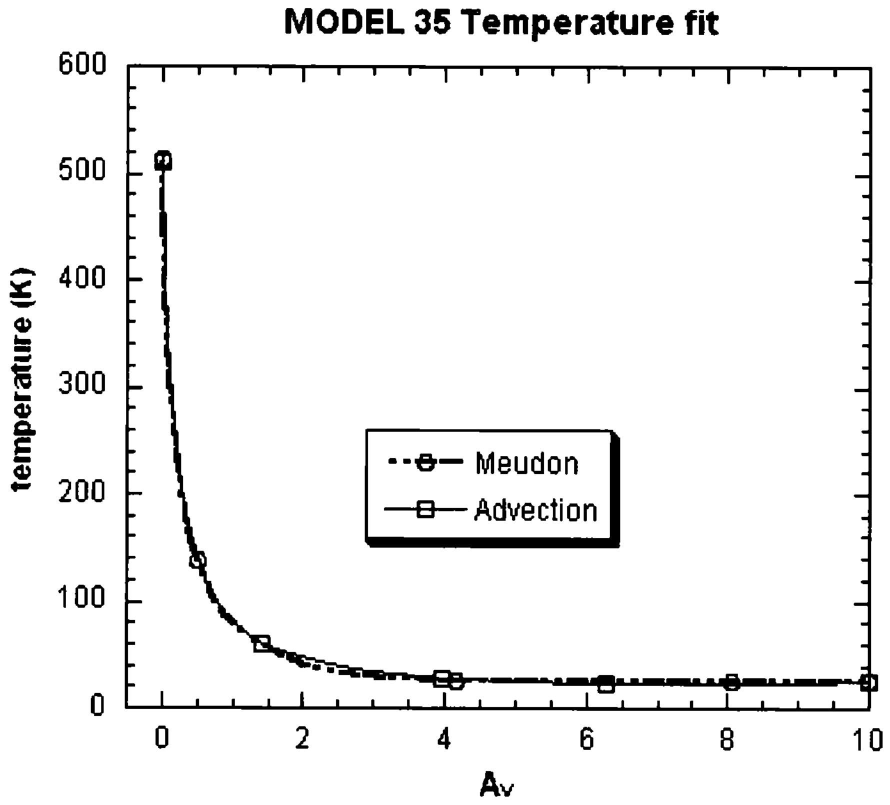

Figure 5.7: The temperature as a function of A_v for Model 35. Dashed line is the temperature produced by Meudon-PDR code. The solid line is the temperature fit obtained for Advection code.

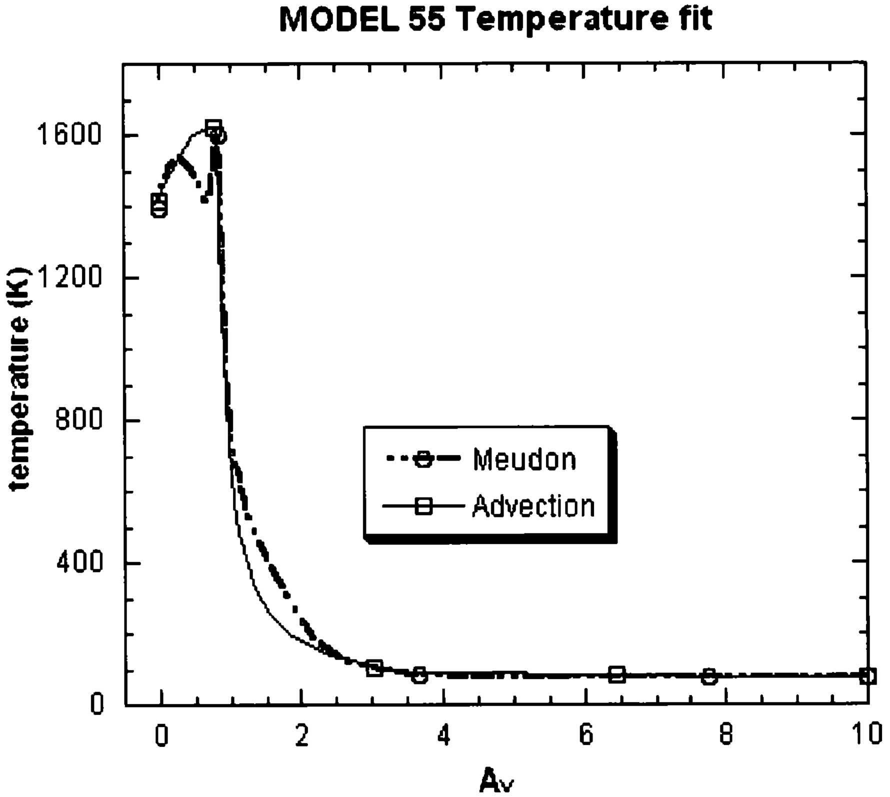

Figure 5.8: The temperature as a function of A_v for Model 55. Dashed line is the temperature produced by Meudon-PDR code. The solid line is the temperature fit obtained for Advection code.

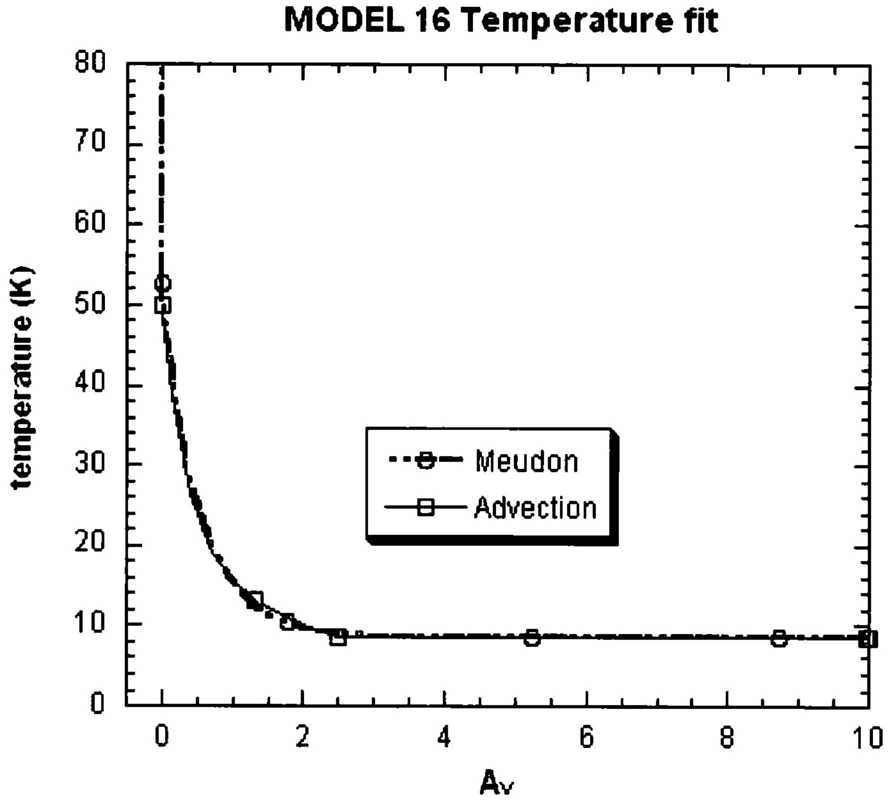

Figure 5.9: The temperature as a function of A_v for Model 16. Dashed line is the temperature produced by Meudon-PDR code. The solid line is the temperature fit obtained for Advection code.

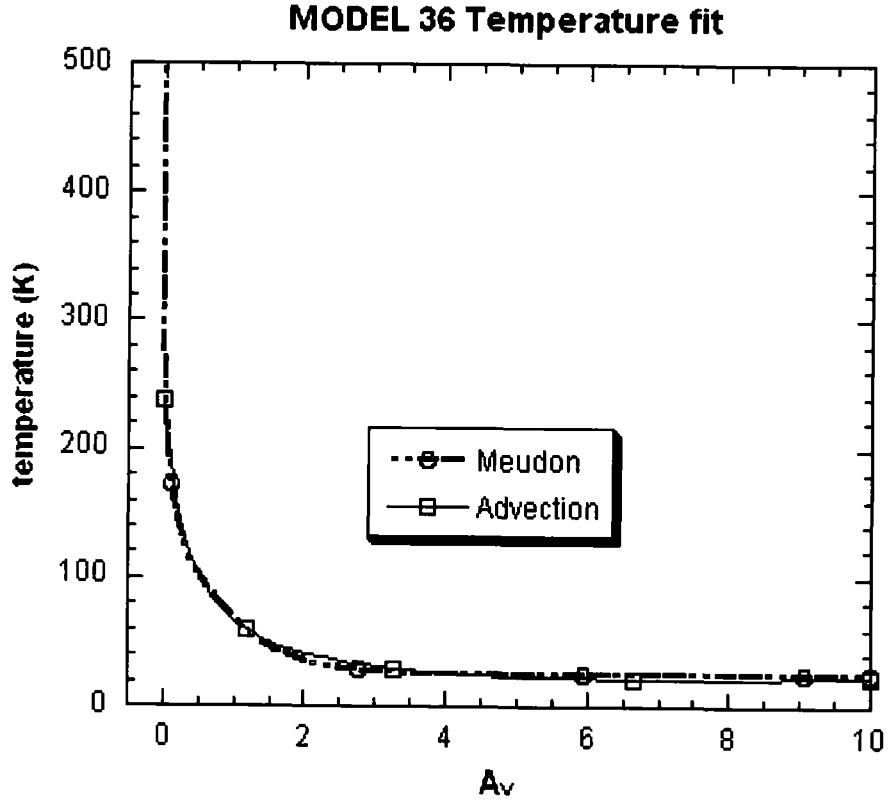

Figure 5.10: The temperature as a function of A_v for Model 36. Dashed line is the temperature produced by Meudon-PDR code. The solid line is the temperature fit obtained for Advection code.

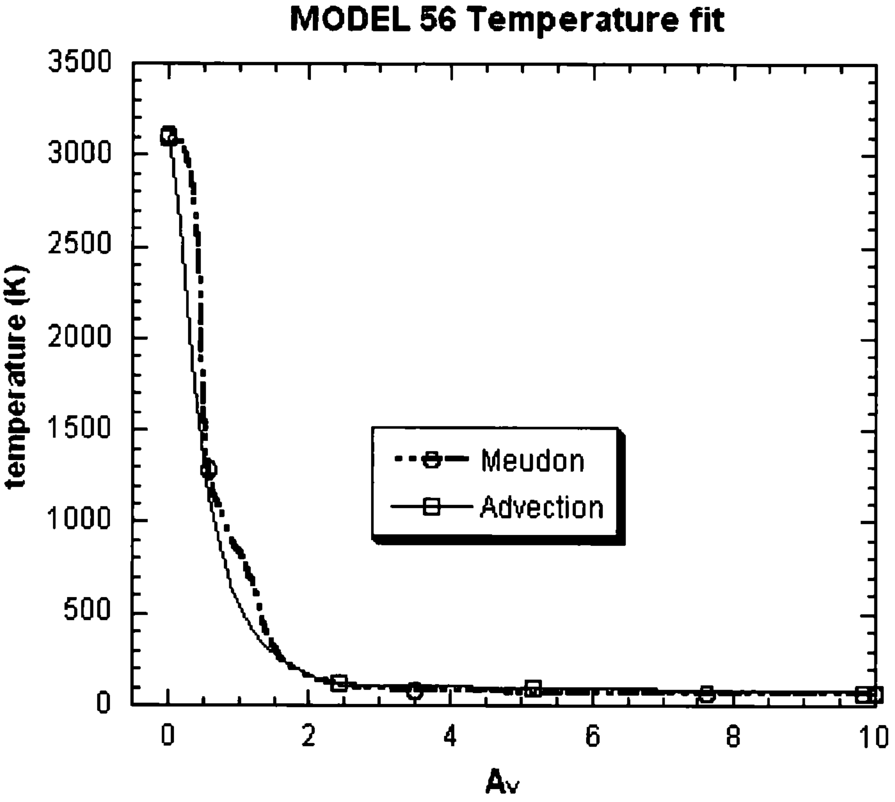

Figure 5.11: The temperature as a function of A_v for Model 56. Dashed line is the temperature produced by Meudon-PDR code. The solid line is the temperature fit obtained for Advection code.

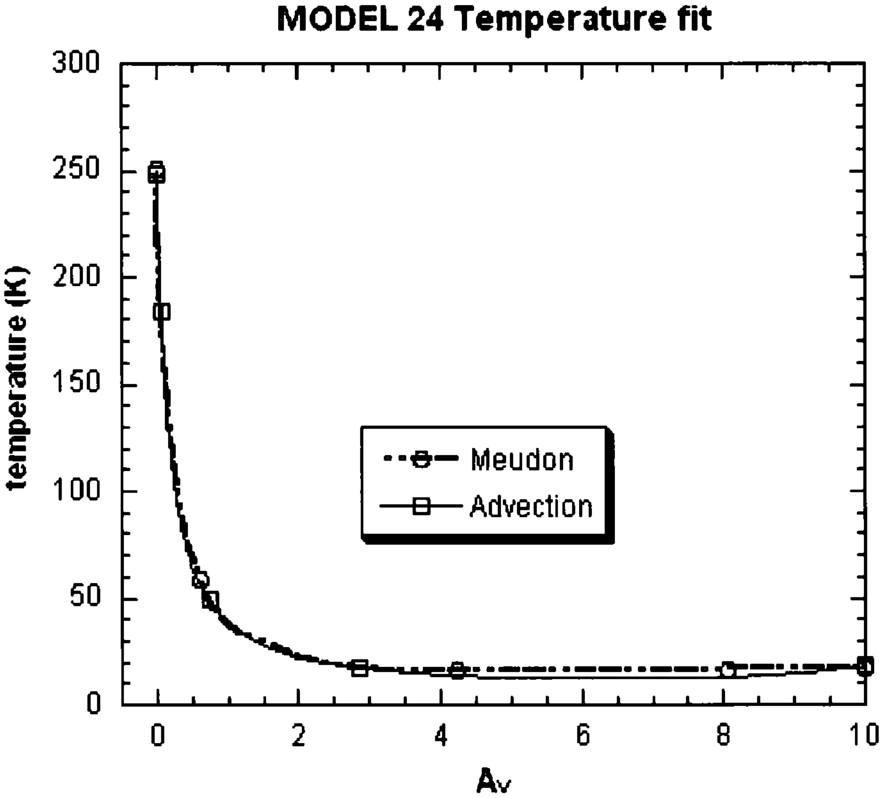

Figure 5.12: The temperature as a function of A_v for Model 24. Dashed line is the temperature produced by Meudon-PDR code. The solid line is the temperature fit obtained for Advection code.

5.3 Models

The model parameters that usually characterize the PDRs are the total number density of hydrogen n_H and the scaling factor for the amount of incident radiation, χ. The order of magnitude of these parameters are used as convention for naming the models in this work as summarized in Table 5.1.

	Models	
Model	Radiation χ	Density n_H (cm^{-3})
Model 14	10	10^4
Model 34	10^3	10^4
Model 54	10^5	10^4
Model 15	10	10^5
Model 35	10^3	10^5
Model 55	10^5	10^5
Model 16	10	10^6
Model 36	10^3	10^6
Model 56	10^5	10^6
Model 24	10^2	10^4

Table 5.1: The models and the corresponding parameters. Draine field (Draine, 1978) is used in all models and χ is the scaling factor. The order of magnitudes of the radiation and the density characterizing each model PDR are also used as convention for naming the models.

Chapter 6

Results

6.1 Comparison-Stationary mode

As mentioned before, Meudon-PDR code was used to obtain the temperature profile and photodissociation fit parameters of H_2 and CO. Also, the values of abundances of chemical species at $A_v = 10$ were obtained from Meudon output to be used as initial abundances for Advection code for each model. For test purposes, Advection code was first run with a very low initial velocity, $10^{-7}\,\mathrm{km\,s^{-1}}$, i.e., in *stationary mode.* This enabled us to compare directly the outputs of Meudon-PDR and Advection codes for consistency. For lower density, lower radiation PDR models, the agreement between the outputs of two codes were found to be good. This can be seen in Figures 6.1 and 6.2 for Model 14, in Figures 6.7 and 6.8 for Model 15, in Figures 6.13 and 6.14 for Model 16. Since the Advection code does not include the radiative transfer itself, the level of agreement between the outputs of Meudon-PDR code and Advection code is expected to be affected for the rest of the models in which the radiation is higher. For example, in Figure 6.11, where the abundance profiles of H, H_2, OH and gas phase and solid phase H_2O produced by Meudon-PDR and Advection codes are compared, it is seen that closer to the cloud surface, i.e., at low A_v, H_2 abundance does not drop in the output of Advection code. The similar behaviour is seen for C and CO, for example in Figure 6.18. The reason for these discrepancies may be due to the the lack of radiative transfer treatment in Advection code. For high density, high radiation models, reducing the initial velocity can enhance the agreement, however, this creates numerical difficulties. In general, the abundance profiles obtained by running Advection code in nonstationary mode, i.e., with an initial velocity of 10^{-7} km s^{-1} have been found to be in good agreement with the abundance profiles obtained by running Meudon-PDR code.

In this section, the fractional abundances of H species and C species produced by Meudon-PDR code and Advection code in stationary mode will be presented. The abundances are relative to $n_{\rm H} = n({\rm H}) + 2{\rm n}({\rm H}_2)$.

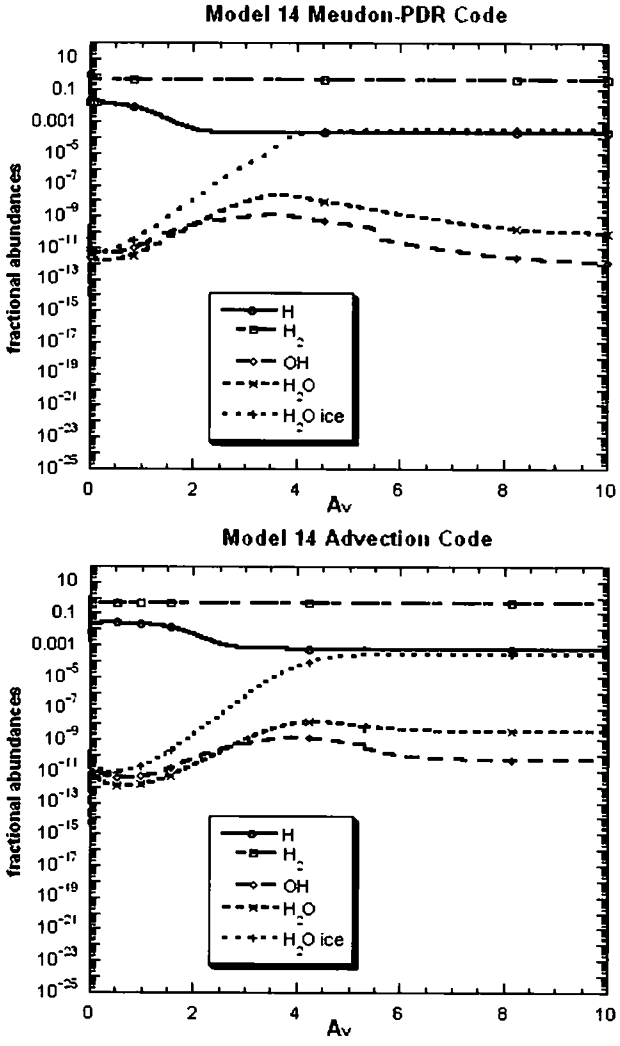

Figure 6.1: The comparison of abundance profiles of H species, gas phase and solid phase water for Model 14. Top panel shows Meudon-PDR code output. Bottom panel shows Advection code output. Advection code has been run with an initial velocity of 10^{-7}km s^{-1}. $n_{\rm H} = 10^4$ cm^{-3}.

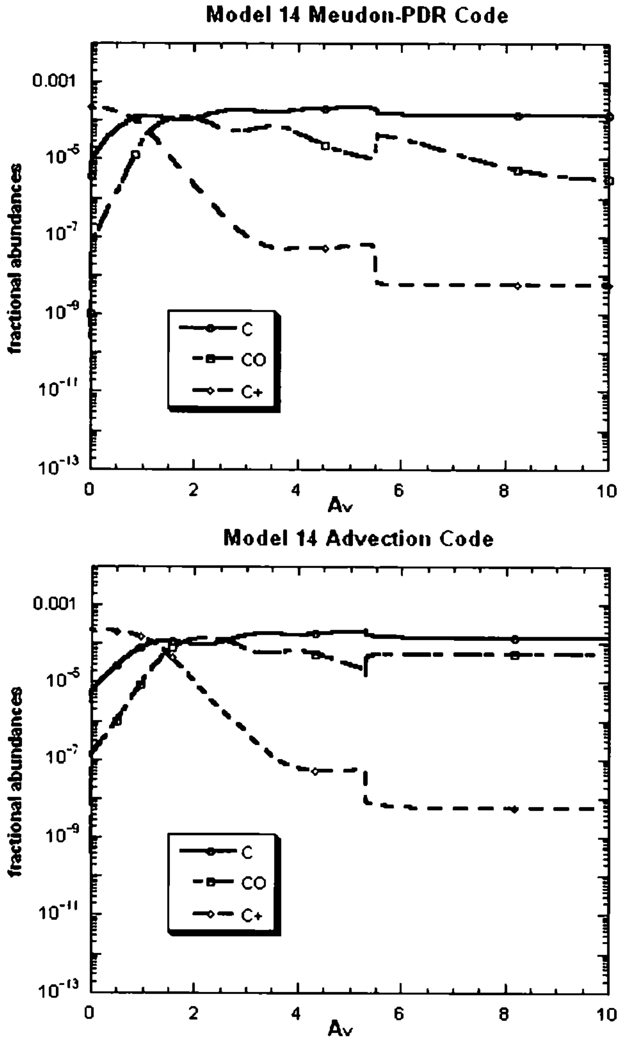

Figure 6.2: The comparison of abundance profiles of C, CO and C+ for Model 14. Top panel shows Meudon-PDR code output. Bottom panel shows Advection code output. Advection code has been run with an initial velocity of 10^{-7}km s^{-1}. $n_{\rm H} = 10^4$ cm^{-3}.

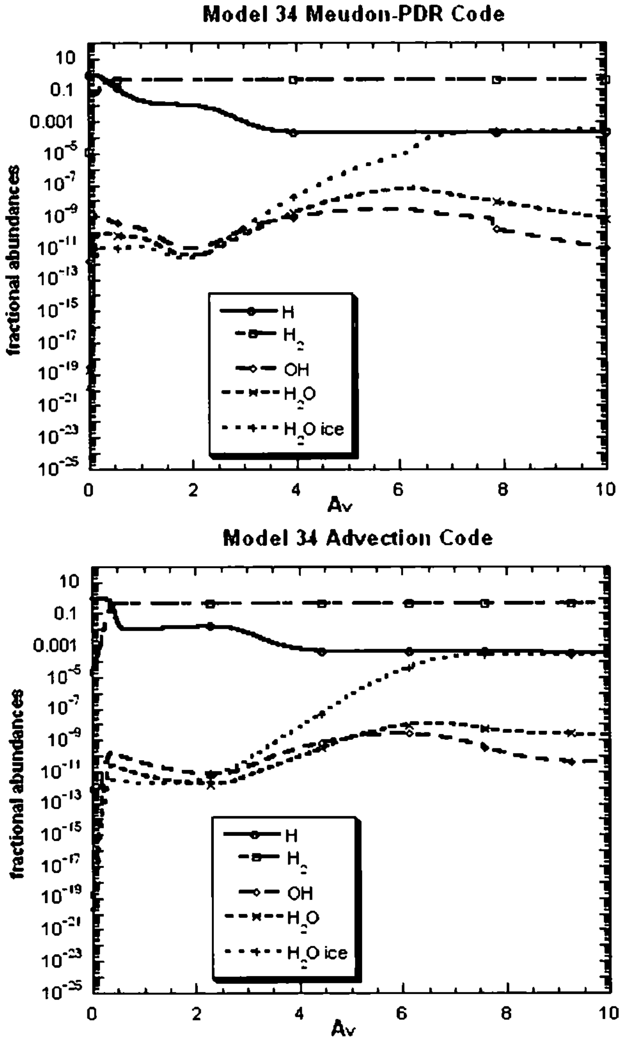

Figure 6.3: The comparison of abundance profiles of H species, gas phase and solid phase water for Model 34. Top panel shows Meudon-PDR code output. Bottom panel shows Advection code output. Advection code has been run with an initial velocity of 10^{-7}km s^{-1}. $n_{\mathrm{H}} = 10^4$ cm^{-3}.

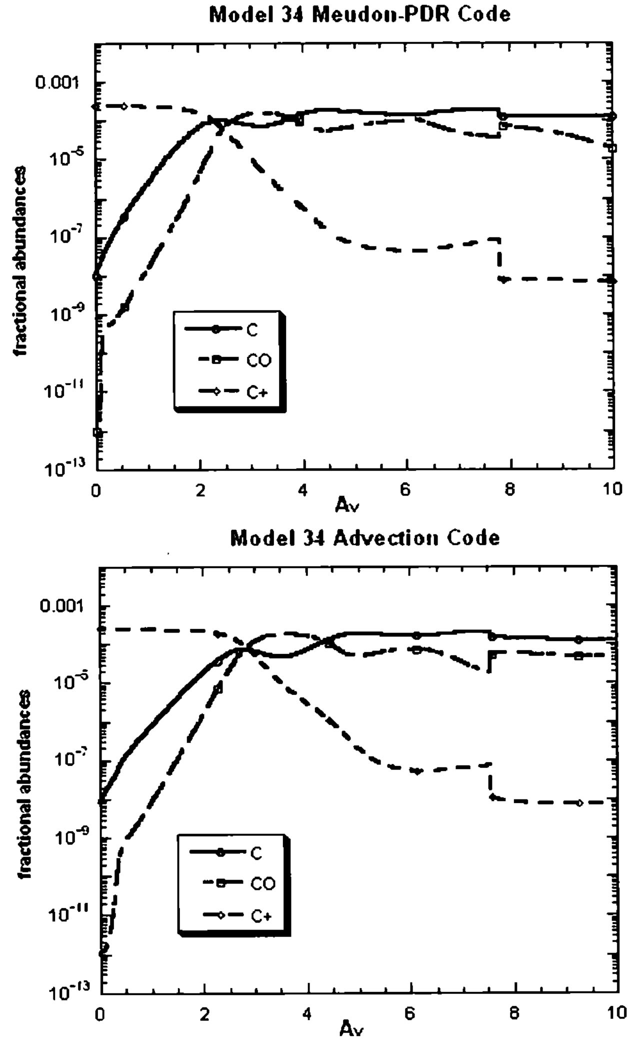

Figure 6.4: The comparison of abundance profiles of C, CO and C+ for Model 34. Top panel shows Meudon-PDR code output. Bottom panel shows Advection code output. Advection code has been run with an initial velocity of 10^{-7}km s^{-1}. $n_{\rm H} = 10^4$ cm^{-3}.

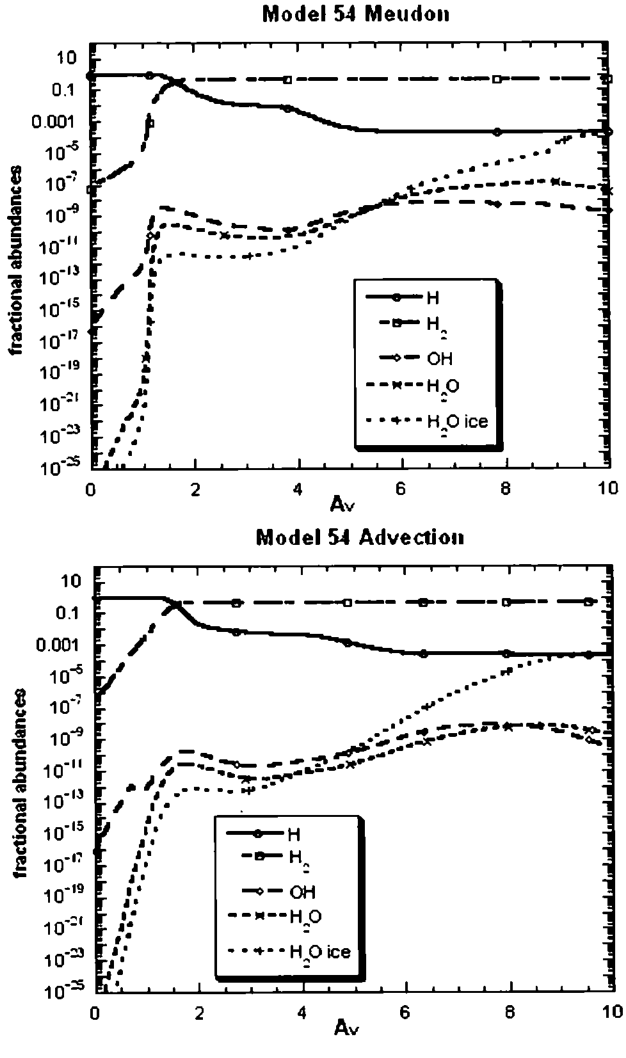
Model 54 Meudon

Model 54 Advection

Figure 6.5: The comparison of abundance profiles of H species, gas phase and solid phase water for Model 54. Top panel shows Meudon-PDR code output. Bottom panel shows Advection code output. Advection code has been run with an initial velocity of 10^{-7}km s^{-1}. $n_H = 10^4$ cm^{-3}.

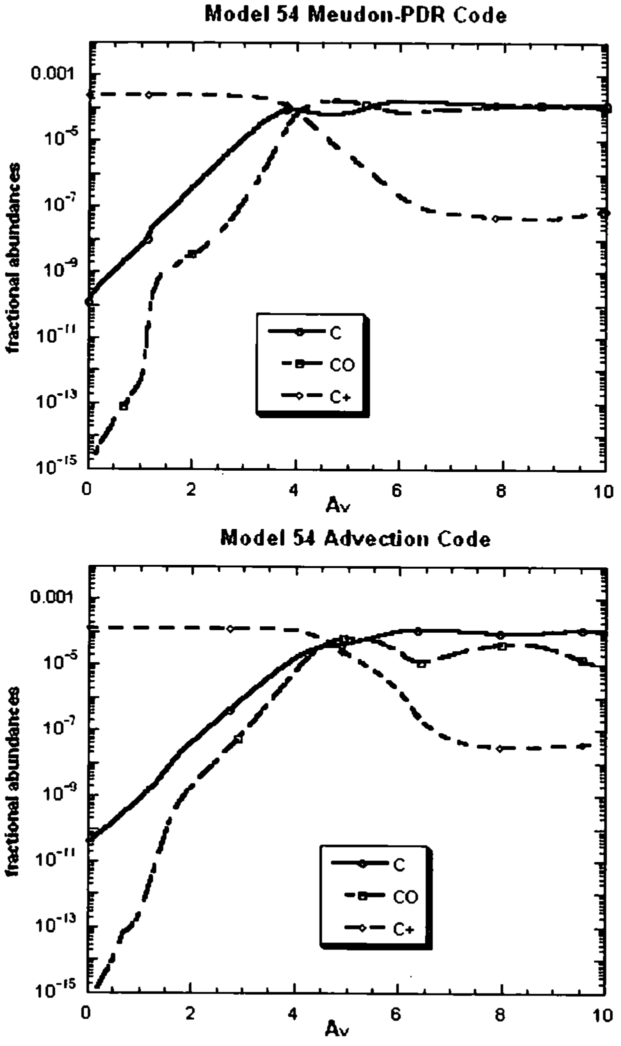

Figure 6.6: The comparison of abundance profiles of C, CO and C+ for Model 54. Top panel shows Meudon-PDR code output. Bottom panel shows Advection code output. Advection code has been run with an initial velocity of 10^{-7}km s^{-1}. $n_{\rm H} = 10^4$ cm^{-3}.

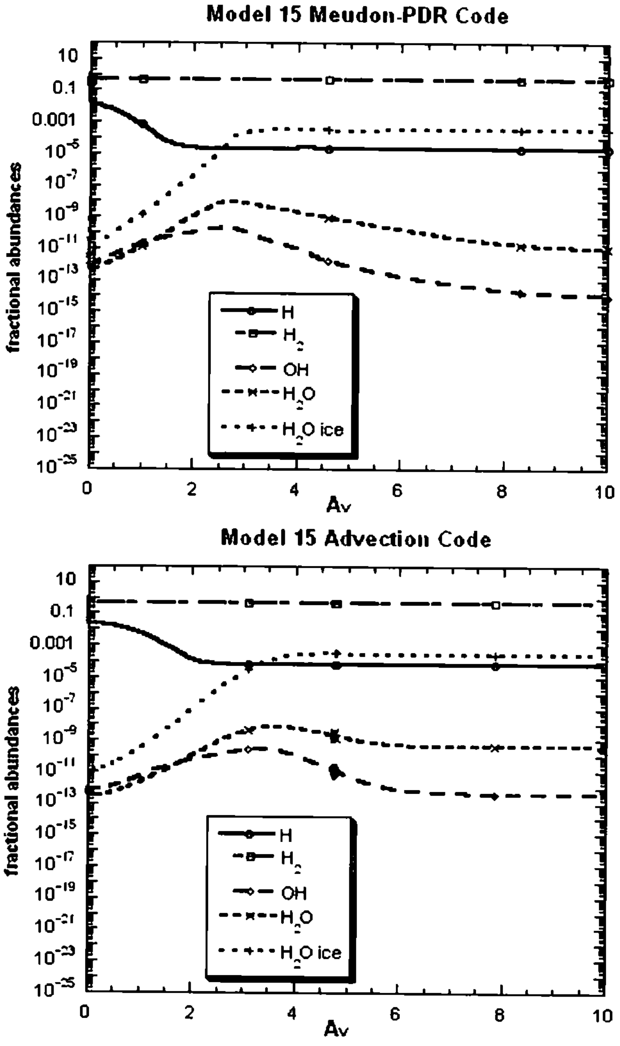

Figure 6.7: The comparison of abundance profiles of H species, gas phase and solid phase water for Model 15. Top panel shows Meudon-PDR code output. Bottom panel shows Advection code output. Advection code has been run with an initial velocity of 10^{-7}km s^{-1}. $n_{\mathrm{H}} = 10^5\,\mathrm{cm}^{-3}$.

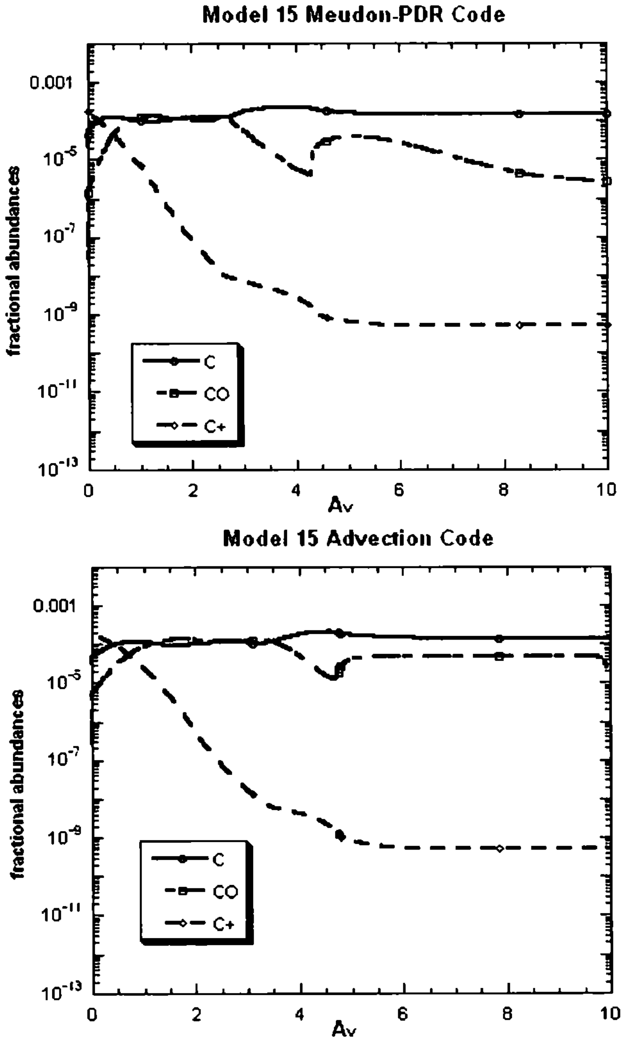

Figure 6.8: The comparison of abundance profiles of C, CO and C+ for Model 15. Top panel shows Meudon-PDR code output. Bottom panel shows Advection code output. Advection code has been run with an initial velocity of 10^{-7}km s^{-1}. $n_{\rm H} = 10^5$ cm^{-3}.

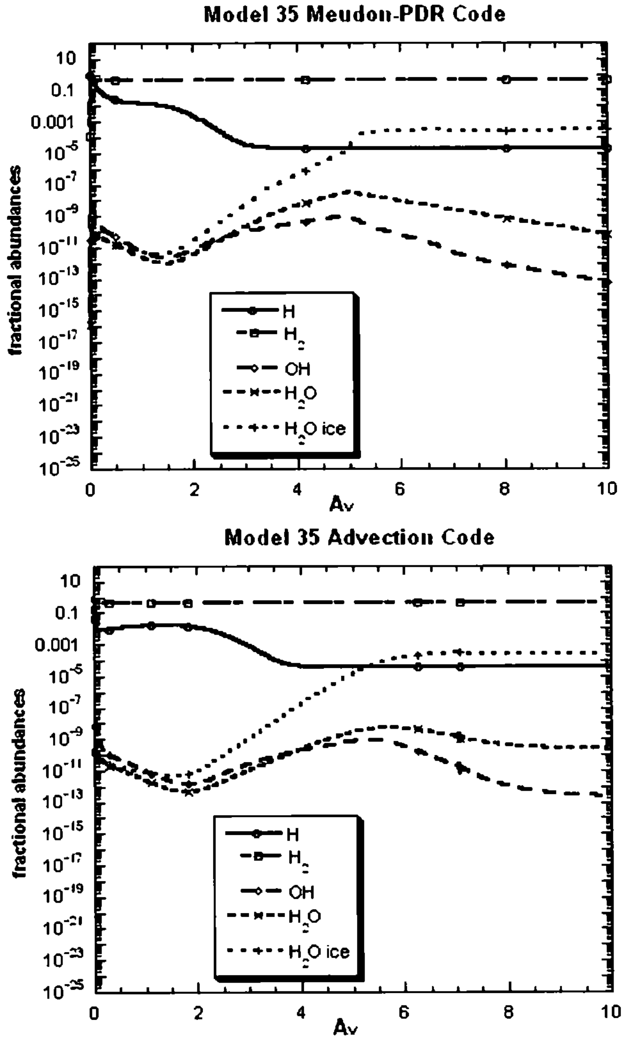

Figure 6.9: The comparison of abundance profiles of H species, gas phase and solid phase water for Model 35. Top panel shows Meudon-PDR code output. Bottom panel shows Advection code output. Advection code has been run with an initial velocity of 10^{-7}km s^{-1}. $n_{\rm H} = 10^5$ cm^{-3}.

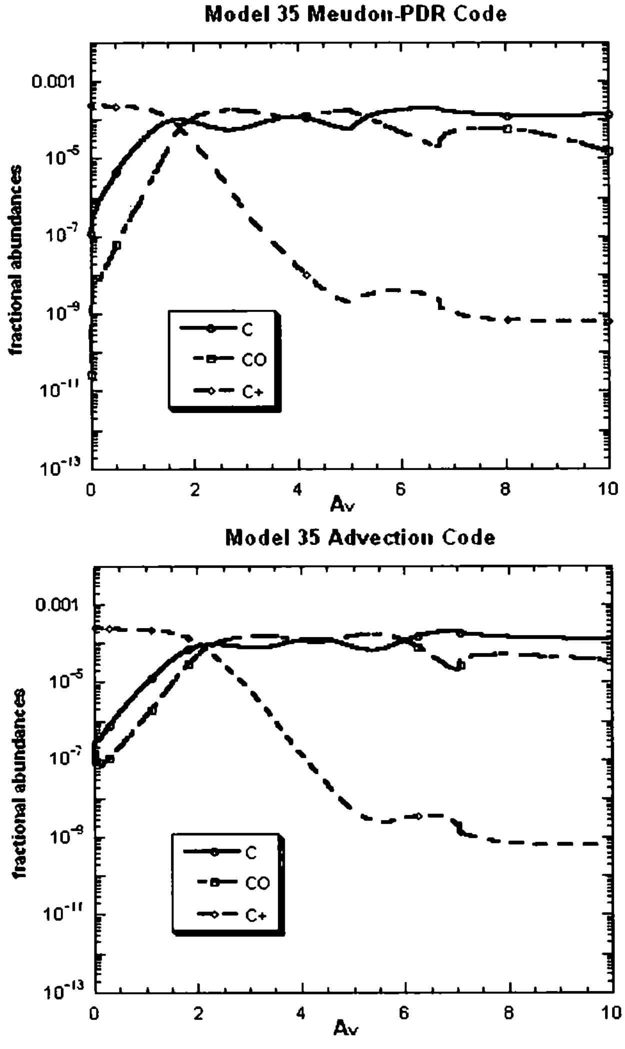

Figure 6.10: The comparison of abundance profiles of C, CO and C+ for Model 35. Top panel shows Meudon-PDR code output. Bottom panel shows Advection code output. Advection code has been run with an initial velocity of 10^{-7}km s^{-1}. $n_{\rm H} = 10^5\,{\rm cm}^{-3}$.

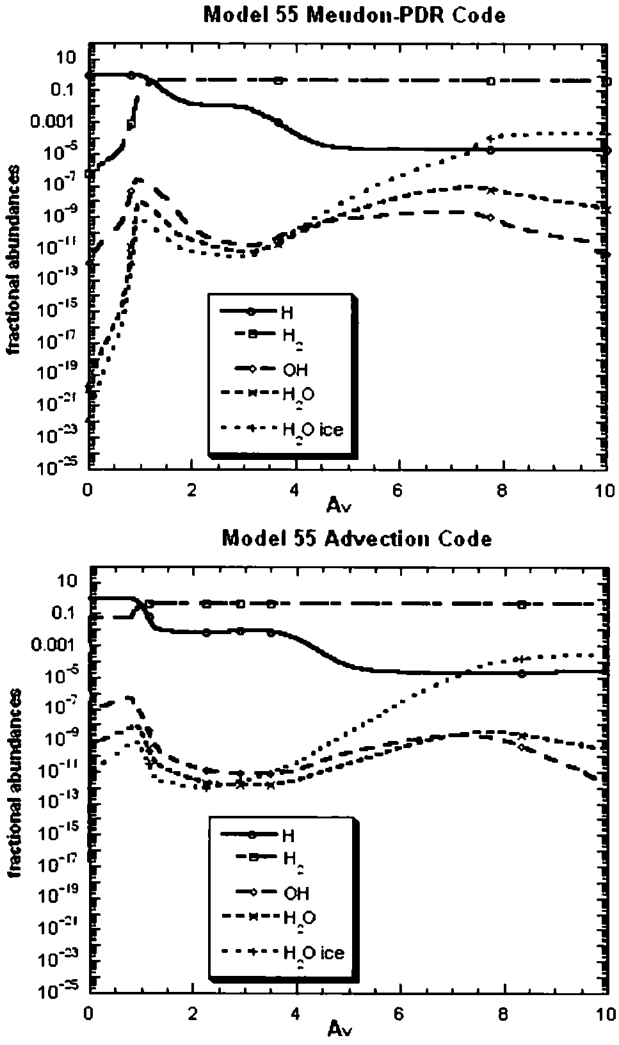

Figure 6.11: The comparison of abundance profiles of H species, gas phase and solid phase water for Model 55. Top panel shows Meudon-PDR code output. Bottom panel shows Advection code output. Advection code has been run with an initial velocity of 10^{-7}km s^{-1}. $n_{\mathrm{H}} = 10^5\,\mathrm{cm}^{-3}$.

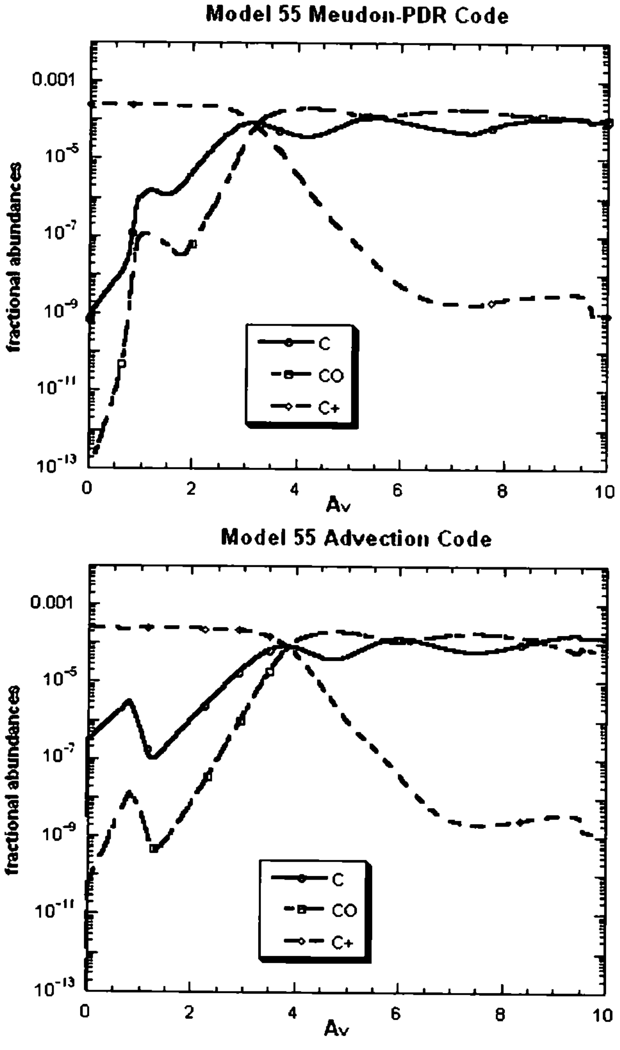

Figure 6.12: The comparison of abundance profiles of C, CO and C+ for Model 55. Top panel shows Meudon-PDR code output. Bottom panel shows Advection code output. Advection code has been run with an initial velocity of 10^{-7}km s^{-1}. $n_H = 10^5\,cm^{-3}$.

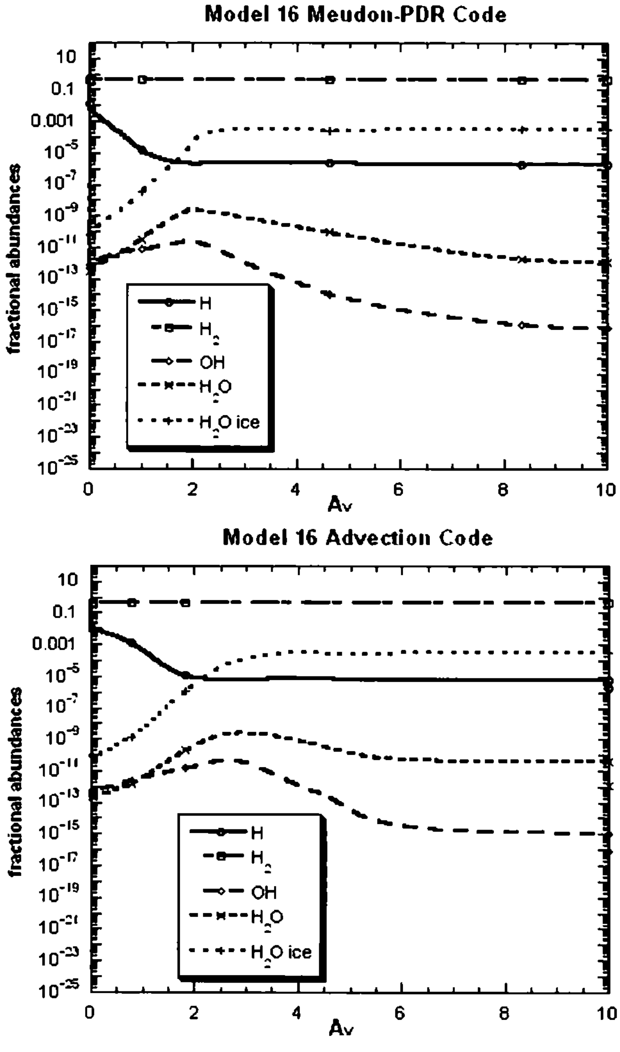

Figure 6.13: The comparison of abundance profiles of H species, gas phase and solid phase water for Model 16. Top panel shows Meudon-PDR code output. Bottom panel shows Advection code output. Advection code has been run with an initial velocity of 10^{-7}km s^{-1}. $n_{\rm H} = 10^6$ cm^{-3}.

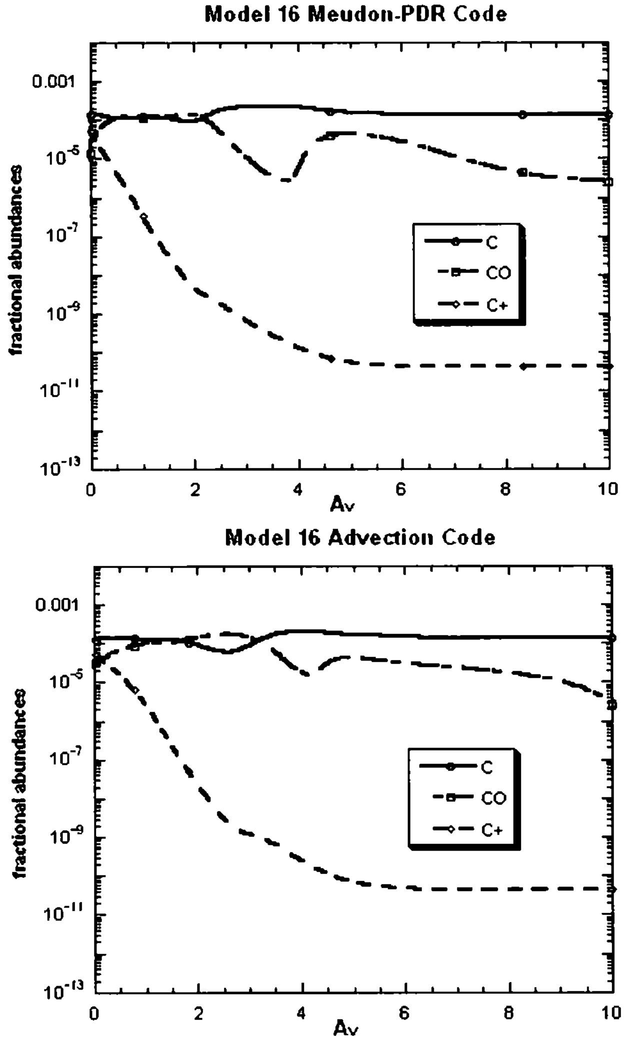

Figure 6.14: The comparison of abundance profiles of C, CO and C+ for Model 16. Top panel shows Meudon-PDR code output. Bottom panel shows Advection code output. Advection code has been run with an initial velocity of 10^{-7}km s^{-1}. $n_{\rm H} = 10^6\,{\rm cm}^{-3}$.

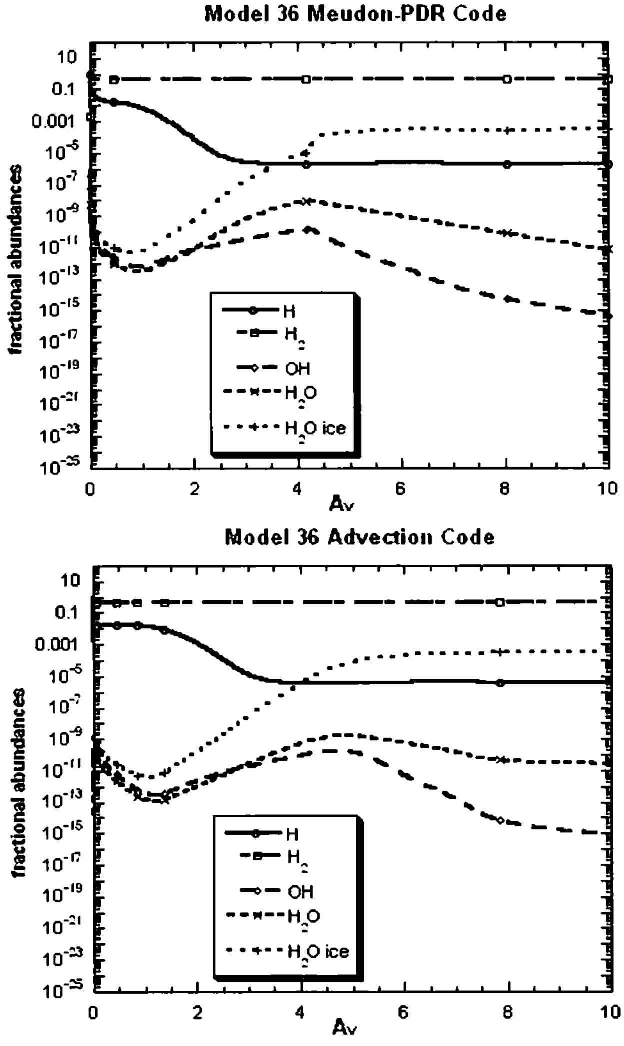

Figure 6.15: The comparison of abundance profiles of H species, gas phase and solid phase water for Model 36. Top panel shows Meudon-PDR code output. Bottom panel shows Advection code output. Advection code has been run with an initial velocity of 10^{-7}km s^{-1}. $n_{\mathrm{H}} = 10^6$ cm^{-3}.

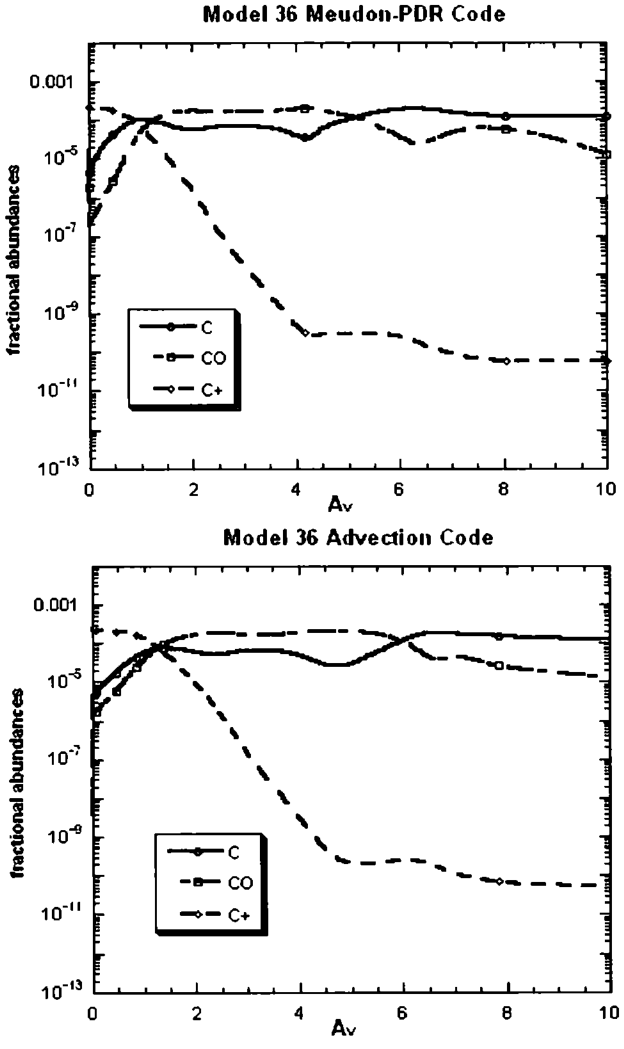

Figure 6.16: The comparison of abundance profiles of C, CO and C+ for Model 36. Top panel shows Meudon-PDR code output. Bottom panel shows Advection code output. Advection code has been run with an initial velocity of 10^{-7}km s^{-1}. $n_{\mathrm{H}} = 10^6\,\mathrm{cm}^{-3}$.

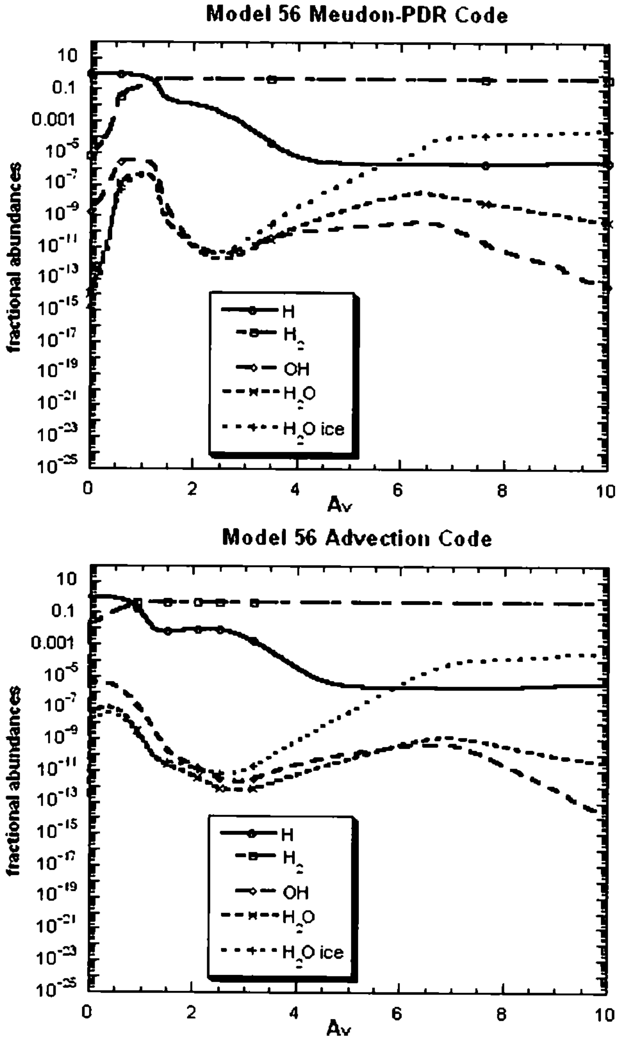

Figure 6.17: The comparison of abundance profiles of H species, gas phase and solid phase water for Model 56. Top panel shows Meudon-PDR code output. Bottom panel shows Advection code output. Advection code has been run with an initial velocity of 10^{-7}km s^{-1}. $n_{\rm H} = 10^6\,{\rm cm}^{-3}$.

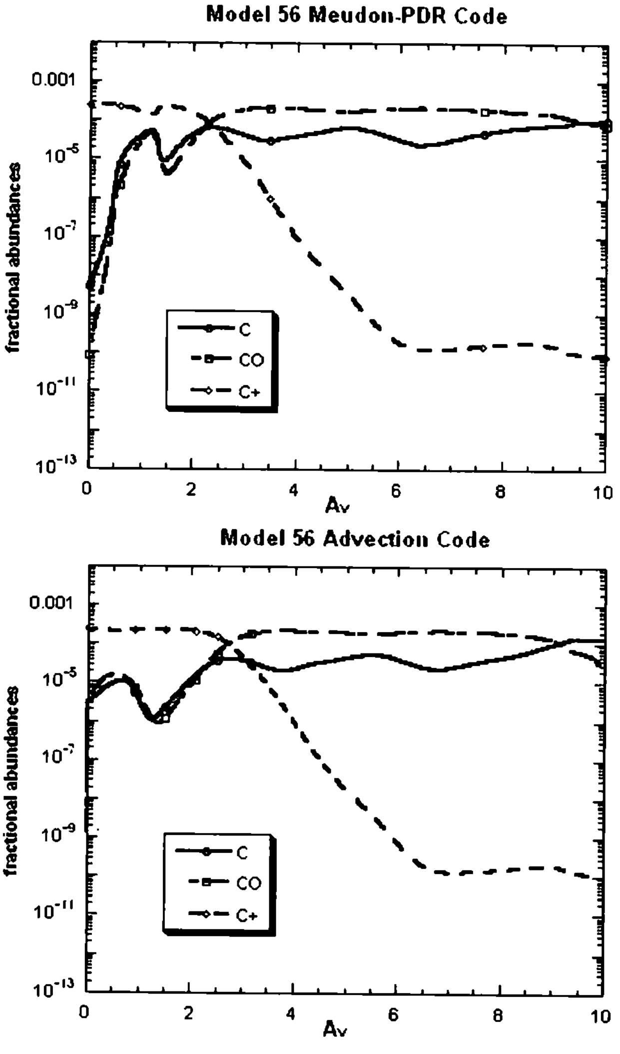

Figure 6.18: The comparison of abundance profiles of C, CO and C+ for Model 56. Top panel shows Meudon-PDR code output. Bottom panel shows Advection code output. Advection code has been run with an initial velocity of 10^{-7}km s^{-1}. $n_{\rm H} = 10^6$ cm^{-3}.

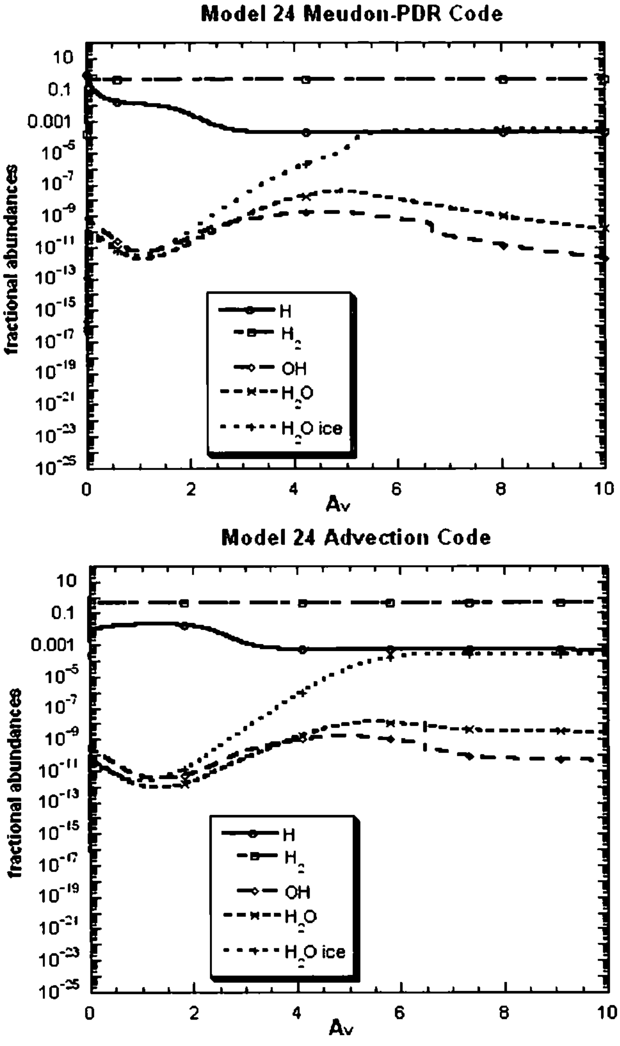

Figure 6.19: The comparison of abundance profiles of H species, gas phase and solid phase water for Model 24. Top panel shows Meudon-PDR code output. Bottom panel shows Advection code output. Advection code has been run with an initial velocity of 10^{-7}km s^{-1}. $n_{\mathrm{H}} = 10^4$ cm^{-3}.

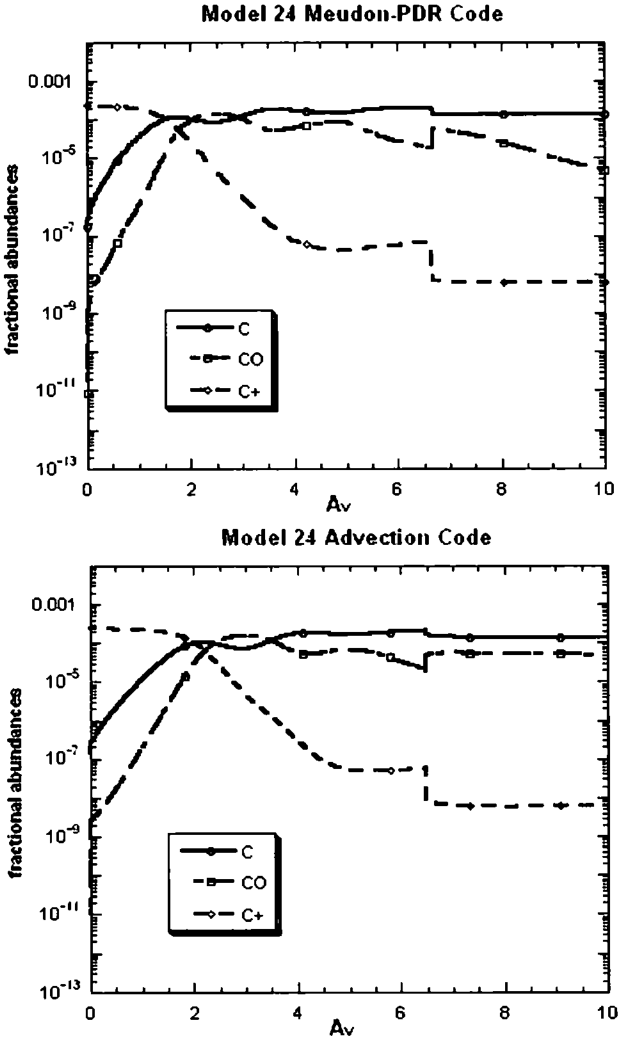

Figure 6.20: The comparison of abundance profiles of C, CO and C+ for Model 24. Top panel shows Meudon-PDR code output. Bottom panel shows Advection code output. Advection code has been run with an initial velocity of 10^{-7}km s^{-1}. $n_{\mathrm{H}} = 10^4$ cm^{-3}.

6.2 Nonstationary results

In order to investigate the effects of advection and self-consistent dynamics in the PDR structure and the line intensities of H_2O, Advection code was run with an initial velocity of 1 km s^{-1} which is a typical value for velocity of advected material in PDRs (Störzer and Hollenbach, 1998; Ferland et al., 1998; Walmsley et al., 1999; Bertoldi and Draine, 1996). The results presented in this section show that advection effects the abundance profiles. Since the emphasis of this thesis is on H_2O, the comparison between the abundance profiles obtained by running Advection code in stationary and nonstationary modes will be given only for atomic and molecular H, OH and H_2O. For comparison reasons, the photodesorption yield has been kept as it is in the chemistry file *chimie06g.chi* of Meudon-PDR code which is 4 orders of magnitude smaller than the value given by Westley et al. (1995). This causes high solid phase H_2O abundance in nonstationary mode. Since the photodesorption yield is low, in nonstationary mode, H_2O ice is pushed towards the cloud surface before photodesorption reaction occurs. This effect is stronger for lower radiation models, e.g., for Model 14, as seen in Figure 6.21. In the higher radiation models, the H_2O ice manages to survive longer in nonstationary mode compared to stationary mode. However, unlike in Model 14 (see Figure 6.21), for Model 56, it is destroyed closer to the cloud surface as seen in Figure 6.29. The higher photodesorption yield causes more effective destruction of H_2O ice releasing larger amount of gas phase H_2O. This is discussed in 7.2.1 and comparisons of abundance profiles for low and high photodesorption yields for all models are provided. The effects of advection in the PDR structure will be discussed in more detail in Chapter 7.

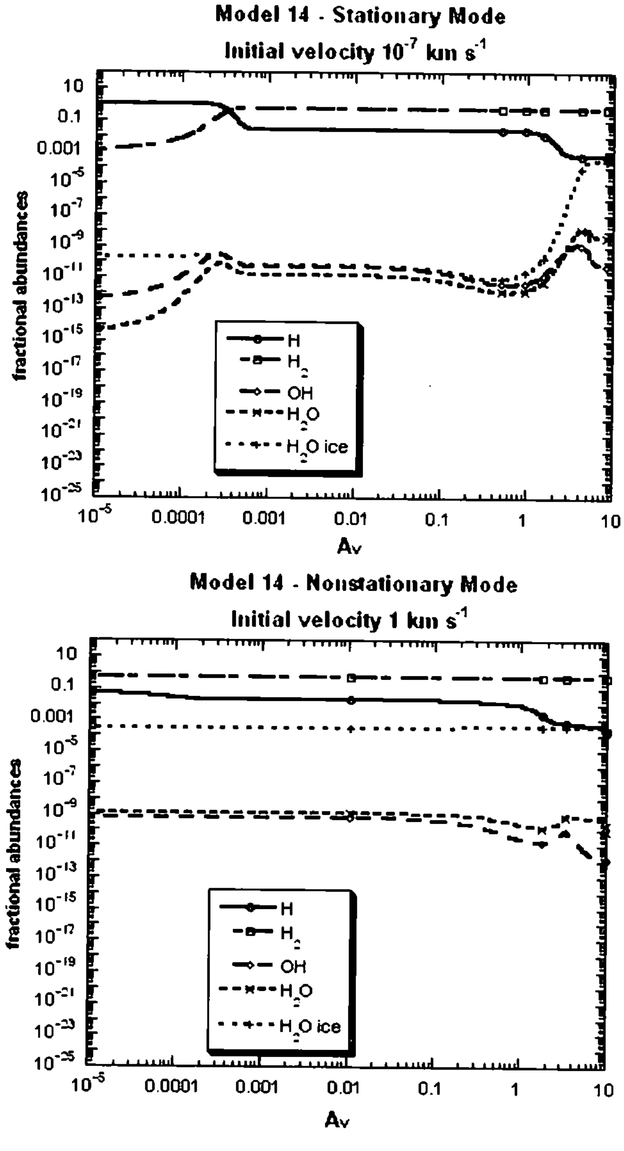

Figure 6.21: The comparison of abundance profiles of H species, gas phase and solid phase H_2O obtained by running Advection code in stationary and nonstationary modes for Model 14. Top panel shows the abundance profiles for stationary mode when the initial velocity is 10^{-7} km s^{-1}. Bottom panel shows the abundance profiles for nonstationary mode when the initial velocity is 1 km s^{-1}.

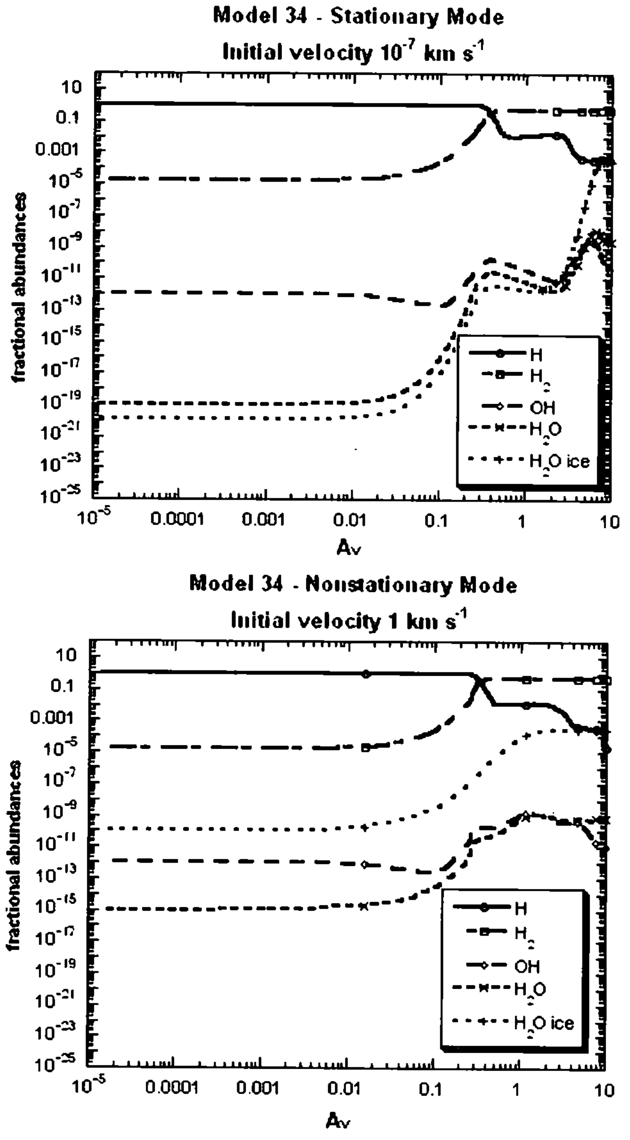

Figure 6.22: The comparison of abundance profiles of H species, gas phase and solid phase H_2O obtained by running Advection code in stationary and nonstationary modes for Model 34. Top panel shows the abundance profiles for stationary mode when the initial velocity is 10^{-7} km s^{-1}. Bottom panel shows the abundance profiles for nonstationary mode when the initial velocity is 1 km s^{-1}.

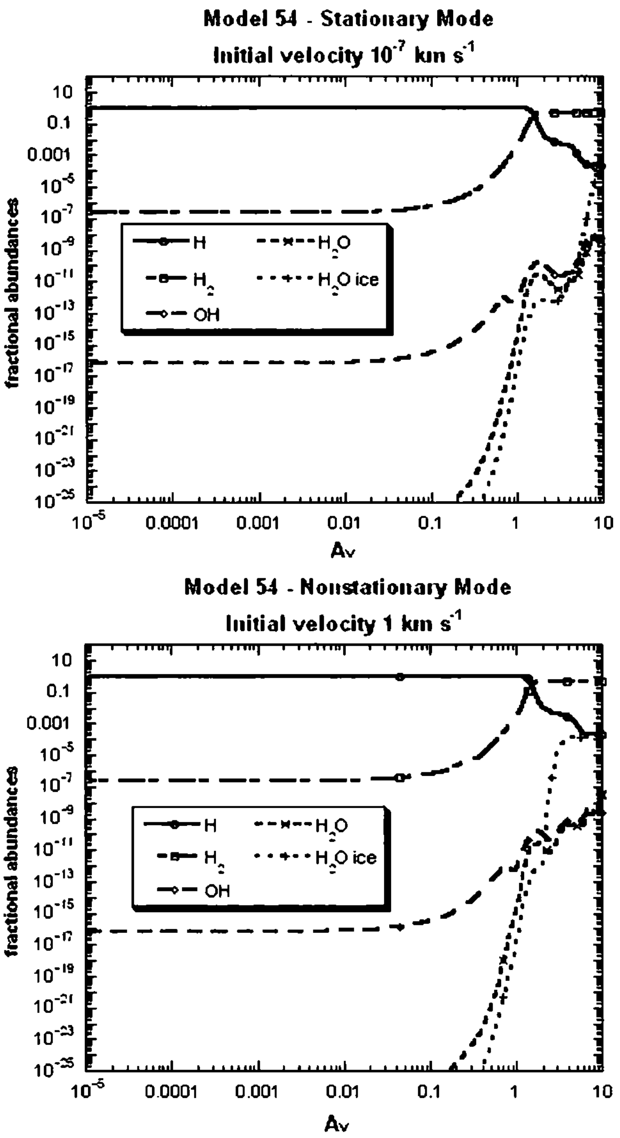

Figure 6.23: The comparison of abundance profiles of H species, gas phase and solid phase H_2O obtained by running Advection code in stationary and nonstationary modes for Model 54. Top panel shows the abundance profiles for stationary mode when the initial velocity is 10^{-7} km s^{-1}. Bottom panel shows the abundance profiles for nonstationary mode when the initial velocity is 1 km s^{-1}.

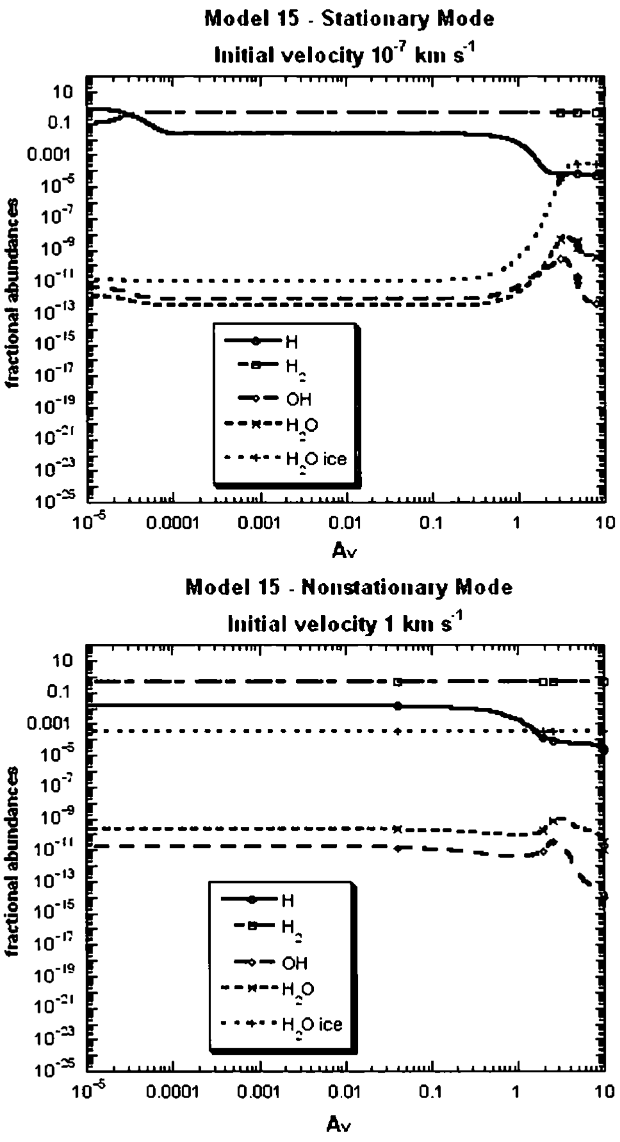

Figure 6.24: The comparison of abundance profiles of H species, gas phase and solid phase H_2O obtained by running Advection code in stationary and nonstationary modes for Model 15. Top panel shows the abundance profiles for stationary mode when the initial velocity is 10^{-7} km s^{-1}. Bottom panel shows the abundance profiles for nonstationary mode when the initial velocity is 1 km s^{-1}.

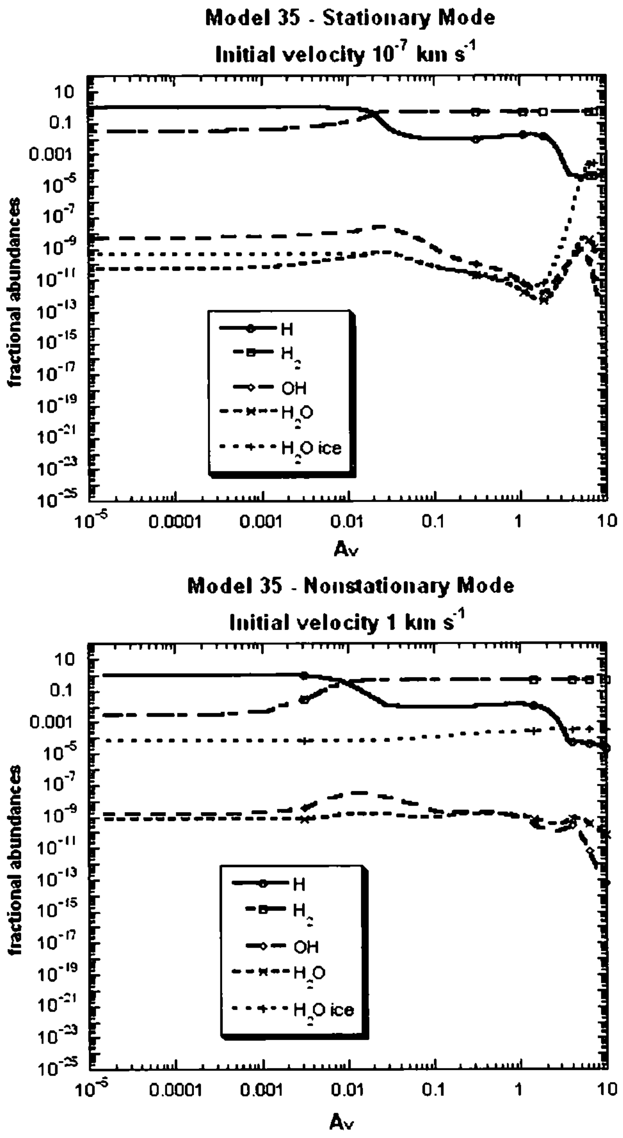

Figure 6.25: The comparison of abundance profiles of H species, gas phase and solid phase H_2O obtained by running Advection code in stationary and nonstationary modes for Model 35. Top panel shows the abundance profiles for stationary mode when the initial velocity is 10^{-7} km s^{-1}. Bottom panel shows the abundance profiles for nonstationary mode when the initial velocity is 1 km s^{-1}.

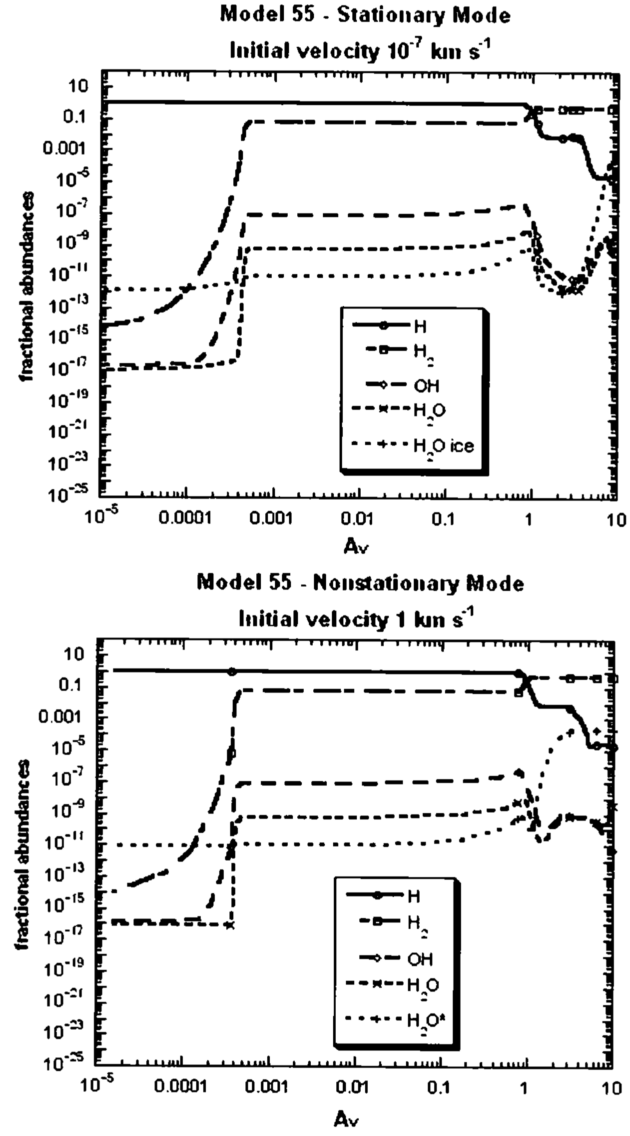

Figure 6.26: The comparison of abundance profiles of H species, gas phase and solid phase H_2O obtained by running Advection code in stationary and nonstationary modes for Model 55. Top panel shows the abundance profiles for stationary mode when the initial velocity is 10^{-7} km s^{-1}. Bottom panel shows the abundance profiles for nonstationary mode when the initial velocity is 1 km s^{-1}.

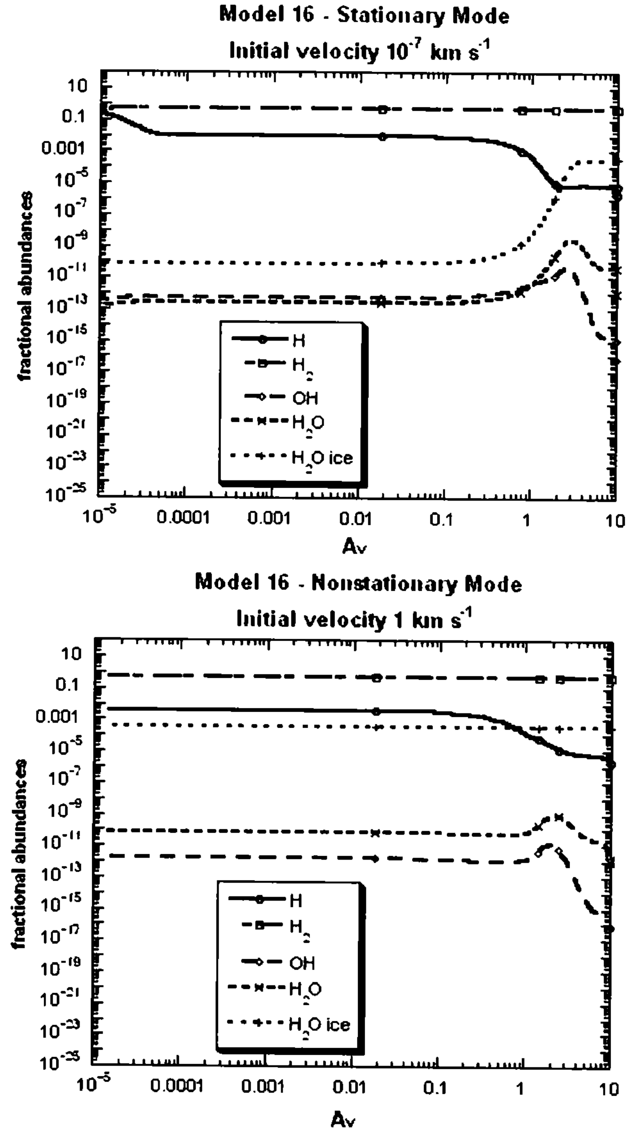

Figure 6.27: The comparison of abundance profiles of H species, gas phase and solid phase H_2O obtained by running Advection code in stationary and nonstationary modes for Model 16. Top panel shows the abundance profiles for stationary mode when the initial velocity is 10^{-7} km s^{-1}. Bottom panel shows the abundance profiles for nonstationary mode when the initial velocity is 1 km s^{-1}.

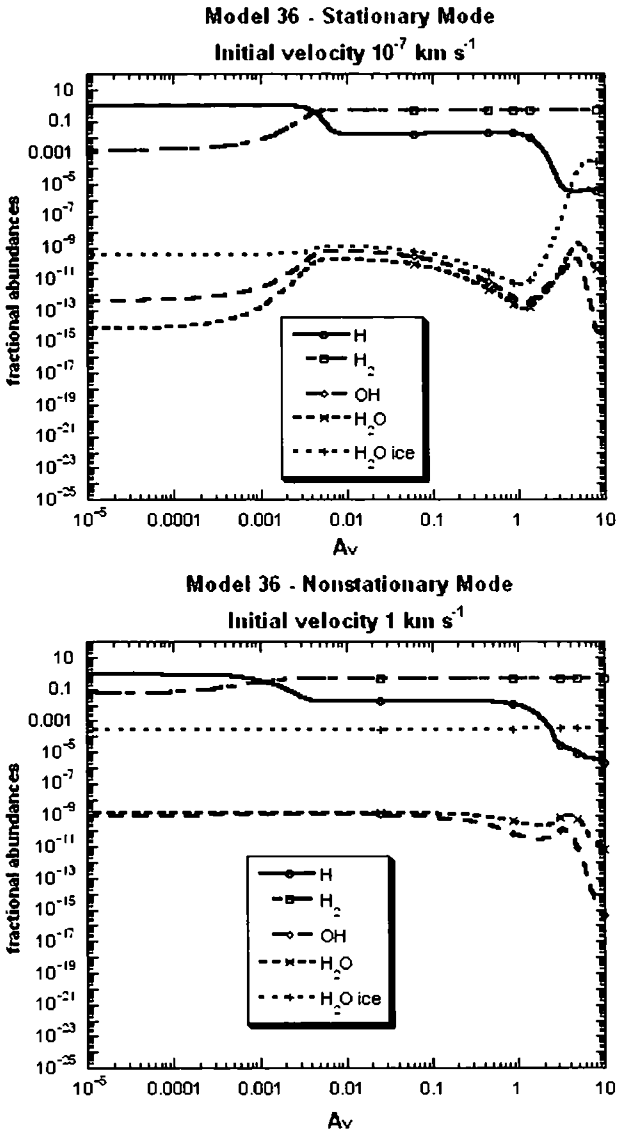

Figure 6.28: The comparison of abundance profiles of H species, gas phase and solid phase H_2O obtained by running Advection code in stationary and nonstationary modes for Model 36. Top panel shows the abundance profiles for stationary mode when the initial velocity is 10^{-7} km s^{-1}. Bottom panel shows the abundance profiles for nonstationary mode when the initial velocity is 1 km s^{-1}.

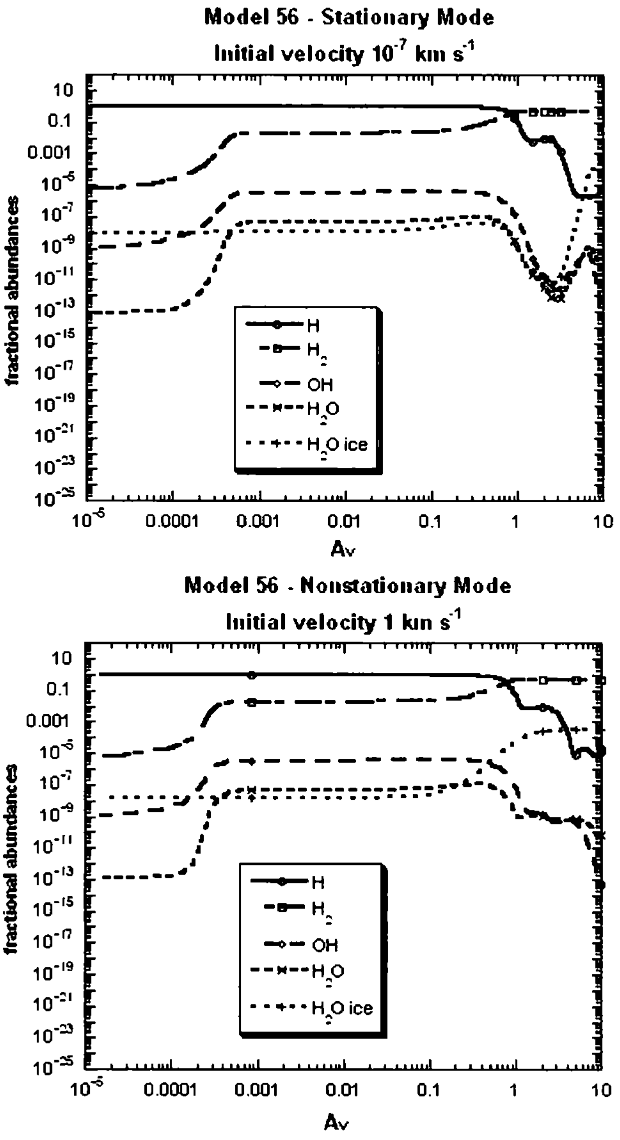

Figure 6.29: The comparison of abundance profiles of H species, gas phase and solid phase H_2O obtained by running Advection code in stationary and nonstationary modes for Model 56. Top panel shows the abundance profiles for stationary mode when the initial velocity is 10^{-7} km s^{-1}. Bottom panel shows the abundance profiles for nonstationary mode when the initial velocity is 1 km s^{-1}.

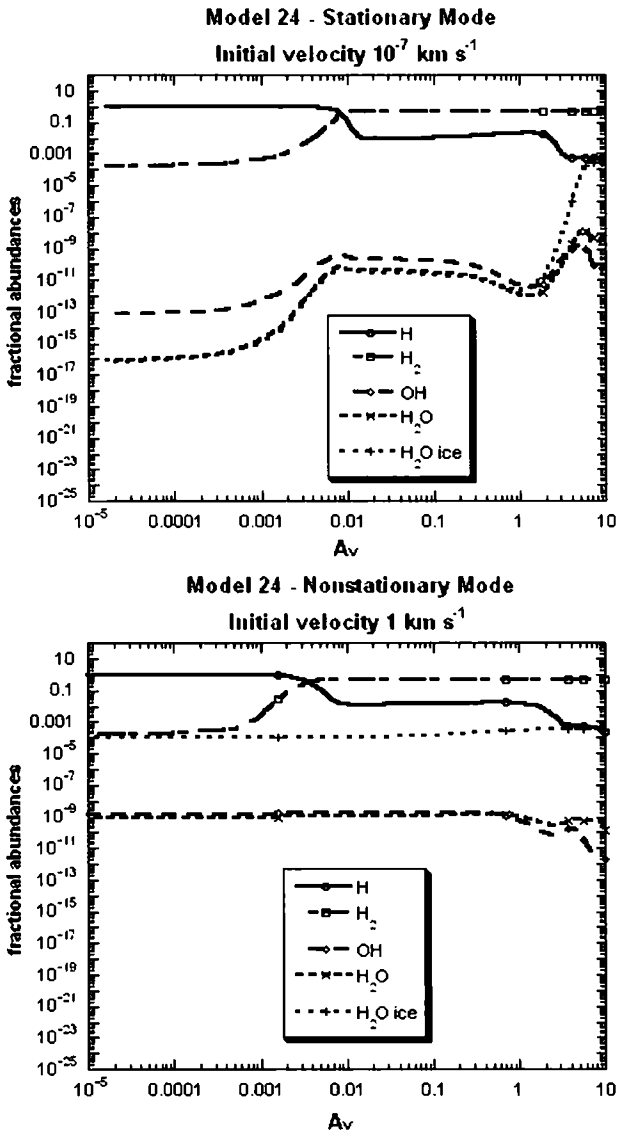

Figure 6.30: The comparison of abundance profiles of H species, gas phase and solid phase H_2O obtained by running Advection code in stationary and nonstationary modes for Model 24. Top panel shows the abundance profiles for stationary mode when the initial velocity is 10^{-7} km s^{-1}. Bottom panel shows the abundance profiles for nonstationary mode when the initial velocity is 1 km s^{-1}.

6.2.1 Velocity Profiles

As described in 5.2.2, the flow velocity is calculated self-consistently by using the conservation equations. The number density of the gas, n, increases as the molecules dissociate. By the conservation of number density, flow velocity decreases as the number density increases. The mass density of the gas also increases as the flow velocity decreases by the continuity equation. The velocity profiles for models with $n_{\mathrm{H}} = 10^4$ cm^{-3} are shown in Figure 6.31[1]. As seen in the Figure 6.31, the velocity gradient at lower A_v where the radiation is less attenuated, is large enough to use LVG approximation. The increase in the number density of the gas at lower depths is shown in 6.32.

---

[1] The velocity profiles show similar behaviour for the other models with higher densities, however, they are not included here due to the space limitations.

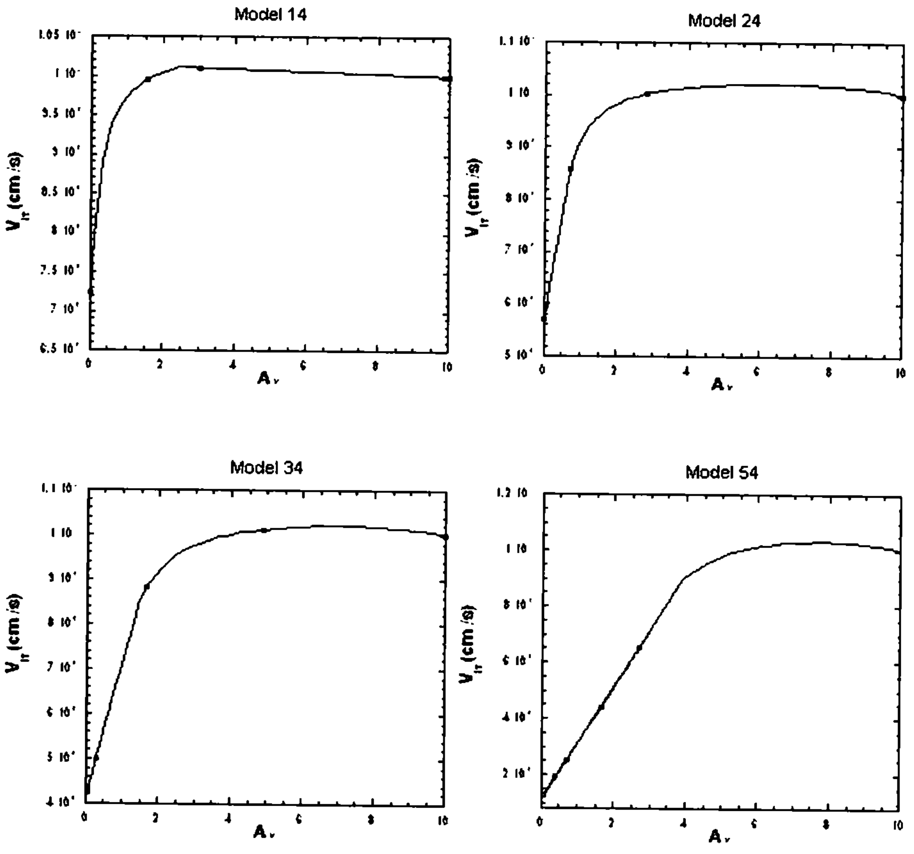

Figure 6.31: Velocity profiles for models with $n_{\mathrm{H}} = 10^4\ \mathrm{cm}^{-3}$. The flow velocity in $\mathrm{cm\,s}^{-1}$ is plotted as a function of A_v for models 14, 24, 34 and 54. The initial velocity at $A_v = 10$ is $1\mathrm{km\,s}^{-1}$.

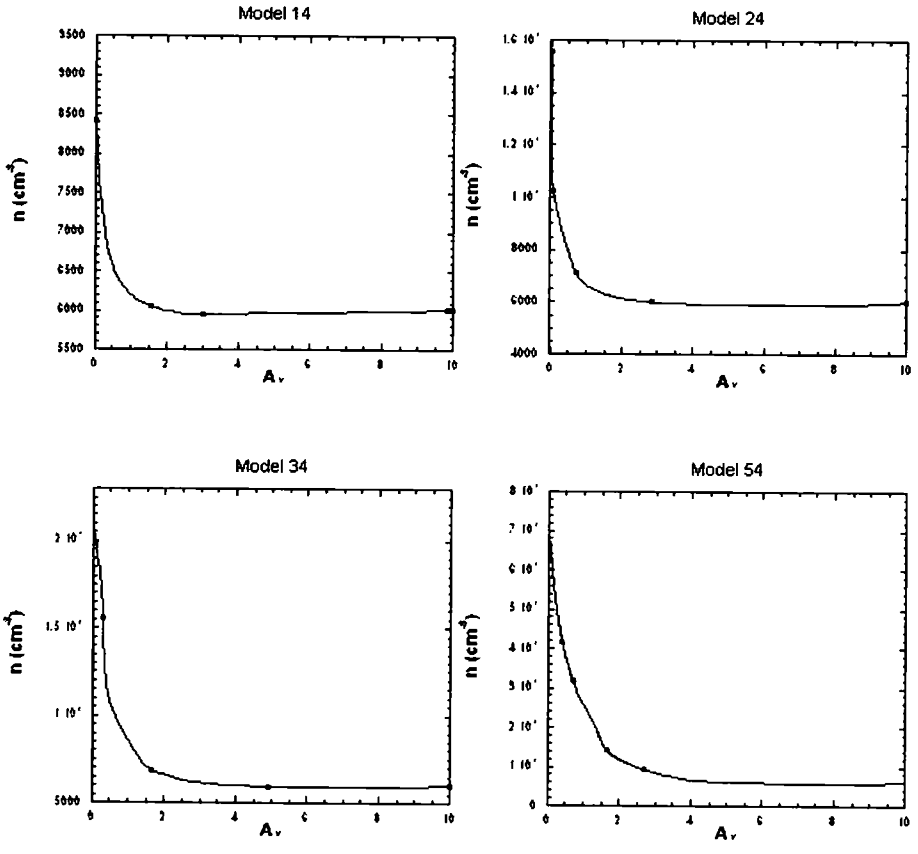

Figure 6.32: The number density of the gas as a function of A_v for models with $n_H = 10^4\,\mathrm{cm}^{-3}$.

6.3 Line intensities of H_2O

In order to calculate the rotational line intensities of H_2O arising from transitions between lower lying levels, Advection code was coupled to an escape probability code (see Chapter 4 for details). The results are presented in this section in Table 6.1 and the discussion regarding the effects of advection in line intensities of H_2O will be given in Chapter 7.

The escape probability code used in this work is capable of calculating the intensities of the transitions between the first 50 rotational levels of both o-H_2O and p-H_2O. As seen in the Table 6.1, for lower density, lower radiation models, there are less number of lines arising. The higher radiation, higher density models yield the intensities of transitions for all 50 rotational levels some of which are not in the wavelength range of Herschel Space Observatory Instruments HIFI and PACS. Therefore, the intensities presented here are kept limited to the transitions which will be observed.

Models	Transitions (μm)							
	o-H_2O Intensity (erg s^{-1} cm^{-2} sr^{-1})							
Models	538.27μm	179.53μm	108.07μm	174.63μm	259.99μm	113.54μm	99.49μm	82.03μm
14	5.08(-13)	2.73(-13)	-2.00(-13)	8.24(-15)	8.61(-17)			
15	4.81(-09)	4.17(-09)	5.66(-12)	2.77(-11)	5.75(-14)			
16	5.26(-08)	1.92(-07)	3.30(-08)	2.04(-08)	6.86(-10)	3.54(-10)	1.70(-12)	
34	1.07(-08)	3.93(-08)	-1.06(-09)	2.29(-09)	4.60(-10)	1.64(-13)		
35	3.04(-08)	1.60(-07)	3.94(-08)	5.88(-08)	1.60(-08)	2.17(-09)	1.45(-12)	2.25(-13)
36	7.55(-08)	5.50(-07)	3.13(-07)	2.75(-07)	7.72(-08)	5.00(-08)	5.38(-10)	2.54(-13)
54	2.23(-08)	1.69(-07)	-1.36(-08)	1.38(-08)	1.75(-09)	9.51(-10)		
55	1.35(-07)	2.15(-06)	1.82(-06)	1.17(-06)	4.42(-07)	1.46(-07)	1.05(-08)	3.03(-10)
56	6.13(-07)	1.22(-05)	2.05(-05)	9.94(-06)	4.95(-06)	1.37(-05)	3.34(-06)	4.84(-07)
24	6.66(-10)	8.38(-11)	4.50(-13)	9.66(-13)	1.91(-14)	1.71(-13)		
	p-H_2O Intensity (erg s^{-1} cm^{-2} sr^{-1})							
Models	269.27μm	303.45μm	398.64μm	100.98μm	138.53μm	125.35μm	95.63μm	83.28μm
14	1.12(-13)	1.06(-14)	7.50(-16)	-1.40(-15)				
15	7.08(-09)	4.72(-10)	1.96(-11)	4.42(-13)	1.23(-16)			
16	1.13(-07)	3.03(-08)	1.65(-08)	1.00(-09)	4.17(-09)			
34	1.99(-08)	6.41(-09)	2.10(-09)	4.86(-10)	5.80(-10)	1.37(-11)		
35	8.85(-08)	5.18(-08)	1.76(-08)	-1.24(-09)	5.47(-09)	9.83(-14)	1.64(-14)	
36	2.69(-07)	1.90(-07)	7.57(-08)	6.15(-08)	1.39(-07)	1.71(-09)	2.48(-16)	
54	7.23(-08)	4.59(-08)	-5.49(-09)	1.78(-10)	2.03(-09)			
55	5.93(-07)	2.35(-07)	-8.82(-08)	5.12(-10)	2.00(-09)	3.84(-10)	6.52(-11)	1.61(-11)
56	3.15(-06)	2.59(-06)	1.09(-06)	9.23(-06)	8.49(-06)	3.07(-06)	1.69(-07)	6.42(-08)
24	1.55(-10)	3.30(-12)	1.05(-13)	-4.95(-14)	3.70(-14)	$1.30E-15$		

Table 6.1: The intensities in erg s^{-1} cm^{-2} sr^{-1} calculated for each model studied for 1 km s^{-1} initial velocity. Transitions presented were selected according to the list of transitions that will be observed by Herschel Space Observatory. a(-b) denotes a × 10^{-b}.

Chapter 7

Discussion

In previous sections, the models and the method were described and the results were presented. In this section, the findings of this work will be discussed in more detail. The results presented here show that the advection in PDRs may effect the PDR structure, i.e., the classical PDRs in which there is an atomic to molecular H transition zone may not exist depending on the density and the radiation of the PDR. This finding is in agreement with the findings of Störzer and Hollenbach (1998). Advection not only effects the structure of the PDR, but it also effects the abundance profiles of chemical species and average abundance values. The line intensities of H_2O are also effected by advection and the treatment of the flow velocity.

As the gas flows with a velocity of the order of 1 $\mathrm{km\,s^{-1}}$, the dynamical timescale becomes comparable to the chemical timescales. The dynamical timescale is the characteristic time required for significant change in A_v and it is calculated as

$$t_{dyn} = \frac{1}{A_v \frac{dA_v}{dt}}$$

If the chemical timescale for a reaction is longer than the dynamical timescale, the reaction does not occur by the time that the chemical species of interest reaches the cloud surface. This interplay between the timescales, in other words, dynamics and the chemistry, may cause significant effects in the structure and the line intensities as will be shown in the following sections.

7.1 PDR structure

The atomic to molecular H transition zone determines the PDR structure since H_2 is the most abundant molecule and it initiates the molecular chemistry in the PDRs. Therefore, in the following analysis, the location of the H/H_2 will be emphasized.

Störzer and Hollenbach (1998), in their numerical parameter study of plane-parallel, semi-infinite PDRs where the IF is moving with a fixed velocity v_{IF} found that there is no H/H_2 photodissociation front for models with $\chi/n \leq 0.2v_{IF}$ where n is in cm^{-3} and v_{IF} is in $\mathrm{km\,s}^{-1}$. The findings of this work are consistent with the findings of Störzer and Hollenbach (1998) for models 14, 15, 16, 54 and 56, although the velocity is calculated self-consistently in our work and may vary upto 10% of its initial value. For Model 14,

$$\chi/n \approx 10^{-3} \quad \text{and} \quad 0.13 \lesssim 0.2v_{IF} \lesssim 0.2$$

where v_{IF} ranges between 0.66 and 1 km s^{-1}. The effect of advection in PDR structure for Model 14 is clearly seen in Figure 6.21 where the H/H$_2$ zone disappears in nonstationary mode. The similar argument holds for models 15 and 16 and can be seen in corresponding figures 6.24 and 6.27. For models 24, 34, 35 and 36, the zone does not completely disappear, however the location of it is slightly closer to the surface in nonstationary mode. For models 54, 55 and 56 where the PDR material is exposed to the highest radiation compared to the rest of the models, the location of the transition zone is the least effected by advection as seen in Figures 6.23, 6.26 and 6.29. Table 7.1 summarizes the values of χ/n and $0.2v_{IF}$ considered in this comparison.

Model	χ/n	$0.2v_{IF}$	
		Lowest	Highest
Model 14	10^{-3}	0.13	0.2
Model 34	10^{-1}	0.08	0.2
Model 54	10	0.02	0.2
Model 15	10^{-4}	0.12	0.2
Model 35	10^{-2}	0.08	0.2
Model 55	1	0.06	0.2
Model 16	10^{-5}	0.16	0.2
Model 36	10^{-3}	0.06	0.2
Model 56	10^{-1}	0.11	0.2
Model 24	10^{-2}	0.11	0.2

Table 7.1: The values for comparison of our findings to the findings of Störzer and Hollenbach (1998). The velocity v_{IF} is in km s^{-1}. The highest values for v_{IF} correspond to the chosen initial velocity of 1 km s^{-1} at $A_v = 10$ for all the models. The lowest values of v_{IF} are reached at the cloud surface, i.e., at $A_v \sim 10^{-5}$.

7.2 H_2O

In this section the effects of advection in H_2O abundance profile, average abundance values and the rotational line intensities will be discussed. For comparison purposes, the calculation of photodesorption of H_2O ice was adopted to that of Meudon in which the photodesorption yield parameter is 5×10^{-7} (see Walmsley et al. (1999)). The yield given by Westley et al. (1995) for photodesorption of H_2O ice was adopted in the models used for calculation of line intensities. First, the comparison of the abundance profiles obtained using these two photodesorption yield parameters will be presented. In the rest of the discussion, yield obtained by Westley et al. (1995) will be used. The most recent laboratory measurements of the photodesorption of H_2O ice have not been published yet, however, the preliminary results provided by K. Öberg (priv. comm.) will be discussed in Section 7.2.1.

7.2.1 Abundance

Photodesorption of H_2O ice

Photodesorption is considered to be the main destruction mechanism of H_2O ice, that contributes to the abundance of gas phase H_2O. Therefore, it will be illustrative to compare the effects of using different photodesorption yields. The Figures 7.1 to 7.10 are presented for this purpose. It is clear for all models that using the yield given by Westley et al. (1995) the H_2O abundance increases as expected. The abundance of solid phase H_2O drops more efficiently. In the low radiation models, e.g., Model 14, using the photodesorption yield by Westley et al. (1995) causes a drop in H_2O ice abundance at $A_v \sim 3$ as seen in Figure 7.1 whereas for Model 54 H_2O ice abundance drops at much larger A_v as seen in Figure 7.3. Since the radiation is high for Model 54, the gas phase H_2O is destroyed at $A_v \sim 1.5$ for both photodesorption yields used. In higher density models, e.g., in Model 16, gas phase H_2O abundance appears to be effected more by using higher photodesorption yield (see 7.7. There is no feedback from the variations in the water abundance on the thermal profile, as temperature is produced by applying external fit to the temperature profile produced by Meudon-PDR code.

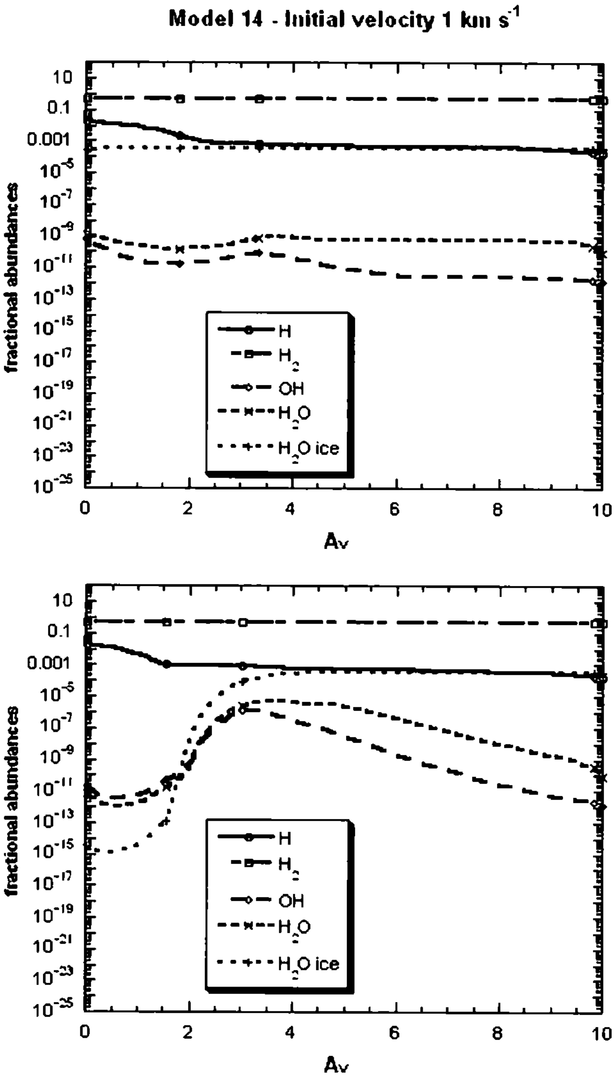

Figure 7.1: The comparison of abundance profiles of H species, gas phase and solid phase H_2O obtained by running Advection code for Model 14 with two different photodesorption yields. Top panel shows the abundance profiles for the photodesorption yield adopted from Meudon-PDR code (see text for details). Bottom panel shows the abundance profiles for $Y = 3.5 \times 10^{-3} + 0.13e^{-336/T_{gr}}$.

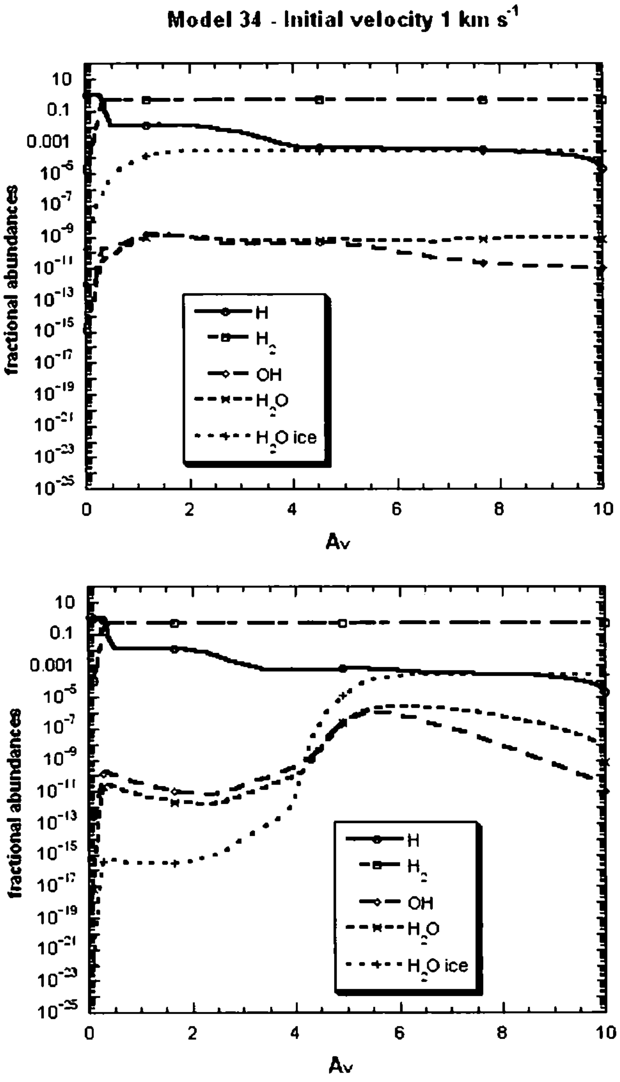

Figure 7.2: The comparison of abundance profiles of H species, gas phase and solid phase H_2O obtained by running Advection code for Model 34 with two different photodesorption yields. Top panel shows the abundance profiles for the photodesorption yield adopted from Meudon-PDR code (see text for details). Bottom panel shows the abundance profiles for $Y = 3.5 \times 10^{-3} + 0.13e^{-336/T_{gr}}$.

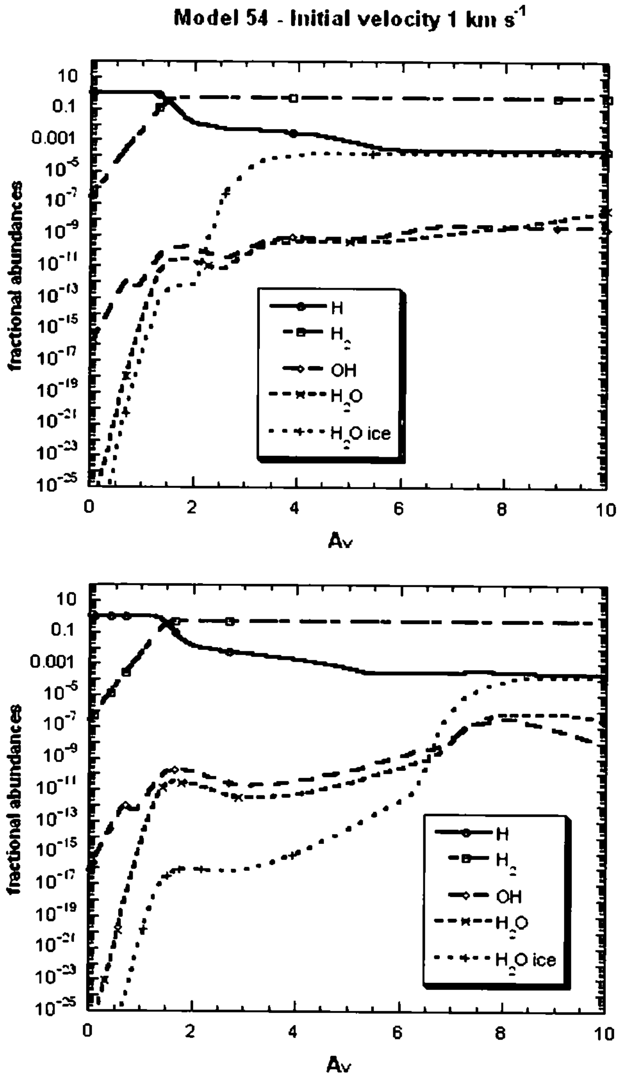

Figure 7.3: The comparison of abundance profiles of H species, gas phase and solid phase H_2O obtained by running Advection code for Model 54 with two different photodesorption yields. Top panel shows the abundance profiles for the photodesorption yield adopted from Meudon-PDR code (see text for details). Bottom panel shows the abundance profiles for $Y = 3.5 \times 10^{-3} + 0.13e^{-336/T_{gr}}$.

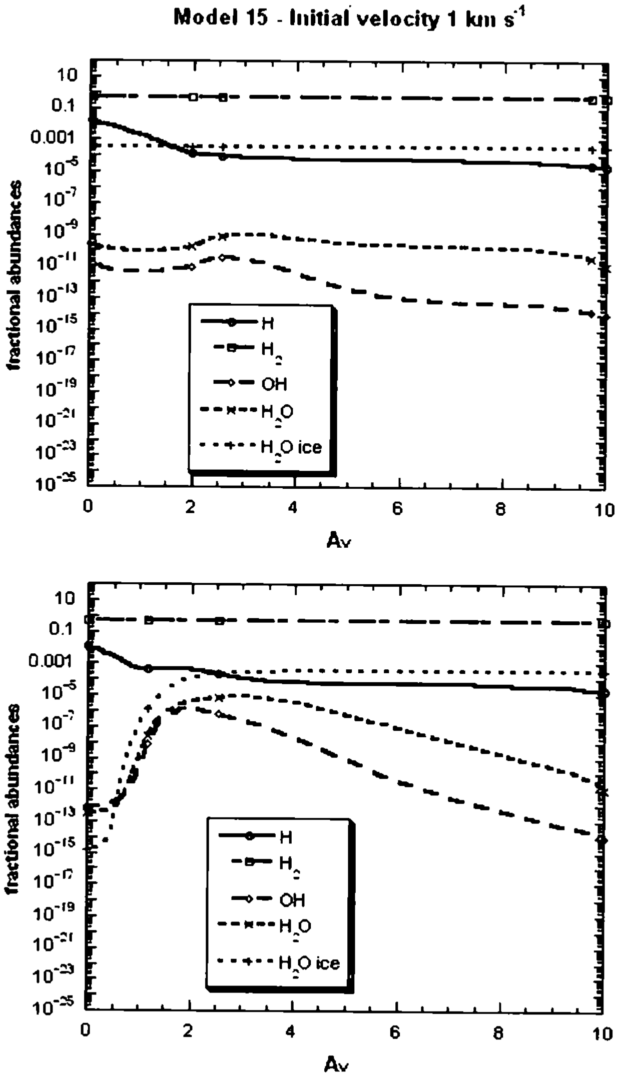

Figure 7.4: The comparison of abundance profiles of H species, gas phase and solid phase H_2O obtained by running Advection code for Model 15 with two different photodesorption yields. Top panel shows the abundance profiles for the photodesorption yield adopted from Meudon-PDR code (see text for details). Bottom panel shows the abundance profiles for $Y = 3.5 \times 10^{-3} + 0.13e^{-336/T_{gr}}$.

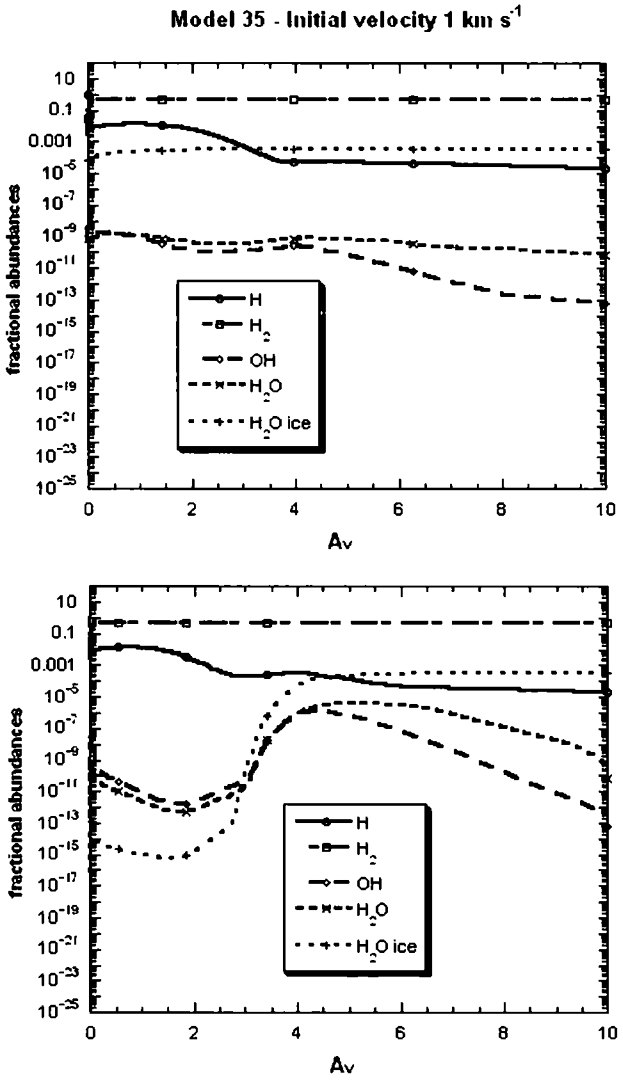

Figure 7.5: The comparison of abundance profiles of H species, gas phase and solid phase H_2O obtained by running Advection code for Model 35 with two different photodesorption yields. Top panel shows the abundance profiles for the photodesorption yield adopted from Meudon-PDR code (see text for details). Bottom panel shows the abundance profiles for $Y = 3.5 \times 10^{-3} + 0.13e^{-336/T_{gr}}$.

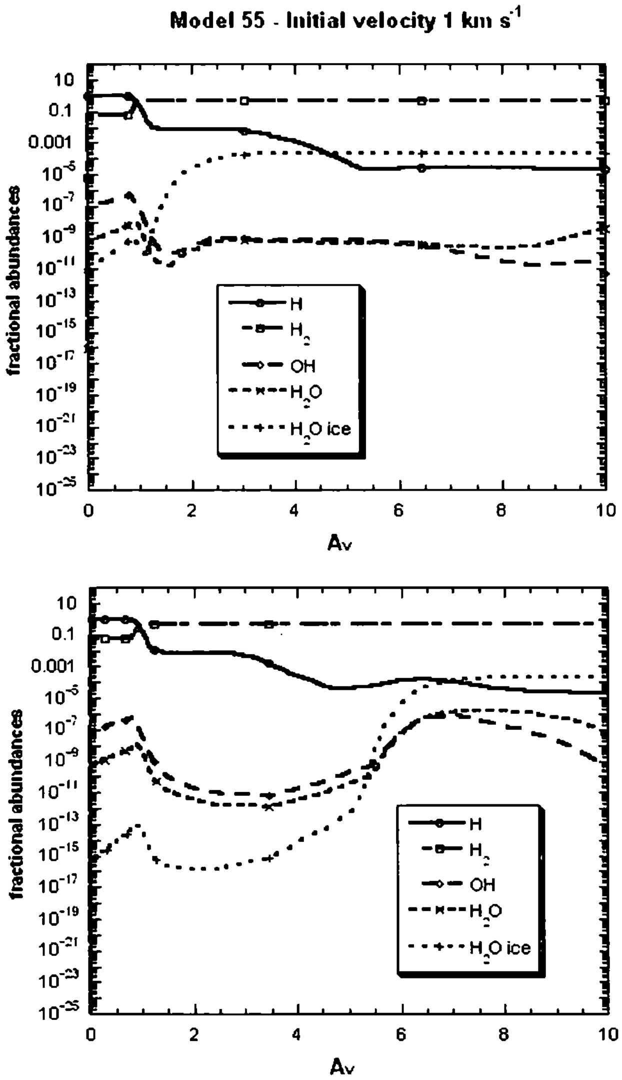

Figure 7.6: The comparison of abundance profiles of H species, gas phase and solid phase H_2O obtained by running Advection code for Model 55 with two different photodesorption yields. Top panel shows the abundance profiles for the photodesorption yield adopted from Meudon-PDR code (see text for details). Bottom panel shows the abundance profiles for $Y = 3.5 \times 10^{-3} + 0.13e^{-336/T_{gr}}$.

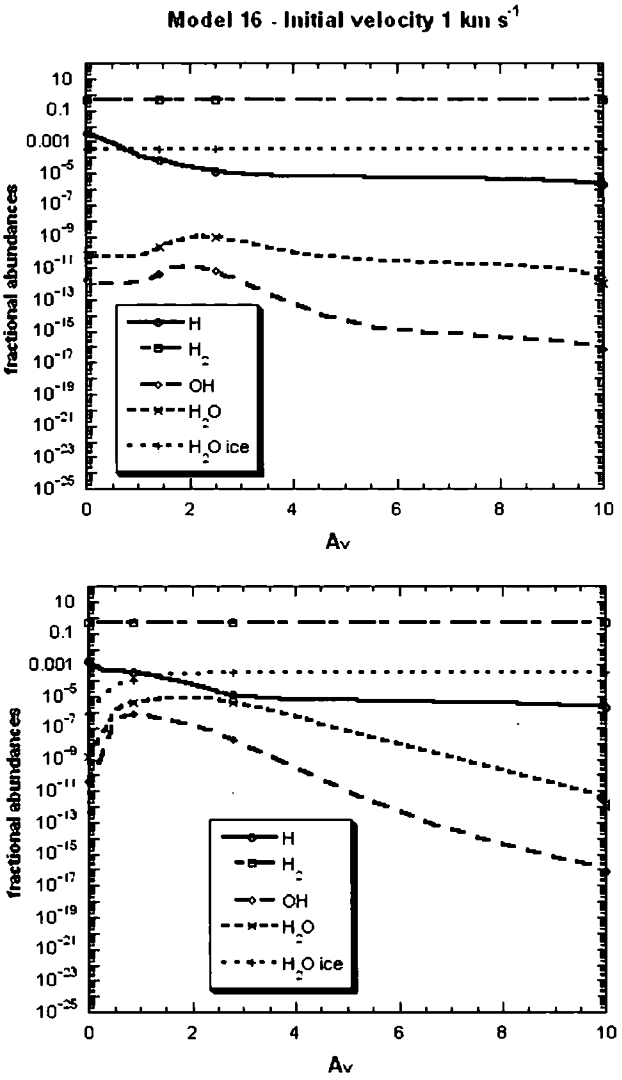

Figure 7.7: The comparison of abundance profiles of H species, gas phase and solid phase H_2O obtained by running Advection code for Model 16 with two different photodesorption yields. Top panel shows the abundance profiles for the photodesorption yield adopted from Meudon-PDR code (see text for details). Bottom panel shows the abundance profiles for $Y = 3.5 \times 10^{-3} + 0.13e^{-336/T_{gr}}$.

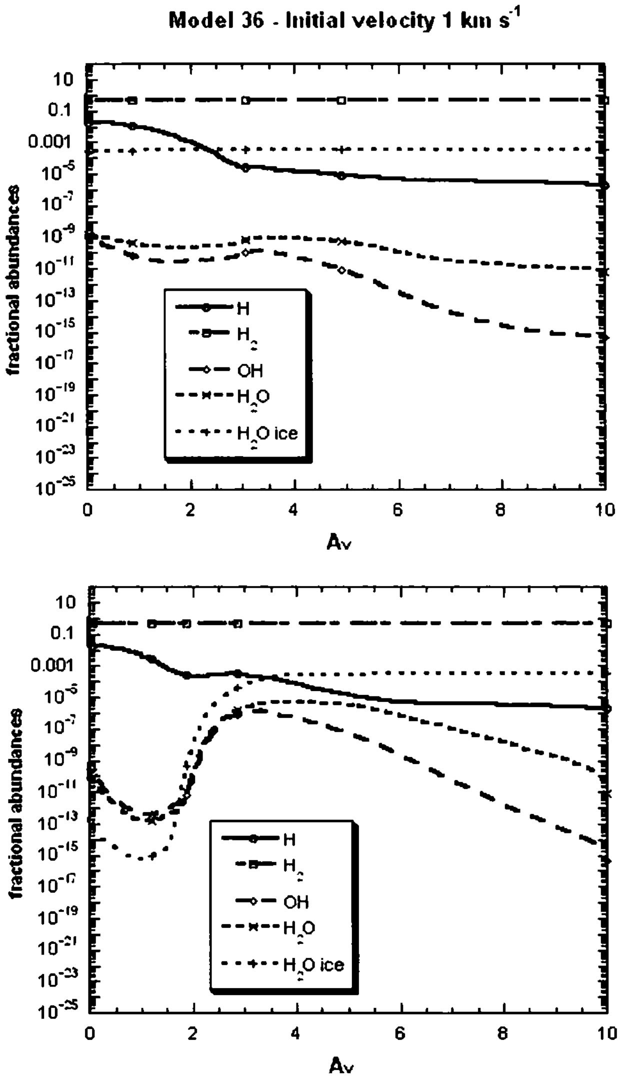

Figure 7.8: The comparison of abundance profiles of H species, gas phase and solid phase H_2O obtained by running Advection code for Model 36 with two different photodesorption yields. Top panel shows the abundance profiles for the photodesorption yield adopted from Meudon-PDR code (see text for details). Bottom panel shows the abundance profiles for $Y = 3.5 \times 10^{-3} + 0.13e^{-336/T_{gr}}$.

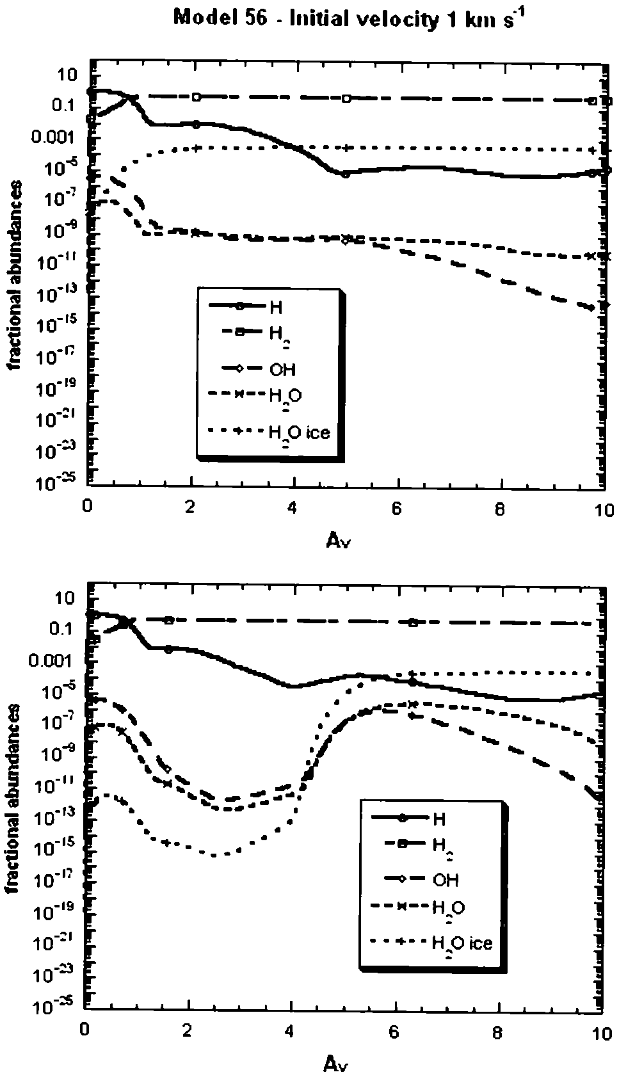

Figure 7.9: The comparison of abundance profiles of H species, gas phase and solid phase H_2O obtained by running Advection code for Model 56 with two different photodesorption yields. Top panel shows the abundance profiles for the photodesorption yield adopted from Meudon-PDR code (see text for details). Bottom panel shows the abundance profiles for $Y = 3.5 \times 10^{-3} + 0.13e^{-336/T_{gr}}$.

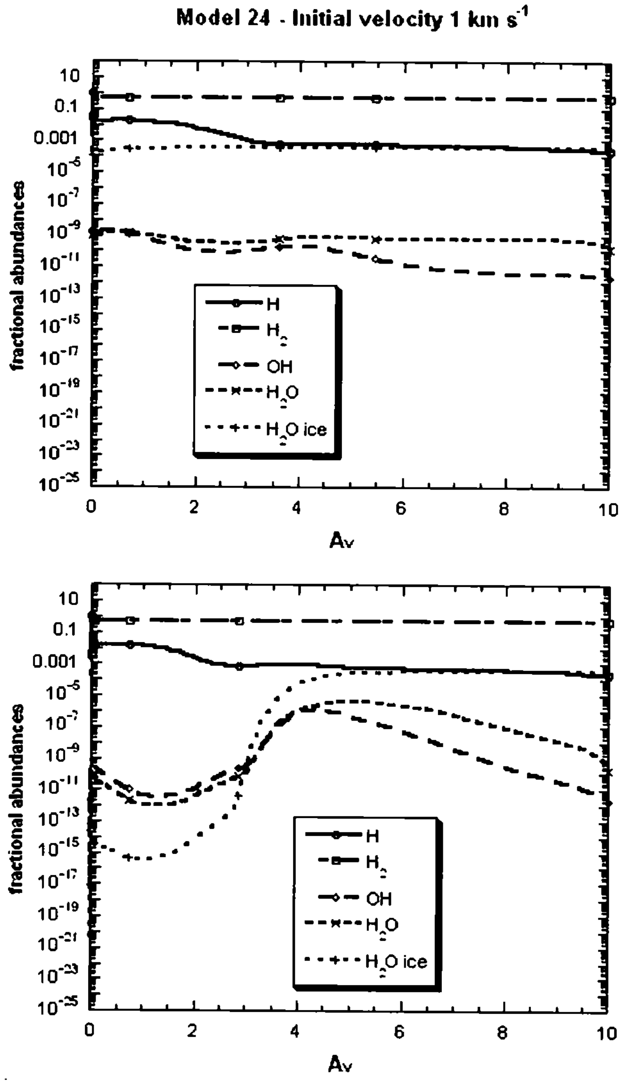

Figure 7.10: The comparison of abundance profiles of H species, gas phase and solid phase H_2O obtained by running Advection code for Model 24 with two different photodesorption yields. Top panel shows the abundance profiles for the photodesorption yield adopted from Meudon-PDR code (see text for details). Bottom panel shows the abundance profiles for $Y = 3.5 \times 10^{-3} + 0.13e^{-336/T_{gr}}$.

The most recent laboratory measurements of photodesorption of H_2O ice have been carried out by Öberg et al. and the photodesorption yield has been kindly provided by K. Öberg. The photodesorption yield in molecules per photon is given as

$$Y(T,X) = (1.3 \times 10^{-3} + 3.5 \times 10^{-5} T_{gr})(1 - \exp(\mathrm{X}/l(T_{gr}))) \tag{7.1}$$

where T_{gr} is the dust temperature, X is the ice thickness in monolayers and $l(T_{gr})$ is the diffusion parameter. For the purpose of comparison with the photodesorption yield given by Westley et al. (1995), the Equation 7.1 has been approximated as

$$Y(T) = 1.3 \times 10^{-3} + 3.5 \times 10^{-5} T_{gr}.$$

The comparison between the dust temperature dependence of photodesorption yield by Westley et al. (1995) and Öberg et al. has been plotted in Figure 7.11. The dust temperature in our models range between $\sim$ 6K and $\sim$ 110K. The Figure 7.11 suggests that the treatment of photodesorption yield may account for changes in the abundance of gas phase H_2O and therefore in the resulting line intensities. This needs further investigation by including the most recent laboratory measurements in our models once they are made available.

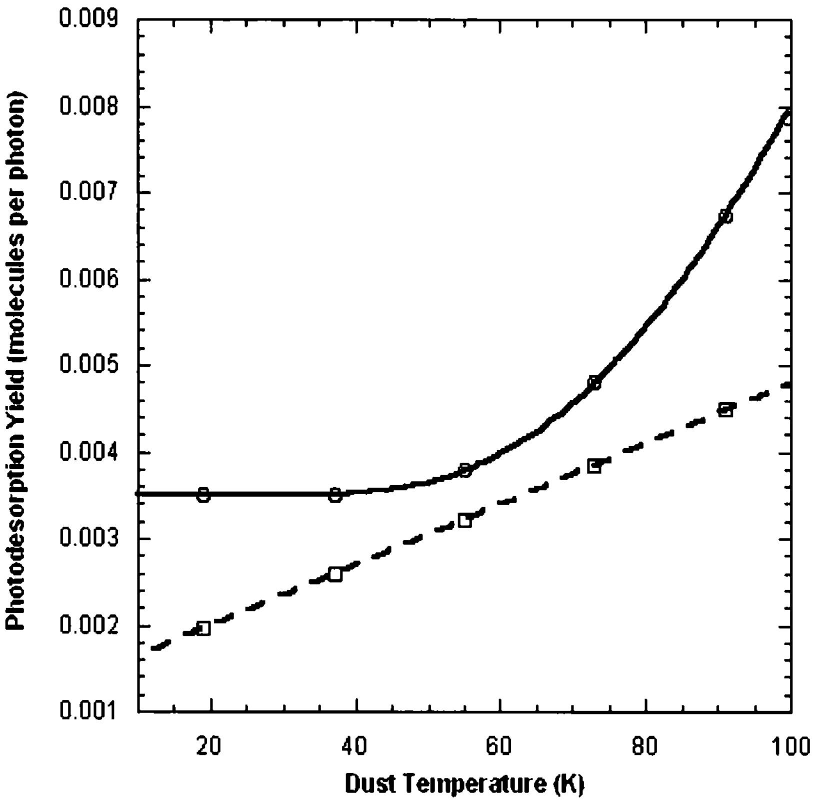

Figure 7.11: The photodesorption yield of H_2O ice in molecules per photon as a function of dust temperature. Solid curve shows the photodesorption yield measured by Westley et al. (1995) and dashed curve shows the preliminary result for photodesorption yield provided by Öberg et al.

Abundance Profiles

Now, the effects of advection in the abundance profile of H_2O will be discussed. The abundance profiles obtained using photodesorption yield of Westley et al. (1995) will be shown for models 14, 56 and 24. It is not possible to present the results for all the models studied due to the space limitations. The models 14, 56 and 24 were selected because of the following reasons; Model 14 represents the PDRs of which the ratio χ/n has the lowest value among studied models (see discussion in Section 7.1), therefore the abundance profiles and the structure are effected by advection to the greatest extent compared to other models presented. Model 56, in opposite, has the highest value for χ/n, therefore, it is the least effected model by advection among the studied models. Model 24 is selected because this model has been used for comparison with the results from the previous work of Bergin et al. (2003).

As shown in the Figure 7.12, the abundance profile of H_2O is effected by the advection even for Model 56. The material is pushed towards the cloud surface with a velocity of the order of $1\,\mathrm{km\,s^{-1}}$ and as a result H_2O manages to survive at lower A_v compared to the stationary case. For Model 14, H_2O survives until it reaches the cloud depth $A_v \sim 3.5$ then starts to decrease at lower depths due to the photodissociation. For Model 24, due to the higher radiation compared to Model 14, H_2O survives upto $A_v \sim 4.5$. The high radiation causes photodissocation of H_2O even at higher depths, $A_v \sim 6$, for Model 56. Photodesorption of H_2O ice at lower depths contributes to the abundance of gas phase H_2O. This effect is stronger for Model 56 due to the high radiation, whereas, the abundance of gas phase H_2O increases only from $A_v \sim 1$ for Model 14. Deeper in the cloud, photodesorption is mainly due to the secondary photons as discussed in Section 5.2.4.

The average relative abundance of H_2O is 2.25×10^{-8} for Model 14 in stationary mode, whereas it is 5.26×10^{-7} in nonstationary mode. For Model 24, stationary mode yields 3.40×10^{-9} and nonstationary mode yields 1.74×10^{-7} for average relative abundance of H_2O. For Model 56, the values are 2.12×10^{-8} and 9.98×10^{-8} for stationary and nonstationary modes, respectively.

7.2.2 Line intensities

So far the effects of advection in PDR structure and in the chemical abundances have been discussed for a range of radiation and density parameters. In order to investigate how advection and choice of initial velocities affect the resulting line intensities, Model 14 has been run for initial velocities ranging between 10^{-5} and $1\ \mathrm{km\,s^{-1}}$. Intensities of H_2O rotational lines have been calculated for each case. The results for mostly observed rotational line of water, i.e., 556.936 GHz, are plotted in Figure 7.13. As seen in the figure, the resulting intensity of the same line depends on the order of magnitude of the velocity. The sharp rise in the intensity between the initial velocities $10^{-3}\ \mathrm{km\,s^{-1}}$ and $10^{-2}\ \mathrm{km\,s^{-1}}$ result from the changes in the gas phase and solid phase abundance profiles of H_2O within that range. This is displayed in Figure 7.14. As seen in the figure, the behaviour of abundances of both gas phase and solid phase H_2O suggests that the initial velocity $10^{-2}\,\mathrm{km\,s^{-1}}$ acts as a critical flow velocity below which the chemical timescales regarding H_2O are still shorter than the dynamical timescale. Chemical timescales of photodissociation of H_2O and photodesorption of H_2O ice have been compared to the dynamical timescale for the initial velocities 10^{-3}, 10^{-2} and $10^{-1}\,\mathrm{km\,s^{-1}}$. Figures 7.17, 7.16 and 7.15 illustrate this comparison. As seen in these figures, initial velocities above $10^{-2}\,\mathrm{km\,s^{-1}}$ make the dynamical timescale shorter than timescale for photodesorption of H_2O ice. This reflects in the abundance profiles of gas phase and solid phase H_2O. However, it should be noted that the gas phase H_2O is formed mainly by dissociative recombination of the H_3O^+ ion, in the cold gas where the temperature is below 100 K. The drop in the line intensity above the initial velocity $10^{-2}\,\mathrm{km\,s^{-1}}$ may be due to the self-absorption but this needs to be verified numerically.

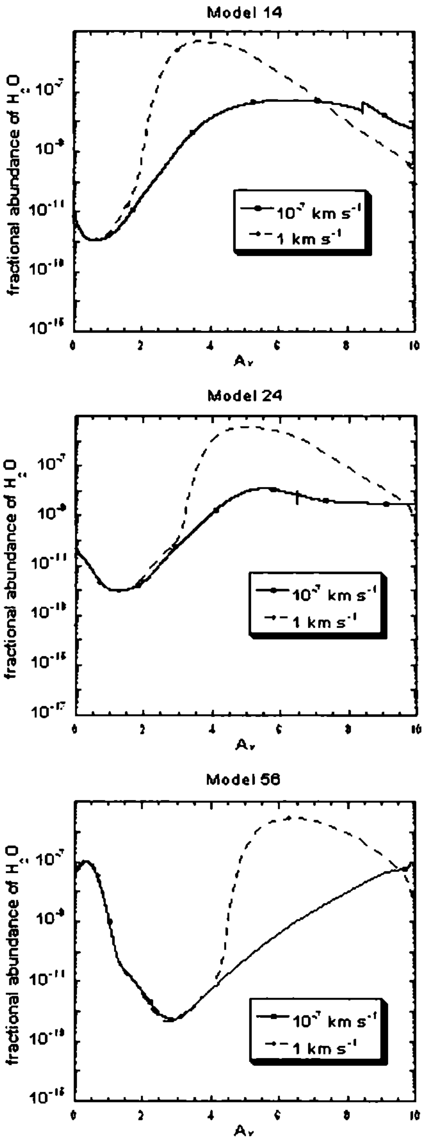

Figure 7.12: The abundance profile of H_2O for models 14, 24 and 56 in stationary and nonstationary modes. The abundance is relative to n_H for each model and $n_H = 10^4$ cm^{-3} for Models 14 and 24 and $n_H = 10^6$cm^{-3} for Model 56.

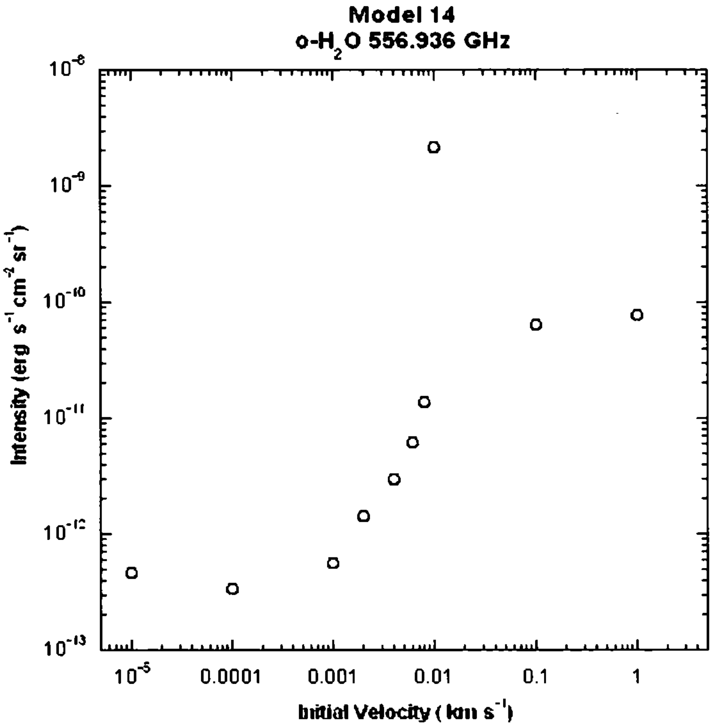

Figure 7.13: Intensity of o-H_2O 556.936 GHz line for initial velocities $10^{-5}, 10^{-4}, 10^{-3}, 2\times10^{-3}, 4\times10^{-3}, 6\times10^{-3}, 8\times10^{-3}, 10^{-2}, 10^{-1}$ and $1\,\mathrm{km\,s^{-1}}$.

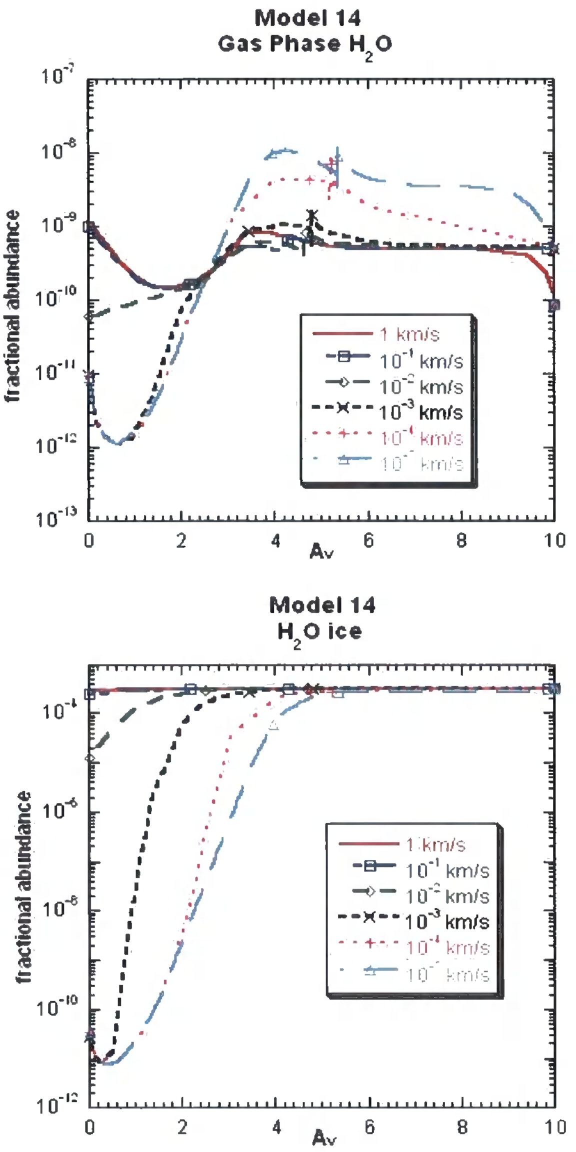

Figure 7.14: Abundance profiles of gas phase (top panel) and solid phase (bottom panel) H_2O for Model 14 for the range of initial velocities between 10^{-5} and $1\,\mathrm{km\,s^{-1}}$. The abundances are relative to $n_{\mathrm{H}} = 10^4\,\mathrm{cm^{-3}}$.

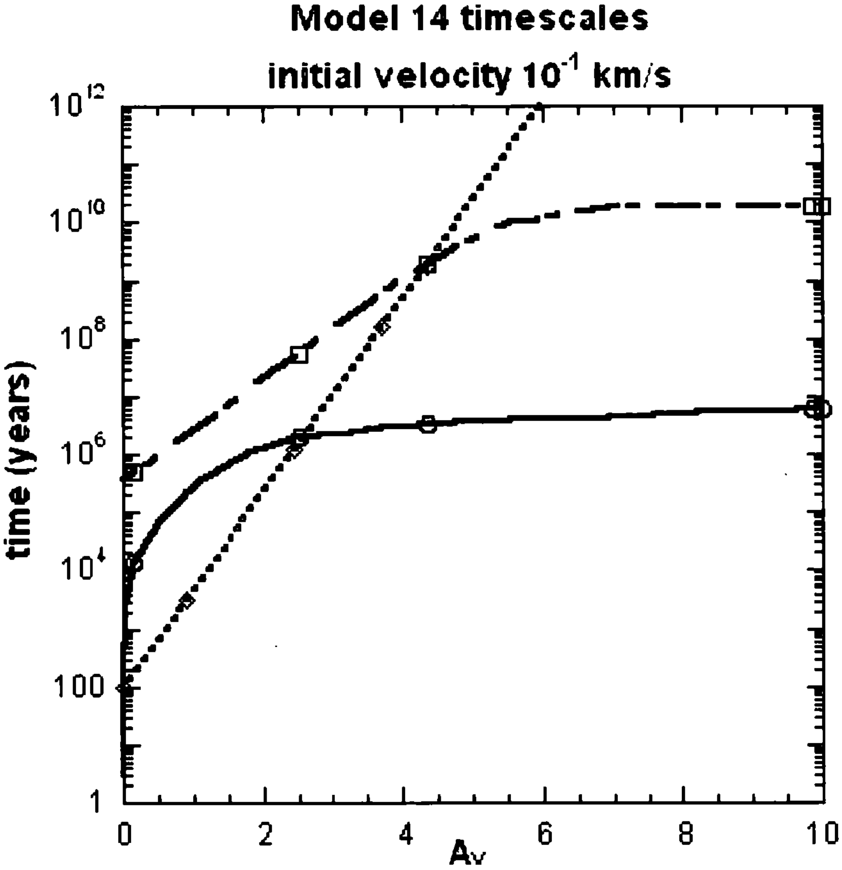

Figure 7.15: The comparison of dynamical timescale to chemical timescales for initial velocity of 10^{-1} km s^{-1} for Model 14. The solid curve shows the dynamical timescale, dotted curve shows the timescale of photodissociation of H_2O and dashed curve shows the timescale of photodesorption of H_2O ice.

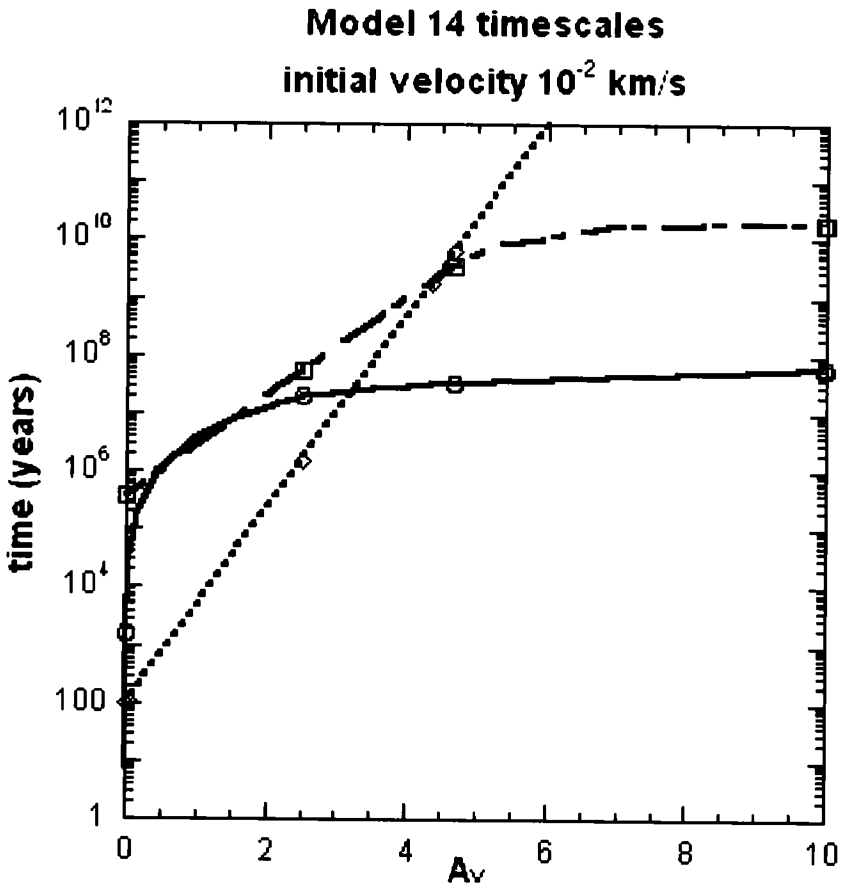

Figure 7.16: The comparison of dynamical timescale to chemical timescales for initial velocity of 10^{-2} km s^{-1} for Model 14. The solid curve shows the dynamical timescale, dotted curve shows the timescale of photodissociation of H_2O and dashed curve shows the timescale of photodesorption of H_2O ice.

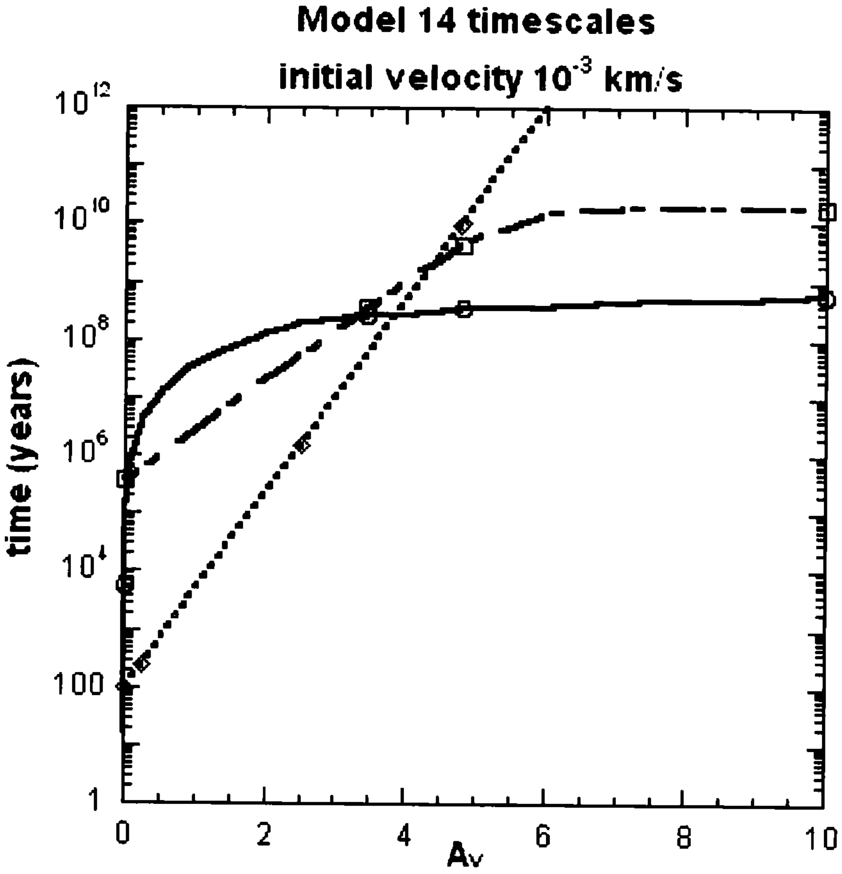

Figure 7.17: The comparison of dynamical timescale to chemical timescales for initial velocity of 10^{-3} km s^{-1} for Model 14. The solid curve shows the dynamical timescale, dotted curve shows the timescale of photodissociation of H_2O and dashed curve shows the timescale of photodesorption of H_2O ice.

7.3 Comparison

Bergin et al. (2003) examined NGC 1333 using SWAS. NGC 1333 is a well known reflection nebula. They suggested that the observed emission of o-H_2O 557 GHz towards several positions in NGC 1333 can be reproduced by PDR models. They found, for SS 5, the observed integrated intensity is 0.19 ± 0.02 K km/s. The average abundance of gas phase H_2O has been found as $X(H_2O) = 1.8 \times 10^{-7}$ for their PDR model based on Tielens and Hollenbach (1985) and Kaufman et al. (1999) with parameters, $n_{H_2} = 2 \times 10^4\,\mathrm{cm}^{-3}$ and $G_0 = 100$. Our corresponding model, Model 24, yields an average abundance value, $X(H_2O) = 1.7 \times 10^{-7}$ for an initial velocity of $1\,\mathrm{km\,s}^{-1}$, whereas the result obtained from stationary case yields $X(H_2O) = 4.1 \times 10^{-9}$. They have assumed that H_2O does not freeze-out on the grains in the low density gas, so the freeze-out in our model has been removed for comparison purpose. The total hydrogen density has been assumed to be $n_H = 10^4\,\mathrm{cm}^{-3}$. This model gave the most consistent average relative abundance of H_2O for initial velocity of $0.7\,\mathrm{km\,s}^{-1}$, which is found to be 1.8×10^{-7}. The line intensity of o-H_2O has been found to be $2.72 \times 10^{-15}\,\mathrm{erg\,s^{-1}\,cm^{-2}}$ for the SWAS beam of $3.3' \times 4.5'$. This is a factor of $\sim$ 16 lower compared to the value $4.48 \times 10^{-14}\,\mathrm{erg\,s^{-1}\,cm^{-2}}$ that the observed integrated intensity 0.19 K km/s corresponds to. This discrepancy may be due to the chosen initial velocity which determines the order of magnitude in $1\,\mathrm{km\,s}^{-1}$ of the flow velocity through the PDR. Increasing the flow velocity, will result in an increased abundance of gas phase H_2O and would increase the resulting line intensity, however, other species that are involved in contribution to the abundance of gas phase H_2O will be effected by shortened dynamical timescale, as well. At low temperatures, the dissociative recombination of H_3O^+ produces H_2O. Photodesorption of H_2O ice is another mechanism that contributes to the gas phase H_2O. On the other hand, determining the temperature of the gas is a common problem of PDR modelling. The dust temperature in our models are derived from the gas temperature, and the photodesorption yield depends on the dust temperature. Therefore, more accurate, fully self-consistent treatment of gas temperature is needed to be included in our advection models in order to carry out further investigations.

There are other theoretical studies attempted to model the observed line intensities in the PDRs as mentioned in Sections 2.1 and 5.1, on line intensities of H_2O, however, the direct comparison of our results with those models is not possible since they do not include the self-consistent dynamics and advection flows. The future observations of PDRs will be useful in comparing our predictions to the observed line intensities for other lines of H_2O.

Chapter 8

Observational Work-NO Depletion in L1544 and L183

8.1 Introduction

Depletion of elements has long been thought to be important in the early stages of star formation. The dynamical status of the protostellar object can be inferred from the chemical evolution and depletion of elements. Therefore, understanding the depletion is crucial in determining the structure of pre-protostellar cores just prior to collapse.

On the other hand, molecular line emission provides information about the kinematics of prestellar cores. However, C-containing species deplete onto dust grain surfaces in the central region. N-containing species (in particular NH_3 and N_2H^+) show a different behaviour and they remain in the gas phase at higher densities.

Whether OH and H_2O are present in gas phase at higher densities is not known. There are observational constraints on the problem which would be solved by the improvements in observational facilities. HIFI and HERSCHEL may resolve this and observe OH and H_2O which are difficult to observe from ground-based facilities due to the reasons explained in Chapter 3.

Until the space-based observational facilities provide more detailed information about H_2O in star forming cores, we have to think of other ways to approach this problem. According to the present chemical models, the abundance of NO reflects more or less the OH abundance. Furthermore, NO is a key molecule in nitrogen chemistry.

In order to understand the depletion characteristics of NO and whether it can be suggested as a tracer, the dependence of NO abundance on position in the pre-protostellar cores was investigated. In this chapter, this observational work is presented in detail and the results are discussed. This chapter is based on the publication Akyilmaz et al. (2007).

8.2 Depletion and chemistry in prestellar cores

The structure of the star forming regions is determined by the interplay of the chemical reactions that involve the depletion of chemical species on the grains. In the interior of cold molecular clouds, most molecules except the ones bearing only H and some N-containing species are expected to deplete on to the grains and eventually disappear from gas phase. C-containing species deplete on to dust grain surfaces in the central, high density regions of prestellar cores. The information provided by molecular line emissions is necessary to understand the kinematics of the prestellar cores. The fact that the most C-containing species trace only the outer shell of the prestellar cores but not the high-density interior ($n_{\rm H} \gtrsim 3 \times 10^4\,{\rm cm}^{-3}$) limits our understanding. The reader is notified that there has been a recent study on CN in L1544 and L183 and CN has been found to be only C-containing species that does not show depletion characteristics similar to other C species (Hily-Blant et al., 2008).

However, N-containing species do not show the same behaviour, i.e., they manage to survive in the gas phase up to densities of a few times 10^5 cm^{-3}. For example, Belloche and André (2004) suggested that N_2H^+ ion disappears from the gas phase above a density of $n_{\rm H_2} \sim 4-7 \times 10^5\,{\rm cm}^{-3}$ in the envelope of the object IRAM 04191. The N-containing species seem to disappear from gas phase when $n_{\rm H} \gtrsim 10^6\,{\rm cm}^{-3}$ (Pagani et al., 2005, and references therein). The survival of N-containing species up to higher densities was originally attributed to the relatively high volatility of N_2 on grain surfaces (Bergin and Langer, 1997; Aikawa et al., 2001), but recent laboratory measurements (Öberg and Schlemmer, 2005; Bisschop et al., 2006) show that N_2 is only marginally more volatile than CO. This result throws doubt on much recent modelling of the chemistry of prestellar cores and poses the question of whether another more volatile and abundant form of nitrogen is responsible for the survival of N-containing species to high density. The low sticking coefficients for either molecular or atomic N can be an alternative explanation. Flower et al. (2005, 2006) found that low sticking coefficients for both atomic N and O provide the best fit of the models to the observed abundances of NH_3 and N_2H^+ although this needs experimental confirmation.

As mentioned in earlier sections, OH and H_2O are important species in the interstellar medium and star formation. It is not known whether O-containing species, such as OH and H_2O deplete at high densities since determining the abundances of these species in cold clouds are difficult due to the observational limitations (Goldsmith and Li, 2005; Bergin and Snell, 2002). The future observations of H_2O with HIFI onboard Herschel or of OH with the Square Kilometer Array (SKA) may resolve this and provide answers to whether O-containing species survive in the gas phase in the regions where N_2H^+ and NH_3 observed. However, by the time the future facilities are ready, the alternative observational strategies need to be considered. The chemical models of prestellar cores can be used as a guide to develop these alternative strategies. If the sticking probability of atomic oxygen is not larger than that of atomic nitrogen, then OH and H_2O might be expected to survive in the gas phase where N_2H^+ and NH_3 are found in the gas phase.

An important aspect of this problem involves NO. NO is believed to be a key molecule in the nitrogen chemistry which mediates the transformation of atomic into molecular nitrogen.

$$\mathrm{N} + \mathrm{OH} \rightarrow \mathrm{H} + \mathrm{NO} \tag{8.1}$$

$$\mathrm{N} + \mathrm{NO} \rightarrow \mathrm{O} + \mathrm{N_2} \qquad (8.2)$$

Assuming that the reactions 8.1 and 8.2 dominate the formation and destruction of NO, respectively, the ratio of the abundance of NO and to that of OH is simply equal to the ratio of the rate coefficients for these reactions, $k_1/k_2 \approx 1$ providing that there are no energy barriers to these reactions, which might reduce differentially the values of their rate coefficients at low temperatures. Under the conditions that the above equation holds, NO can be considered as a proxy for OH, and therefore, it can provide information on O-containing species in the gas phase.

NO is one of the most abundant nitrogenated molecules in the interstellar medium. It has been previously detected at millimeter wavelengths in both dark and cold clouds. It was observed in L183 and fractional abundance of NO was found to be around 10^{-7} (Gerin and Ellinger, 1992; Gerin and Casoli, 1993). The value quoted by these authors was based on the $C^{18}O$ column density. CO is known to be depleted in L183 (Pagani et al., 2004, 2005), hence the value for the fractional abundance of NO was an overestimate. However, it is still high that makes NO suitable and the spatial variation of it worth investigating for, in the cores L183 and L1544. The objective was to compare the spatial variation of NO and H_2. The dust emission maps are available for both L183 and L1544, from which the estimates of the column densities of molecular hydrogen $N(H_2)$ can be inferred. The $N_2H^+(1-0)$ was observed simultaneously, since it is known to follow roughly the dust emission.

8.3 The rotational structure of NO molecule

In this section, the molecular structure of NO molecule will be given in detail in the context of rotational levels. Each rotational level J is split into two single rotational levels of opposite parity, '+' and '−', due to the coupling of electronic angular momentum and the rotation of the nuclei. Only the transitions between levels of opposite parity are allowed by the selection rule for electric dipole transitions. Therefore, there are two series of transitions called Π^+ and Π^- connecting the Π^+ and Π^- levels, respectively.

The hyperfine splitting is due to the interaction of the magnetic moment and the electric quadrupole moment of the nitrogen nucleus with the electrons. The hyperfine levels are characterized by quantum number F which arises from the coupling of the nuclear spin vector I and the total angular momentum J. F takes the values between $\mid I - J \mid$ and $\mid I + J \mid$ and has a statistical weight $g_F = 2F + 1$. Selection rules for electric dipole transitions between hyperfine levels are $\Delta J = \pm 1$ and $\Delta F = 0, \pm 1$ giving rise to 5 hyperfine components for the transition $J = 3/2 \rightarrow 1/2$ and 6 hyperfine components for the transition $J = 5/2 \rightarrow 3/2$.

Table 8.1 shows the parameters of the hyperfine transitions of NO (Gerin and Ellinger, 1992, and references therein). The parameters appearing in the table will be explained in more detail in Section 8.5.2.

Transition $J'F' \rightarrow J''F''$	Frequency (MHZ)	$S_{J'J''}$	$A_{J'J''}$ (s^-1)	$g_{J'}$	$S_{F'F''}$	$A_{J'F',J''F''}$ (s^-1)	$g_{F'}$	$E_{J'F'}$ (K)
Π^+ band								
$3/2, 5/2 \rightarrow 1/2, 3/2$	150176.46	4/3	3.34(-7)	4	0.500	1.10(−7)	6	7.2070
$3/2, 3/2 \rightarrow 1/2, 1/2$	150198.76				0.186	6.13(−8)	4	7.2090
$3/2, 3/2 \rightarrow 1/2, 3/2$	150218.74				0.148	4.91(−8)	4	7.2090
$3/2, 1/2 \rightarrow 1/2, 1/2$	150225.65				0.148	9.82(−8)	2	7.2103
$3/2, 1/2 \rightarrow 1/2, 3/2$	150245.64				0.018	1.23(−8)	2	7.2103
Π^- band								
$3/2, 1/2 \rightarrow 1/2, 3/2$	150375.30	4/3	3.34(-7)	4	0.018	1.23(−8)	2	7.2372
$3/2, 3/2 \rightarrow 1/2, 3/2$	150439.10				0.148	4.93(−8)	4	7.2402
$3/2, 5/2 \rightarrow 1/2, 3/2$	150546.46				0.500	1.11(−7)	6	7.2454
$3/2, 1/2 \rightarrow 1/2, 1/2$	150580.55				0.148	9.89(−8)	2	7.2372
$3/2, 3/2 \rightarrow 1/2, 1/2$	150644.35				0.186	6.19(−8)	4	7.2402
Π^+ band								
$5/2, 7/2 \rightarrow 3/2, 5/2$	250436.84	2.4	1.84(-6)	6	0.445	6.14(−7)	8	19.2254
$5/2, 5/2 \rightarrow 3/2, 3/2$	250440.66				0.280	5.16(−7)	6	19.2276
$5/2, 3/2 \rightarrow 3/2, 1/2$	250448.53				0.167	4.61(−7)	4	19.2292
$5/2, 3/2 \rightarrow 3/2, 3/2$	250475.42				0.053	1.47(−7)	4	19.2292
$5/2, 5/2 \rightarrow 3/2, 5/2$	250482.94				0.053	9.83(−8)	6	19.2276
$5/2, 3/2 \rightarrow 3/2, 5/2$	250517.71				0.002	6.15(−9)	4	19.2292
Π^- band								
$5/2, 3/2 \rightarrow 3/2, 5/2$	250645.77	2.4	1.84(-6)	6	0.002	6.16(−9)	4	19.2739
$5/2, 5/2 \rightarrow 3/2, 5/2$	250708.24				0.053	9.86(−8)	6	19.2768
$5/2, 3/2 \rightarrow 3/2, 3/2$	250753.14				0.053	1.48(−7)	4	19.2739
*$5/2, 7/2 \rightarrow 3/2, 5/2$	250796.43				0.445	6.17(−7)	8	19.2811
*$5/2, 5/2 \rightarrow 3/2, 3/2$	250815.61				0.280	5.18(−7)	6	19.2768
$5/2, 3/2 \rightarrow 3/2, 1/2$	250816.93				0.167	4.63(−7)	4	19.2739

Table 8.1: Parameters of the hyperfine transitions of NO (Gerin and Ellinger, 1992). a(-b) denotes a $\times 10^{-b}$.

8.4 Observations

The observations were carried out in two runs, in July and August 2005, using the IRAM 30m telescope. The 3 mm, 2 mm and 1.3 mm receivers, A100, D150 and D270, respectively, were used simultaneously. The 3 mm receiver was tuned to the N_2H^+ J = 1 → 0 93.17632 GHz line, the 2 mm receiver to the centre of the NO $J = 3/2 \rightarrow 1/2\,\Pi^+$ and Π^- transitions at 150.36146 GHz and the 1.3 mm receiver to the centre of the NO $J = 5/2 \rightarrow 3/2\,\Pi^+$ and Π^- transitions at 250.61664 GHz. The half-power beam widths (HPBW″) are obtained by using the relation

$$\text{HPBW}'' = 2460/\text{Frequency(GHz)} \tag{8.3}$$

which for the frequencies above gives 27″, 16″ and 10″, respectively. The corresponding main-beam efficiencies are 0.78, 0.68 and 0.48. Pointing was checked at intervals of roughly two hours and was found to be accurate within 2″. We used central positions (J2000) of RA = $05^h04^m16^s.9$, Dec = $25°10'47''.7$ for L1544 and RA = $15^h54^m08^s.8$, Dec = $-02°52'44''.0$ for L183, and the offsets specified below are with respect to these positions.

The facility SIS receivers were used in frequency-switching mode with system temperatures of 150 – 180 K at 3 mm, 350 – 450 K at 2 mm, and 1000 – 2000 K at 1.3 mm. At 3 mm, the facility VESPA autocorrelator was used as a spectral backend with 20 kHz channel spacing over a 20 MHz bandwidth, allowing us to cover all 7 hyperfine satellites of the N_2H^+ (J = 1 → 0) transition. At 2 mm and at 1.3 mm, the NO lines are too widely

Receiver	Resolution (kHz)	Bandwidth (MHz)	Frequency (GHz)	Transition
A100	20	20	93.176265	N_2H^+ J = 1 → 0
D150	20	20	150.17646	NO Π^+ J = 3/2 → 1/2, F = 5/2 → 3/2
D150	20	20	150.54646	NO Π^- J = 3/2 → 1/2, F = 5/2 → 3/2
D270	40	40	250.43684	NO Π^+ J = 5/2 → 3/2, F = 7/2 → 5/2
D270	40	40	250.79643	NO Π^- J = 5/2 → 3/2, F = 7/2 → 5/2
D150	20	20	150.19876	NO Π^+ J = 3/2 → 1/2, F = 3/2 → 1/2
D150	20	20	150.21874	NO Π^+ J = 3/2 → 1/2, F = 3/2 → 3/2
D150	20	20	150.22565	NO Π^+ J = 3/2 → 1/2, F = 1/2 → 1/2
D150	20	20	150.58055	NO Π^- J = 3/2 → 1/2, F = 1/2 → 1/2
D270	40	40	250.81561	NO Π^- J = 5/2 → 3/2, F = 5/2 → 3/2

Table 8.2: The transitions observed and the corresponding autocorrelator splitting.

separated to be covered in one band with adequate resolution. Therefore, VESPA was split into 6 parts of 20 MHz bandwidth with 20 kHz resolution at 2 mm and 3 parts with 40 MHz bandwidth and 40 kHz resolution at 1.3 mm. The list of observed transitions and the details of autocorrelator splitting are summarized in Table 8.2. The data were processed by using the GILDAS (Grenoble Image and Line Data Analysis System) package [1].

8.5 Results

8.5.1 The Observed Line Intensities

In the time available, rather than attempting to map the sources L1544 and L183, we observed NO emission along two orthogonal cuts in L1544 and one cut in L183 chosen according to the total column density distributions represented by the dust maps. For L1544 the observed cuts correspond to the major and minor axes of the dust emission, which are along NW-SE and

---

[1] Mainly CLASS was used.

NE-SW directions of the source, respectively [2]. For L183, only one cut along R.A., i.e., E-W direction was observed due to the total time available for this source. The line intensities of NO transitions observed towards the centre of both L1544 and L183 are summarised in Table 8.3. The 250 GHz lines have larger noise levels compared to the 150 GHz lines. For L1544, the parameters in Table 8.3 are obtained by using the fixed width method in CLASS and fixing the line width to that of 150.17646 GHz lines.

---

[2] N, S, E and W denote the directions North, South, East and West in Equatorial Coordinate system, respectively

Frequency GHz	Integrated Intensity K km s^{-1}	V_{lsr} km s^{-1}	Δv km s^{-1}
L1544			
150.17646	0.22(0.02)	7.18(0.01)	0.38(0.02)
150.19876	0.09(0.01)	7.14(0.02)	0.35(0.04)
150.21874	0.05(0.01)	7.12(0.02)	0.30(0.04)
150.22565	0.06(0.01)	7.12(0.02)	0.26(0.04)
150.54646	0.20(0.01)	7.11(0.01)	0.34(0.02)
150.58055	0.04(0.01)	7.13(0.03)	0.34(0.06)
250.43684	0.26(0.04)	7.28(0.05)	0.38
250.79643	0.22(0.04)	7.26(0.04)	0.38
L183			
150.17646	0.47(0.02)	2.37(0.01)	0.38(0.02)
150.19876	0.18(0.02)	2.37(0.02)	0.44(0.04)
150.21874	0.14(0.01)	2.29(0.02)	0.38(0.04)
150.22565	0.14(0.01)	2.35(0.02)	0.32(0.04)
150.54646	0.46(0.02)	2.38(0.01)	0.38(0.02)
150.58055	0.12(0.01)	2.38(0.02)	0.29(0.04)
250.43684	0.27(0.06)	2.33(0.01)	0.11(0.03)
250.79643	0.32(0.06)	2.38(0.02)	0.27(0.06)

Table 8.3: NO transitions observed towards the central positions of L1544 and L183 with uncertainties in parentheses. For L1544, the linewidths of the 150 GHz transitions were determined by using the Gaussian fit available with CLASS of GILDAS package, the linewidths of the 250 GHz lines were fixed to that of the 150.17646 GHz transition due to the noise level of these lines.

8.5.2 Determination of column densities

NO

The determination of column densities were carried out using the method described by Gerin and Ellinger (1992). Provided that the emission line is optically thin, for a transition $J', F' \rightarrow J'', F''$ the column density of NO molecules in the upper level J', F' can be obtained directly from the integrated intensity of the main beam brightness temperature using

$$N(J', F') = \frac{8\pi k}{hc^3} \frac{\nu^2_{J'F',J''F''}}{A_{J'F',J''F''}} \frac{10^5}{(1 - J_{\nu_0}(T_{BG})/J_{\nu_0}(T_{ex}))} \int T_R dV, \tag{8.4}$$

where

$$J_{\nu_0}(T) = \frac{h\nu_0}{k} \frac{1}{\exp(\frac{h\nu_0}{kT}) - 1} \tag{8.5}$$

and $T_{BG} = 2.7$ K is the background radiation temperature, T_{ex} is the excitation temperature of the transition, $\nu_0 = \nu_{J'F',J''F''}$ and the transition probability between two hyperfine levels is

$$A_{J'F',J''F''} = \frac{64\pi^4}{3hc^3} \nu^3_{J'F',J''F''} \frac{\mu^2}{2F' + 1} S_{J'J''} S_{F'F''} \tag{8.6}$$

$S_{J'J''}$ is the rotational line strength and $S_{F'F''}$ is a dimensionless factor which obeys the sum rules as follows

$$\sum_{F'}\sum_{F''} S_{F'F''} = 1$$

$$\sum_{F''} S_{F'F''} = \frac{2F'+1}{(2I+1)(2J'+1)}$$

$$\sum_{F'} S_{F'F''} = \frac{2F''+1}{(2I+1)(2J''+1)}.$$

Assuming that the population of levels obeys Boltzmann law at the kinetic temperature of the cloud T_{kin}, in the optically thin LTE(Local Thermal Equilibrium) limit, the total column density N_{tot} can be calculated using

$$N_{tot} = \frac{N(J',F')}{g_{F'}} Q_{rot}(T_{kin})\mathrm{exp}\left[\frac{E(J',F')}{kT_{kin}}\right] \tag{8.7}$$

where Q_{rot} is the rotational partition function,

$$Q_{rot} = \sum_{\Sigma}\sum_{p}\sum_{J,F} g_F \mathrm{exp}\left[\frac{E(J',F')}{kT_{kin}}\right]. \tag{8.8}$$

The relative intensities of the different hyperfine components are observed to be close to the values expected on the basis of the line strengths given in Table 8.1. This can be checked by comparing the ratios of the observed line intensities and of the strengths given in the table. The ratio between $J = 3/2 \rightarrow 1/2, F = 3/2 \rightarrow 1/2$ and $J = 3/2 \rightarrow 1/2, F = 5/2 \rightarrow 3/2$ is 0.37 according to the Table 8.1. Averaging the transitions from Π^+ and Π^- bands, the ratio was obtained to be 0.46±0.07 at the central position of L1544 which corresponds to the offset (0,0). Similarly, the ratio of the average of the three 2 mm lines with strength 0.148 in Table 8.1 to the two lines with strength

0.500 is measured to be 0.30 ± 0.04, as compared with 0.30 [3]. The intensities of the NO hyperfine components are almost consistent, to within the error bars, with the low optical depth limit. Therefore, the intensities of the NO 150 GHz (2 mm) can be expected to yield a good approximation to the true NO column density distribution. The averaged integrated intensity $I(2\,\mathrm{mm})$ of the $J = 3/2 \rightarrow 1/2, F = 5/2 \rightarrow 3/2$ transitions in Π^+ and Π^- bands can be converted into the NO column density for a given T_{ex}.

The calculations of the rate coefficients for rotational transitions of NO, induced by H_2 are not yet available to the best of our knowledge. However, the calculations for OH-H_2 which shares many physical characteristics with NO-H_2 have been carried out by Offer and van Dishoeck (1992). The rate coefficient for rotational de-excitation at $T = 50$ K is of the order of 10^{-11} cm^3 s^{-1} and not strongly dependent on T_{kin}. The rate of spontaneous radiative decay is of order of 10^{-7} (Table 8.1) which implies a critical density of H_2 of the order of 10^4 cm^{-3}. In this case, it is reasonable to assume that the NO levels of interest here are thermalized. Based on the NH_3 results of Tafalla et al. (2002) for L1544 and Ungerechts et al. (1980) for L183 T_{ex} is assumed to be 8.75 K and 9 K, respectively. More recently, the gas temperature in the core center of L183 has been predicted to be (7 ± 1) K by using a non-LTE Monte Carlo code (Pagani et al., 2007) and the gas has been found to be thermalized with the dust [4].

---

[3] Averaging procedure was carried out using CLASS.

[4] This study was not available at the time that our observational work was being carried out and the results were published.

An independent check of the NO excitation in L1544 is provided by our own measurements of the $J = 5/2 \rightarrow 3/2$ 250 GHz lines. The ratio of intensities of 250 GHz lines to 150 GHz lines are $I(1.2\,\mathrm{mm})/\mathrm{I}(2\,\mathrm{mm}) = 1.14 \pm 0.25$ from the Table 8.3 where a 15 percent of calibration error was assumed in addition to the formal errors given in the table [5]. Using the formulation of Gerin and Ellinger (1992), and assuming that LTE approach holds and the level populations obey Boltzmann law, the corresponding excitation temperature between the $J = 5/2$ and $J = 3/2$ levels is found to be 13.5 ± 4 K, which is higher than the single-dish NH_3 measurement, but consistent with it, to within the combined error bars.

Therefore, for the excitation temperatures 8.75 K and 9 K for L1544 and L183, respectively, the column density of NO cm^{-2} in L1544 and L183 can be approximately given by

$$N(\mathrm{NO}) = 4.3 \times 10^{15}\mathrm{I}(2\,\mathrm{mm}) \tag{8.9}$$

where $I(2\,\mathrm{mm})$ is the integrated intensity of NO 2 mm (150 GHz) lines in $\mathrm{K\,km\,s^{-1}}$. The integrated intensities of the strongest transitions in Π^+ and Π^- bands are given in Table 8.4.

---

[5] The $I(1.2\,\mathrm{mm})$ is the average of the integrated intensities of the two $J = 5/2 \rightarrow 3/2, F = 7/2 \rightarrow 5/2$ transitions.

R.A. Offset arcsec	Dec. Offset arcsec	$\Pi^{+} J = 3/2 \rightarrow 1/2, F = 5/2 \rightarrow 3/2$ Integrated intensity Kkms^{-1}	$\Pi^{-} J = 3/2 \rightarrow 1/2, F = 5/2 \rightarrow 3/2$ Integrated intensity Kkms^{-1}	Averaged Integrated Intensity Kkms^{-1}
L1544 NW-SE				
120.00	-120.00	0.038(0.007)	0.047(0.007)	0.044(0.005)
100.00	-100.00	0.063(0.008)	0.618(0.010)	0.062(0.007)
80.000	-80.000	0.080(0.010)	0.061(0.008)	0.070(0.007)
60.000	-60.000	0.117(0.010)	0.069(0.012)	0.095(0.007)
40.000	-40.000	0.173(0.009)	0.133(0.010)	0.156(0.007)
20.000	-20.000	0.168(0.010)	0.172(0.010)	0.169(0.007)
0.0000	0.0000	0.216(0.010)	0.199(0.010)	0.206(0.007)
-20.000	20.000	0.163(0.010)	0.176(0.011)	0.169(0.007)
-40.000	40.000	0.161(0.012)	0.152(0.011)	0.156(0.009)
-60.000	60.000	0.162(0.011)	0.145(0.012)	0.154(0.008)
-80.000	80.000	0.078(0.010)	0.102(0.016)	0.088(0.010)
-100.00	100.00	0.050(0.007)	0.065(0.016)	0.054(0.007)
-120.00	120.00	0.027(0.005)	0.020(0.007)	0.023(0.004)
-140.00	140.00	0.097(0.023)	0.081(0.010)	0.065(0.008)
L1544 NE-SW				
-80.000	-80.000	0.022(0.008)	0.023(0.008)	0.025(0.005)
-60.000	-60.000	0.019(0.005)	0.047(0.010)	0.030(0.005)
-40.000	-40.000	0.090(0.010)	0.100(0.011)	0.095(0.007)
-20.000	-20.000	0.225(0.011)	0.205(0.011)	0.214(0.008)
0.0000	0.0000	0.216(0.010)	0.199(0.010)	0.206(0.007)
20.000	20.000	0.214(0.012)	0.224(0.011)	0.218(0.008)
40.000	40.000	0.236(0.014)	0.190(0.014)	0.213(0.011)
60.000	60.000	0.218(0.010)	0.223(0.011)	0.219(0.008)
80.000	80.000	0.173(0.010)	0.164(0.010)	0.169(0.007)
100.00	100.00	0.115(0.010)	0.147(0.008)	0.131(0.005)
120.00	120.00	0.065(0.011)	0.073(0.010)	0.068(0.007)
140.00	140.00	0.027(0.010)	0.000(0.000)	0.022(0.005)
L183 E-W				
-100.00	0.0000	0.577(0.070)	0.599(0.082)	0.618(0.060)
-80.000	0.0000	0.578(0.088)	0.577(0.088)	0.577(0.063)
-60.000	0.0000	0.333(0.060)	0.363(0.059)	0.352(0.044)
-40.000	0.0000	0.641(0.070)	0.692(0.064)	0.665(0.045)
-20.000	0.0000	0.574(0.074)	0.565(0.066)	0.538(0.051)
0.0000	0.0000	1.170(0.067)	1.146(0.071)	1.137(0.055)
20.000	0.0000	1.369(0.142)	1.387(0.141)	1.365(0.078)
40.000	0.0000	1.127(0.171)	0.841(0.170)	1.003(0.119)
60.000	0.0000	0.589(0.077)	0.643(0.080)	0.610(0.059)
80.000	0.0000	0.440(0.090)	0.356(0.095)	0.394(0.063)

Table 8.4: The integrated intensities of strongest NO 2 mm (150 GHz) lines along the observed cuts in L1544 and L183. The integrated intensities and accompanied errors given in the parentheses were obtained using the Gaussian fits of CLASS procedure. Averaging the transitions $J = 3/2 \rightarrow 1/2, F = 5/2 \rightarrow 3/2$ in Π^{+} and Π^{-} bands were carried out by using CLASS.

N_2H^+

In addition to NO, N_2H^+ $J = 1 \rightarrow 0$ transition at 93.17632 GHz was observed to provide a means of check against pointing errors. To this end, the column density calculations of N_2H^+ were carried out and the values obtained were found to be consistent with the previous measurements.

The expressions for the total column density of N_2H^+ were given by Caselli et al. (2002) for both optically thick and thin limits. In the optically thick limit

$$\begin{aligned} N(\mathrm{N_2H^+}) &= \frac{4\pi\Delta\upsilon}{\lambda^3}\left(\frac{\pi}{\ln 2}\right)^{\frac{1}{2}}\frac{Q}{g_u A(u \rightarrow l)}\frac{\tau}{1-\exp(-\mathrm{h}\nu/\mathrm{kT_{ex}})} \\ &\times\frac{1}{\exp(-E_l/kT_{ex})} \end{aligned} \tag{8.10}$$

where $\Delta\upsilon$ is the full width half maximum of the line assuming that the line profile is Gaussian, the subscripts u and l denote the quantity at upper and lower levels, respectively, g_u is the degeneracy of the upper level of the observed transition, $A(u \rightarrow l)$ is the spontaneous radiation transition probability to the lower level, E_l is the excitation energy of the lower level and Q is the partition function. For rotational transitions, τ is the total optical depth.

The population of levels assumed to be characterized by Boltzmann distribution at an excitation temperature T_{ex}. In the optically thin limit, where the assumption of thermalization holds, the expression for the total column density becomes related to the main beam brightness temperature T_{mb} by

$$\begin{aligned} N(\mathrm{N_2H^+}) &= \frac{4\pi\Delta v}{\lambda^3}(\frac{\pi}{\ln 2})^{\frac{1}{2}}\frac{Q}{g_u A(u \rightarrow l)} \\ &\times \frac{kT_{mb}/h\nu}{[\exp(h\nu/kT_{ex})-1]^{-1}-[\exp(h\nu/kT_{bg})-1]^{-1}} \\ &\times \frac{1}{1-\exp(-h\nu/kT_{ex})}\frac{1}{\exp(-E_l/kT_{ex})} \end{aligned} \tag{8.11}$$

The integrated intensity for a Gaussian line is given by

$$W = \pi^{1/2}/\left[2(\ln 2)^{1/2}\right]\Delta v T_{mb}$$

The $J = 1 \rightarrow 0, F_1 = 1 \rightarrow 0, F = 0 \rightarrow 1$ transition is called weakest satellite and is expected to be the most optically thin component among all other hyperfine components of N_2H^+(1-0) multiplet. The relative strengths of these lines are given in Table 8.5.

Transition $J'F_1'F' \rightarrow JF_1F$	Line strength $S(F_1'F', F_1F)$
101 → 012	1/9
121 → 011	1/9
123 → 012	7/27
122 → 011	5/27
111 → 010	1/9
112 → 012	5/27
110 → 011	1/27

Table 8.5: The resolved hyperfine transitions of $J = 1 \rightarrow 0$ and the corresponding line strengths.

Some of the lines are optically thick towards the central positions of two objects observed. Accordingly, the weakest satellite has been used to derive the column density of N_2H^+. It has already been shown that Crapsi et al. (2005) the column densities derived in this way are consistent with the results obtained by using more sophisticated analyses of the emission in the rotational multiplet. Based on the previous work, the excitation temperature is assumed to be $T_{ex} = 5$ K.

The partition function Q is defined by

$$Q = \sum_i g_i \exp\left(-\frac{E_i}{kT_{ex}}\right) \tag{8.12}$$

which extends over all energy levels. $g_i = 2F_i + 1$ and the summation over g_i for each level of J is

$$Q = 9\sum_i g_J \exp\left(-\frac{E_J}{kT_{ex}}\right) \tag{8.13}$$

where $g_J = 2J+1$. The factor of 9 comes from the product of the degeneracies $2I + 1$ arising from the spin of the nitrogen nuclei. For a given value of J,

$$\sum_i (2F_i + 1) = 9(2J + 1) \tag{8.14}$$

The above explanation summarize the method used in determining the total column density of N_2H^+, however, the interested reader is referred to Akyilmaz et al. (2007) for a more detailed discussion regarding the degeneracies and hyperfine parameters.

Crapsi et al. (2005) using the weakest satellite and the optically thin approximation obtained the total column density $N(N_2H^+) = (1.83 \pm 0.19) \times$

10^{13} cm^{-2} which agrees within the error bar with the value obtained by Caselli et al. (2002), $N(\mathrm{N_2H^+}) = 2.0 \times 10^{13}$ cm^{-2}, using all resolved hyperfine components and corrected for the finite optical depths. At the central coordinate of our observation the total column density is found to be $N(\mathrm{N_2H^+}) = (2.54 \pm 0.51) \times 10^{13}$ cm^{-2} and the value provided by Crapsi (private communication) is $N(\mathrm{N_2H^+}) = (2.21 \pm 0.19) \times 10^{13}$ cm^{-2} at the corresponding position [6]. Therefore, the total column density derived from our observation data using the integrated intensity of the weakest satellite is consistent with the previously obtained value.

---

[6] The coordinates of the central position (J2000) that Crapsi et al. (2005) and Caselli et al. (2002) are R.A. = $05^{\mathrm{h}}04^{\mathrm{m}}15^{\mathrm{s}}.1$ and Dec = $25°11'08''$.

R.A. Offset	Dec. Offset	Integrated Intensity	Integrated Intensity
		101 → 012	110 → 011
arcsec	arcsec	Kkms^{-1}	Kkms^{-1}
L1544 Major Axis			
120.00	-120.00	0.000(0.000)	0.000(0.000)
100.00	-100.00	0.000(0.000)	0.000(0.000)
80.000	-80.000	0.005(0.004)	0.000(0.000)
60.000	-60.000	0.037(0.007)	0.024(0.010)
40.000	-40.000	0.305(0.044)	0.177(0.058)
20.000	-20.000	0.733(0.098)	0.442(0.123)
0.0000	0.0000	1.053(0.150)	0.626(0.205)
-20.000	20.000	0.962(0.136)	0.556(0.187)
-40.000	40.000	0.691(0.101)	0.395(0.136)
-60.000	60.000	0.035(0.053)	0.169(0.070)
-80.000	80.000	0.116(0.018)	0.062(0.022)
-100.00	100.00	0.050(0.010)	0.027(0.011)
-120.00	120.00	0.000(0.000)	0.000(0.000)
-140.00	140.00	0.000(0.000)	0.000(0.000)
L1544 Minor Axis			
-80.000	-80.000	0.000(0.000)	0.000(0.000)
-60.000	-60.000	0.006(0.004)	0.000(0.000)
-40.000	-40.000	0.053(0.011)	0.012(0.009)
-20.000	-20.000	0.518(0.075)	0.275(0.097)
0.000	0.000	1.053(0.150)	0.626(0.125)
20.000	20.000	0.456(0.068)	0.225(0.089)
40.000	40.000	0.279(0.043)	0.132(0.054)
60.000	60.000	0.216(0.033)	0.096(0.044)
80.000	80.000	0.086(0.017)	0.027(0.015)
100.00	100.00	0.037(0.009)	0.007(0.006)
120.00	120.00	0.000(0.000)	0.000(0.000)
140.00	140.00	0.000(0.000)	0.000(0.000)

Table 8.6: The observed integrated intensities of the isolated component $F_1 = 0 \rightarrow 1, F = 1 \rightarrow 2$ and the weakest satellite $F_1 = 1 \rightarrow 1, F = 0 \rightarrow 1$ of $N_2H^+ J = 1 \rightarrow 0$ multiplet. The r.m.s. errors are given in the parentheses.

8.6 Modelling the spatial distribution of NO

8.6.1 Introduction

Our observations indicate that unlike NH_3 and N_2H^+, NO does not show a constant or even an increasing abundance, relative to H_2 for densities $n_H \gtrsim 3 \times 10^5$ cm^{-3}. Instead, NO appears to decrease in relative abundance approaching the dust emission peak. In this section the modelling of the spatial distribution of NO and possible chemical explanations for this discrepancy are discussed.

Previous studies have considered prolate spheroid geometry for L1544 (Doty et al., 2005) and taken into account that the thermal pressure and the magnetic field strengths in estimating the collapse timescale. However, for the purpose of comparing observations of different chemical species and deducing the chemical and physical conditions in the cores, the relatively simple free-fall collapse model is adequate.

A simple empirical model was constructed in which the ratio x(NO) = N(NO)/N(H_2) was computed and n(NO)/n(H_2) was assumed to behave as a step function. x(NO) was found to decrease at a density $n(H_2) \approx 4 \times 10^5$cm^{-3}. Given that the characteristic densities for $C^{18}O$ and CS are 5.5×10^4 cm^{-3} and 1.7×10^5 cm^{-3} (Tafalla et al., 2002), respectively, NO is suggested to be intermediate in its depletion characteristics between the C-containing and N-containing species.

The chemical path from atomic to molecular nitrogen was also considered. The ratio of the abundance of NO to that of OH is given by the ratio of the rate coefficients of reactions 8.1 and 8.2, k_1/k_2, as was mentioned in Section 8.2. However, the rate coefficients for both of these reactions should be sufficiently large at low temperatures to ensure the conversion of atomic nitrogen into molecular nitrogen which is the precursor of N_2H^+ and NH_3. In other words, the above ratio does not apply when

$$n_{\rm H} k_{dep}({\rm NO}) = n({\rm N}) k_2$$

i.e., when the abundance of atomic nitrogen falls below the value for which the destruction of NO by N, has the same rate as direct depletion of NO on to the grains, where

$$k_{dep}({\rm NO}) = (n_g/n_{\rm H}) \pi a_g^2 v_{th}$$

Taking $T = 10$ K and $k_2 = 3.5 \times 10^{-11}$ cm^3 s^{-1} (Baulch, 2005) the value of $x({\rm N})$ is found to be 4×10^{-8} below which the NO is removed predominantly by freeze-out on to the grains.

One of the possible chemical explanations for the spatial distribution of NO observed in L1544 and L183 lies in the abundance of OH. OH may be under-abundant in the high density regions of at least some prestellar cores for the same reasons that keep O_2 and water under-abundant in those cores (Pagani et al., 2003; Snell et al., 2000).

The other chemical explanation is that there may be chemical pathways from N to N_2 which has been overlooked. Under conditions in which the gas-phase abundance of elemental carbon approaches that of elemental oxygen, the reactions

$$\mathrm{N + CH \rightarrow H + CN} \tag{8.15}$$

and

$$\mathrm{N + CN \rightarrow C + N_2} \tag{8.16}$$

assume importance relative to reactions 8.1 and 8.2.

In order to test some of the ideas above the calculations of the variation of NO, N_2H^+, and NH_3 with density was carried out in the framework of the free-fall collapse model presented by Flower et al. (2006). The details of this model are beyond the scope of this thesis, therefore the interested reader is referred to (Akyilmaz et al., 2007, and references therein) for more detailed discussions of the chemical considerations and calculations of the variation of above species using the free-fall collapse model. The conclusions derived from the models in an attempt to interpret the observed abundance of NO in L1544 and L183, however, are presented in the next section.

8.7 Conclusions

The observational results show that NO, unlike N_2H^+, and NH_3, is depleted towards the density peaks of the prestellar cores L1544 and L183. NO was believed to be an important intermediate of the nitrogen chemistry and the chemical pathway that converts atomic nitrogen into molecular nitrogen was believed to involve both OH and NO. Our results cast some doubt on these assumptions. CH and CN are proposed to be involved in the path from atomic to molecular nitrogen.

The prestellar core L1544 is likely to be "carbon-rich". In the gas phase, the assumption $n_C/n_O \approx 1$ yields good agreement with the observed upper limits than when the gas is oxygen-rich ($n_C/n_O = 0.67$). In case the gas-phase C/O abundance ratio is close to unity, the fractional abundances of C-rich species are expected to be enhanced relative to oxygen-containing species. L1544 shows this behaviour (Walmsley et al., 1980), however, L183 is relatively carbon-poor (Swade, 1989).

The ratio $n(N)/n(N_2)$ at the start of the collapse is found to be much more than its value in equilibrium. If $n(N)/n(N_2) \gg 1$ in the gas phase, then our observations of NO imply the existence of a small barrier ($\approx 25K$) to reaction 8.2. Experiments of neutral-neutral reactions 8.1, 8.15 and 8.16 are necessary to confirm the existence of a small barrier to these, however, they are very demanding at low temperatures.

The grain sticking probabilities of atomic C, N and, probably, O are significantly smaller than unity; values of $S(\mathrm{C}) = S(\mathrm{N}) = 0.1$ and $0.1 \leq S(\mathrm{O}) \leq 1.0$ were adopted in the model calculations. The assumed values of the sticking probabilities for the atomic species are ad hoc and require confirmation by means of experimental measurements.

Finally, the complete maps of NO distribution are required to study further L1544 and L183.

Chapter 9

Conclusions and Future Work

In this thesis, the theoretical work carried out to investigate the effects of advection in PDRs and the observational work carried out to investigate the spatial distribution of NO in pre-protostellar cores have been presented. In the following sections, the conclusions derived from the work covered in this thesis will be summarized. In addition to the concluding remarks, the possible areas of improvement in our PDR models and suggestions for future work will be discussed.

9.1 Advection in PDRs

Most PDR models assume steady-state, stationary conditions and some observations cannot be explained by the equilibrium PDR models. Self-consistent treatment of dynamics and advection are needed to be included in PDR models. To this end, the code developed by Walmsley et al. (1999) has been modified and updated in order to include self-consistent dynamics and adapt the most recent rate equations for a larger set of chemical species and reactions. H_2O is a key ingredient in the ISM and consequently, H_2O in PDRs receive a great attention in recent years since PDRs and H_2O will be the key science topics of upcoming Herschel observations. One of the goals of this work has been set as calculating the line intensities of H_2O in the PDRs where the material is advected. A parameter based study has been carried out producing ten models characterized by radiation χ (Draine, 1978) and density $n_{\rm H}$ parameters. For each model, the initial abundances at $A_v = 10$, the temperature profile and the photodissociation fits to H_2 and CO are obtained from corresponding Meudon-PDR code output. The output of Advection code has been coupled to the escape probability code developed by C. Ceccarelli (Ceccarelli et al., 2002). The results of this work can be summarized as follows

- The abundance profiles obtained by running Advection code in stationary mode (i.e., with an initial velocity of the order of $10^{-7}\,\mathrm{km\,s^{-1}}$) are in good agreement with those produced by Meudon-PDR code.

- Nonstationary results (i.e., with an initial velocity of the order of $1\,\mathrm{km\,s^{-1}}$) show that advection affects the PDR structure and abundance profiles of H_2O. The effects in the location of H/H_2 transition zone are significant when $\chi/n \leq 0.2 v_{IF}$ as suggested by Störzer and Hollenbach (1998). In all our nonstationary models, the flow velocity is larger at higher depths and it decreases as the material approaches the cloud surface (see Section 6.2.1). Therefore, the velocity near cloud surface may not be sufficiently large for the H/H_2 transition zone to completely disappear even though the condition given above seems to be satisfied for the value of initial velocity. Model 34 is a good example for this.

- The abundance profiles of H_2O are affected by advection even for Model 56, in which advection effects in PDR structure are the least. The average abundance of H_2O may be sensitive to the advection of material with a flow velocity of order of 1 $\mathrm{km\,s^{-1}}$. The average abundance of H_2O relative to n_H increases up to 2 orders of magnitude for Model 24 when run in nonstationary mode. Therefore, advection effects need to be considered in order to interpret the observational data obtained for H_2O.
- Rotational line intensities of H_2O are found to be sensitive to the order of magnitude of the flow velocity. The comparison of dynamical timescales to the chemical timescales of photodesorption of H_2O ice and photodissociation of H_2O has been carried out for Model 14 for a range of initial velocities from 10^{-5} $\mathrm{km\,s^{-1}}$ to 1 $\mathrm{km\,s^{-1}}$. The line intensities of o-H_2O 557 GHz transition has been found to vary up to 4 orders of magnitude. This suggests that comparison of advection models to the observational data can provide information about the characteristics of flow in nonequilibrium PDRs.
- For Model 24, the average abundance of H_2O is found to be in good agreement with that calculated by Bergin et al. (2003) for NGC 1333, SS 5. There is a factor of $\sim$ 16 discrepancy between the observed line

intensity of o-H_2O 557 GHZ transition and the model predictions for this line produced by Model 24. The suggestions for improvement will be discussed in the Section 9.3.

9.2 NO depletion in pre-protostellar cores

The observational part of this thesis involves the observations of NO and N_2H^+ in L1544 and L183 using IRAM-30m radio telescope. NO is a key molecule in nitrogen chemistry. The abundance of NO reflects the OH abundance. The investigation of spatial distribution of NO molecule in L1544 and L183 has been carried out. The main conclusion derived from this work can be summarized as NO unlike NH_3 and N_2H^+, has been found to be depleted towards the density peaks of prestellar cores L1544 and L183. This result casts doubt on the chemical models. CH and CN have been suggested to play role in formation of molecular nitrogen at high densities.

9.3 Future Work

It is concluded that the method used in this work produces reliable results which are in reasonable agreement with the results of previous works. Our approach of making use of three codes is an efficient way of including the complex treatment in our model considerations instead of attempting to create a single PDR code which includes all the input considerations included here and produces the line intensities. However, there are further improvements and investigations that can be suggested.

- One improvement can be done in computing the gas temperature. This can be done by including the energy balance, heating and cooling terms in Advection code. In this way, gas temperature can be calculated self-consistently and the effects of advection in temperature profile can be seen directly.

- The grain-grain collisions can be included in order to investigate the explosive desorption of chemical species from the grain mantles, as suggested by Le Bourlot et al. (1995). The rate of desorption is given in terms of turbulent velocity which is taken to be 1km s^{-1} in Le Bourlot et al. (1995), and effective cross section of grains.

- Our models can be applied to the famous PDRs (e.g., S140, Sgr B2, M17, Orion, Horsehead Nebulae) and the predictions for future Herschel HIFI observations can be carried out for specific objects.

- This work may be of general interest for the physical and chemical structure of molecular clouds since their envelopes can be considered as PDRs with higher density and lower radiation parameters. This parameter based study can be extended to include the radiation and density parameters which would be appropriate for molecular clouds.

As for observational work of NO in presetallar cores, the complete maps of NO of L1544 and L183 are necessary for further investigation of depletion characteristics of NO. To this end, the further observations of NO in other prestellar cores can be useful.

Appendices

Appendix A

Characteristics of PDR codes

Aikawa

Characteristics: Plane-parallel (semi-infinite) geometry, uni-directional radiation field, time-dependent chemistry solution, fixed number of species (577).

Output: abundance profiles, temperature profile.

Model has been presented in Lee et al. (1996).

Cloudy

Characteristics: Spherical , plane-parallel (semi-infinite and finite), circumstellar disk geometry, uni-directional radiation field, homogeneous and time-dependent density, time-dependent and stationary chemistry solutions, advection flow, fixed number of species (96), PAHs are included.

Output: abundance profiles, temperature profile, emitted intensities, heating and cooling rates, column density.

Model has been presented in Ferland et al. (1998); van Hoof et al. (2004);

Shaw et al. (2005).

COSTAR

Characteristics: Circumstellar disc geometry, uni-directional radiation field, stationary chemistry solution, fixed number of species (48).

Output: abundance profiles, temperature profile, column density.

Model has been presented in Kamp and Bertoldi (2000); Kamp and van Zadelhoff (2001).

HTBKW

Characteristics: Plane-parallel (semi-infinite and finite) geometry, uni-directional radiation field, homogeneous density, stationary chemistry solution, fixed number of species (46), PAHs included.

Output: abundance profiles, temperature profile, column density, emitted intensities, opacities at line centers.

Model has been presented in Tielens and Hollenbach (1985); Wolfire et al. (1990); Burton et al. (1990); Hollenbach et al. (1991); Kaufman et al. (1999).

KOSMA-τ

Characteristics: Spherical geometry, ensemble of clouds, isotropic radiation field, stationary chemistry solution, variable number of species, PAHs included.

Output: abundance profiles, column density, temperature profile, heating and cooling, chemical rates.

Model has been presented in Köster et al. (1994); Störzer et al. (1996); Zielinsky et al. (2000).

Lee96mod

Characteristics: Plane-parallel (semi-infinite) geometry, uni-directional radiation field, time-dependent chemistry solution, fixed number of species (419).

Output: abundance profiles.

Model has been presented in Lee et al. (1996).

Leiden

Characteristics: Plane-parallel (semi-infinite, finite) geometry, circumstellar disc, uni-directional radiation field, stationary chemistry solution, variable number of species, PAHs included.

Output: abundance profiles, temperature profile, emitted intensities, opacities at line centers, heating and cooling rates, chemical rates, excitation diagram of H_2.

Model has been presented in Black and van Dishoeck (1987); Jansen et al. (1995).

Meijerink

Characteristics: Plane-parallel (semi-infinite) geometry, uni-directional radiation field, stationary chemistry solution, variable number of species, PAHs included.

Output: abundance profiles, column density, temperature profile, emitted intensities, opacities at line center, heating and cooling, chemical rates.

Model has been presented in Meijerink and Spaans (2005).

Meudon

Characteristics: Plane-parallel (semi-infinite and finite), isotropic and unidirectional field, combination of isotropic and illuminating star, stationary chemistry solution, variable number of species, PAHs included.

Output: abundance profiles, temperature profile, emitted intensities, opacities at line centers, heating and cooling rates, chemical rates, excitation diagram of H_2.

Model has been presented in Abgrall et al. (1992); Le Bourlot et al. (1993); Le Petit et al. (2002).

Sternberg

Characteristics: Plane-parallel (semi-infinite) geometry, uni-directional radiation field, stationary chemistry solution, fixed number of species (78).

Output: abundance profiles, column density, temperature profile, emitted intensities, opacities at line center, heating and cooling, chemical rates, excitation diagram of H_2.

Model has been presented in Sternberg and Dalgarno (1995); Sternberg and Neufeld (1999).

UCL_PDR

Characteristics: Plane-parallel (semi-infinite) geometry, uni-directional radiation field, homogeneous and time-dependent density, time-dependent chemistry solution, fixed number of species (128).

Output: abundance profiles, temperature profile, heating and cooling rates, chemical rates, emitted intensities.

Model has been presented in Taylor et al. (1993); Papadopoulos et al. (2002).

Appendix B

Temperature fit parameters

Fits to the temperature profile produced by Meudon-PDR code take one of the forms below or a combination of them.

$$T = \frac{T_0}{a + bA_v + cA_v^2}$$

$$T = dA_v^2 + eA_v + f$$

Model 14

$0 < A_v \leqslant 2.5 \;\rightarrow\; T_0 = 70, a = 1, b = 2.57, c = -0.07$

$2.5 < A_v \leqslant 10 \;\rightarrow\; d = 0, e = 0.4, f = 9$

Model 34

$$T_0 = 620,\ a = 1, b = 6.97, c = -0.5$$

Model 54

$$0 < A_v \leqslant 0.7 \rightarrow T_0 = 70, d = -292.85, e = 386.43, f = 580$$

$$0.7 < A_v \leqslant 10 \rightarrow T_0 = 758, a = -1, b = 8.1, c = -0.2$$

Model 15

$$0 < A_v \leqslant 2.5 \rightarrow T_0 = 50, a = 1, b = 1.45, c = 0.05$$

$$2.5 < A_v \leqslant 10 \rightarrow d = 0, e = 0.0252, f = 10.037$$

Model 35

$$T_0 = 520, a = 1, b = 5.89, c = -0.39$$

Model 55

$$0 < A_v \leqslant 0.8 \rightarrow d = -406.7, e = 575.3, f = 1400$$

$$0.8 < A_v \leqslant 3.5 \rightarrow T_0 = 320, a = 1, b = 1.5, c = 0$$

$$3.5 < A_v \leqslant 10 \rightarrow d = 0, e = -2.83, f = 101.33$$

Model 16

$$0 < A_v \leqslant 2.5 \rightarrow T_0 = 50, a = 1, b = 2.38, c = -0.19$$

$$2.5 < A_v \leqslant 10 \rightarrow d = 0, e = -0.029, f = 8.74$$

Model 36

$$T_0 = 240, a = 1, b = 2.82, c = -0.19$$

Model 56

$$0 < A_v \leqslant 2.5 \rightarrow T_0 = 3100, a = 1, b = 0.47, c = 4.16$$

$$2.5 < A_v \leqslant 10 \rightarrow d = 0, e = -5.07, e = 122.7$$

Model 24

$$T_0 = 250, a = 1, b = 5.85, c = -0.46$$

Appendix C

Chemical rate equations

The reader should note that α, β and γ used in the expressions below may denote different physical parameters with different units for each particular reaction. Usage of these symbols is based on the standard convention which is used in setting up the chemistry files for PDR models.

Cosmic ray processes

The reaction rate is calculated as below

$$k = \gamma\zeta \, \mathrm{s}^{-1} \tag{C.1}$$

where ζ is the cosmic ray ionization rate which is usually of the order of $10^{-17}\,\mathrm{s}^{-1}$.

Secondary photon processes

The rates of processes involving secondary photons are given as

$$k = \gamma\zeta \left(\frac{T}{300}\right)^{\alpha} \frac{\mathrm{n(H_2)}}{\mathrm{n(H) + n(H_2)}} \quad \mathrm{s}^{-1} \qquad \text{(C.2)}$$

where T is the temperature of the gas, n(H) and n(H_2) are the abundances of atomic and molecular hydrogen, respectively. The details of how secondary photons are created in the interstellar clouds can be found in Prasad and Tarafdar (1983).

Gas phase reactions and radiative association

The rate of these reactions are implemented in the code using the rate equation below which is common to both types.

$$k = \gamma \left(\frac{T}{300}\right)^{\alpha} \exp(-\beta/T) \quad \mathrm{cm}^3\,\mathrm{s}^{-1} \qquad \text{(C.3)}$$

Photoreactions

The rate of the reactions involving photons is expressed as

$$k = \gamma\chi e^{-\beta A_v}\,\mathrm{s}^{-1} \qquad \text{(C.4)}$$

for a plane-parallel, semi-infinite slab illuminated on one side, where χ is the scaling factor of the radiation field with respect to that of Draine (Draine, 1978).

Adsorption on grains

The rate of adsorption reactions depends on the grain cross section per unit volume, $\langle \sigma n_g \rangle$ and the mean particle velocity, $\overline{v}$.

$$k = \gamma \langle \sigma n_g \rangle \overline{v} \quad \mathrm{s}^{-1} \tag{C.5}$$

The grain size distribution is taken into account in the calculation of the $\langle \sigma n_g \rangle$ as explained in Le Bourlot et al. (1995).

Formation of H_2 on grain surfaces

The formation rate was adopted from Viala et al. (1988) in the original version of the code [1].

$$k = \gamma \frac{n_H}{n(H)} \left(\frac{T}{300} \right)^{\alpha} \ \mathrm{cm}^3\,\mathrm{s}^{-1} \tag{C.6}$$

Thermal evaporation from grains

The rate for thermal evaporation is given by

$$k = \gamma \nu_0 \mathrm{exp}(-\beta / T_{gr}) \ \mathrm{cm}^3\,\mathrm{s}^{-1} \tag{C.7}$$

where ν_0 is the vibration frequency of the chemical species of interest.

---

[1] It has been kept as it is due to the numerical difficulties arose when the formation rate calculation was adopted from Meudon-PDR code. The test runs showed that keeping the H_2 formation rate as described in Equation C.6 yielded the results that were satisfactorily consistent with the output of Meudon-PDR.

Bibliography

H. Abgrall, J. Le Bourlot, G. Pineau Des Forets, E. Roueff, D. R. Flower, and L. Heck. *A&A*, 253:525, 1992.

Y. Aikawa, N. Ohashi, S.-i. Inutsuka, E. Herbst, and S. Takakuwa. *ApJ*, 552: 639, 2001.

M. Akyilmaz, D. R. Flower, P. Hily-Blant, G. Pineau Des Forêts, and C. M. Walmsley. *A&A*, 462:221, 2007.

E. L. O. Bakes and A. G. G. M. Tielens. *ApJ*, 499:258, 1998.

D. L. Baulch. *J. Phys. Chem. Ref. Data*, 34:757, 2005.

A. Belloche and P. André. *A&A*, 419:L35, 2004.

E. A. Bergin and W. D. Langer. *ApJ*, 486:316, 1997.

E. A. Bergin and R. L. Snell. *ApJ*, 581:L105, 2002.

E. A. Bergin, M. J. Kaufman, G. J. Melnick, R. L. Snell, and J. E. Howe. *ApJ*, 582:830, 2003.

P. Bernath. *Spectra of Atoms and Molecules.* Oxford University Press, Oxford, 2nd edition, 2005.

F. Bertoldi and B. T. Draine. *ApJ*, 458:222, 1996.

S. E. Bisschop, H. J. Fraser, K. I. Öberg, E. F. van Dishoeck, and S. Schlemmer. *A&A*, 449:1297, 2006.

J. H. Black and A. Dalgarno. *ApJS*, 34:405, 1977.

J. H. Black and A. Dalgarno. *ApJS*, 34:405, 1977.

J. H. Black and E. F. van Dishoeck. *ApJ*, 322:412, 1987.

J. H. Black, T. W. Hartquist, and A. Dalgarno. *ApJ*, 224:448, 1978.

M. G. Burton, D. J. Hollenbach, and A. G. G. M. Tielens. *ApJ*, 365:620, 1990.

P. Caselli, C. M. Walmsley, A. Zucconi, M. Tafalla, L. Dore, and P. C. Myers. *ApJ*, 565:344, 2002.

S. Casu, C. Cecchi-Pestellini, and S. Aiello. *MNRAS*, 325:826, 2001.

S. Cazaux and A. G. G. M. Tielens. *ApJ*, 604:222, 2004.

C. Ceccarelli, J.-P. Baluteau, M. Walmsley, B. M. Swinyard, E. Caux, S. D. Sidher, P. Cox, C. Gry, M. Kessler, and T. Prusti. *A&A*, 383:603, 2002.

J. Cernicharo, T. Lim, P. Cox, E. Gonzalez-Alfonso, E. Caux, B. M. Swinyard, J. Martin-Pintado, J. P. Baluteau, and P. Clegg. *A&A*, 323:L25, 1997.

A. C. Cheung, D. M. Rank, C. H. Townes, D. D. Thornton, and W. J. Welch. *Nature*, 221:626, 1969.

A. Coustenis, A. Salama, E. Lellouch, T. Encrenaz, G. L. Bjoraker, R. E. Samuelson, T. de Graauw, H. Feuchtgruber, and M. F. Kessler. *A&A*, 336: L85, 1998.

A. Crapsi, P. Caselli, C. M. Walmsley, P. C. Myers, M. Tafalla, C. W. Lee, and T. L. Bourke. *ApJ*, 619:379, 2005.

T. de Jong. *A&A*, 55:137, 1977.

T. de Jong, W. Boland, and A. Dalgarno. *A&A*, 91:68, 1980.

S. D. Doty, S. E. Everett, Y. L. Shirley, N. J. Evans, and M. L. Palotti. *MNRAS*, 359:228, 2005.

B. T. Draine. *ApJS*, 36:595, 1978.

B. T. Draine and F. Bertoldi. *ApJ*, 468:269, 1996.

M. Elitzur and T. de Jong. *A&A*, 67:323, 1978.

A. Faure, N. Crimier, C. Ceccarelli, P. Valiron, L. Wiesenfeld, and M. L. Dubernet. *A&A*, 472:1029, 2007.

S. R. Federman, A. E. Glassgold, and J. Kwan. *ApJ*, 227:466, 1979.

G. J. Ferland, K. T. Korista, D. A. Verner, J. W. Ferguson, J. B. Kingdon, and E. M. Verner. *PASP*, 110:761, 1998.

H. Feuchtgruber, E. Lellouch, T. de Graauw, B. Bezard, T. Encrenaz, and M. Griffin. *Nature*, 389:159, 1997.

G. B. Field, W. B. Somerville, and K. Dressler. *Ann. Rev. Astron. Astrophys.*, 4:207, 1966.

D. Flower. *Molecular Collisions in the Interstellar Medium*, chapter 7. Cambridge University Press, Cambridge, 2007.

D. R. Flower, G. Pineau Des Forêts, and C. M. Walmsley. *A&A*, 436:933, 2005.

D. R. Flower, G. Pineau Des Forêts, and C. M. Walmsley. *A&A*, 456:215, 2006.

A. Fuente, J. Martin-Pintado, J. Cernicharo, and R. Bachiller. *A&A*, 276: 473, 1993.

A. Fuente, S. García-Burillo, M. Gerin, D. Teyssier, A. Usero, J. R. Rizzo, and P. de Vicente. *ApJ*, 619:L155, 2005.

Viala Y. Gerin, M. and F. Casoli. *A&A*, 268:212, 1993.

Viala Y. Pauzat F. Gerin, M. and Y. Ellinger. *A&A*, 266:463, 1992.

P. F. Goldsmith and D. Li. *ApJ*, 622:938, 2005.

P. F. Goldsmith, D. Li, and M. Krco. *ApJ*, 654:273, 2007.

R. J. Gould and E. E. Salpeter. *ApJ*, 138:393, 1963.

C. Gry, F. Boulanger, C. Nehmé, G. Pineau des Forêts, E. Habart, and E. Falgarone. *A&A*, 391:675, 2002.

E. Habart, F. Boulanger, L. Verstraete, C. M. Walmsley, and G. Pineau des Forêts. *A&A*, 414:531, 2004.

H. J. Habing. *Bull. Astron. Inst. Netherlands*, 19:421, 1968.

E. L. Heck, D. R. Flower, J. Le Bourlot, G. Pineau des Forets, and E. Roueff. *MNRAS*, 258:377, 1992.

W. J. Henney, S. J. Arthur, R. J. R. Williams, and G. J. Ferland. *ApJ*, 621: 328, 2005.

W. J. Henney, R. J. R. Williams, G. J. Ferland, G. Shaw, and C. R. O'Dell. *ApJ*, 671:L137, 2007.

J. K. Hill and D. J. Hollenbach. *ApJ*, 225:390, 1978.

P. Hily-Blant, M. Walmsley, G. Pineau Des Forêts, and D. Flower. *A&A*, 480:L5, 2008.

D. J. Hollenbach and A. G. G. M. Tielens. *Rev. Mod. Phys.*, 71:173, 1999.

D. J. Hollenbach, T. Takahashi, and A. G. G. M. Tielens. *ApJ*, 377:192, 1991.

D. J. Jansen, E. F. van Dishoeck, J. H. Black, M. Spaans, and C. Sosin. *A&A*, 302:223, 1995.

M. Jura. *ApJ*, 191:375, 1974.

M. Jura. *ApJ*, 197:575, 1975.

I. Kamp and F. Bertoldi. *A&A*, 353:276, 2000.

I. Kamp and G.-J. van Zadelhoff. *A&A*, 373:641, 2001.

M. J. Kaufman, M. G. Wolfire, D. J. Hollenbach, and M. L. Luhman. *ApJ*, 527:795, 1999.

R. F. Knacke, H. P. Larson, and K. S. Noll. *ApJ*, 335:L27, 1988.

B. Köster, H. Störzer, J. Stutzki, and A. Sternberg. *A&A*, 284:545, 1994.

J. Le Bourlot, G. Pineau Des Forets, E. Roueff, and D. R. Flower. *A&A*, 267:233, 1993.

J. Le Bourlot, G. Pineau des Forets, E. Roueff, A. Dalgarno, and R. Gredel. *ApJ*, 449:178, 1995.

F. Le Petit, E. Roueff, and J. Le Bourlot. *A&A*, 390:369, 2002.

F. Le Petit, C. Nehmé, J. Le Bourlot, and E. Roueff. *ApJS*, 164:506, 2006.

H.-H. Lee, E. Herbst, G. Pineau des Forets, E. Roueff, and J. Le Bourlot. *A&A*, 311:690, 1996.

S. Lepp and A. Dalgarno. *ApJ*, 335:769, 1988.

R. London. *ApJ*, 225:405, 1978.

C. F. McKee and J. P. Ostriker. *ApJ*, 218:148, 1977.

R. Meijerink and M. Spaans. *A&A*, 436:397, 2005.

G. Melnick, G. E. Gull, and M. Harwit. *ApJ*, 227:L29, 1979.

G. J. Melnick and E. A. Bergin. *AdSpR*, 36:1027, 2005.

D. A. Neufeld, S. Lepp, and G. J. Melnick. *ApJS*, 100:132, 1995.

D. A. Neufeld, H. Feuchtgruber, M. Harwit, and G. J. Melnick. *ApJ*, 517: L147, 1999.

van Broekhuizen F. Fraser H. J. Bisschop S. E. van Dishoeck E. F. Öberg, K. I. and S. Schlemmer. *ApJ*, 621:L33, 2005.

A. R. Offer and E. F. van Dishoeck. *MNRAS*, 257:377, 1992.

D.E. Osterbrock and G.F. Ferland. *Astrophysics of Gaseous Nebulae and Active Galactic Nuclei*, chapter 8. University Science Books, USA, 2006.

L. Pagani, A. O. H. Olofsson, P. Bergman, P. Bernath, J. H. Black, R. S. Booth, V. Buat, J. Crovisier, C. L. Curry, P. J. Encrenaz, E. Falgarone, P. A. Feldman, M. Fich, H. G. Floren, U. Frisk, M. Gerin, E. M. Gregersen, J. Harju, T. Hasegawa, Å. Hjalmarson, L. E. B. Johansson, S. Kwok, B. Larsson, A. Lecacheux, T. Liljeström, M. Lindqvist, R. Liseau, K. Mattila, G. F. Mitchell, L. H. Nordh, M. Olberg, G. Olofsson, I. Ristorcelli, A. Sandqvist, F. von Scheele, G. Serra, N. F. Tothill, K. Volk, T. Wiklind, and C. D. Wilson. *A&A*, 402:L77, 2003.

L. Pagani, A. Bacmann, F. Motte, L. Cambrésy, M. Fich, G. Lagache, M.-A. Miville-Deschênes, J.-R. Pardo, and A. J. Apponi. *A&A*, 417:605, 2004.

L. Pagani, J.-R. Pardo, A. J. Apponi, A. Bacmann, and S. Cabrit. *A&A*, 429:181, 2005.

L. Pagani, A. Bacmann, S. Cabrit, and C. Vastel. *A&A*, 467:179, 2007.

P. P. Papadopoulos, W.-F. Thi, and S. Viti. *ApJ*, 579:270, 2002.

D. R. Poelman and M. Spaans. *A&A*, 440:559, 2005.

D. R. Poelman and M. Spaans. *A&A*, 453:615, 2006.

S. S. Prasad and S. P. Tarafdar. *ApJ*, 267:603, 1983.

J. L. Puget and A. Leger. *ARA&A*, 27:161, 1989.

W.G. Roberge. *Molecular Astrophysics.* Cambridge University Press, Cambridge, UK, 1990.

H. Roberts and E. Herbst. *A&A*, 395:233, 2002.

M. Röllig, N. P. Abel, T. Bell, F. Bensch, J. Black, G. J. Ferland, B. Jonkheid, I. Kamp, M. J. Kaufman, J. Le Bourlot, F. Le Petit, R. Meijerink, O. Morata, V. Ossenkopf, E. Roueff, G. Shaw, M. Spaans, A. Sternberg, J. Stutzki, W.-F. Thi, E. F. van Dishoeck, P. A. M. van Hoof, S. Viti, and M. G. Wolfire. *A&A*, 467:187, 2007.

R. W. Russell, G. Melnick, G. E. Gull, and M. Harwit. *ApJ*, 240:L99, 1980.

R. W. Russell, G. Melnick, S. D. Smyers, N. T. Kurtz, T. R. Gosnell, M. Harwit, and M. W. Werner. *ApJ*, 250:L35, 1981.

C. Savage and L. M. Ziurys. *ApJ*, 616:966, 2004.

G. Shaw, G. J. Ferland, N. P. Abel, P. C. Stancil, and P. A. M. van Hoof. *ApJ*, 624:794, 2005.

J. M. Shull. *ApJ*, 219:877, 1978.

R. L. Snell, J. E. Howe, M. L. N. Ashby, E. A. Bergin, G. Chin, N. R. Erickson, P. F. Goldsmith, M. Harwit, S. C. Kleiner, D. G. Koch, D. A. Neufeld, B. M. Patten, R. Plume, R. Schieder, J. R. Stauffer, V. Tolls, Z. Wang, G. Winnewisser, Y. F. Zhang, and G. J. Melnick. *ApJ*, 539: L101, 2000.

M. Spaans and E. F. van Dishoeck. *ApJ*, 548:L217, 2001.

L. Spitzer. *Physical Processes in the Interstellar Medium*, chapter 4. John Wiley & Sons, Canada, 1978.

T. P. Stecher and D. A. Williams. *ApJ Letters*, 149:L29, 1967.

A. Sternberg and A. Dalgarno. *ApJS*, 99:565, 1995.

A. Sternberg and D. A. Neufeld. *ApJ*, 516:371, 1999.

J. W. V. Storey, D. M. Watson, and C. H. Townes. *ApJ*, 233:109, 1979.

H. Störzer and D. Hollenbach. *ApJ*, 495:853, 1998.

H. Störzer, J. Stutzki, and A. Sternberg. *A&A*, 310:592, 1996.

D. A. Swade. *ApJ*, 345:828, 1989.

M. Tafalla, P. C. Myers, P. Caselli, C. M. Walmsley, and C. Comito. *ApJ*, 569:815, 2002.

J. Tauber, G. Olofsson, G. Pilbratt, L. Nordh, and U. Frisk. *A&A*, 308:913, 1996.

S. D. Taylor, T. W. Hartquist, and D. A. Williams. *MNRAS*, 264:929, 1993.

D. Teyssier, D. Fossé, M. Gerin, J. Pety, A. Abergel, and E. Roueff. *A&A*, 417:135, 2004.

A. G. G. M. Tielens and D. Hollenbach. *ApJ*, 291:722, 1985.

A.G.G.M. Tielens. *The Physics and the Chemistry of the Interstellar Medium*, chapter 2. Cambridge University Press, Cambridge, 2005.

T. Tsuji. *ApJ*, 540:L99, 2000.

T. Tsuji. *A&A*, 376:L1, 2001.

J. Tumlinson, J. M. Shull, B. L. Rachford, M. K. Browning, T. P. Snow, A. W. Fullerton, E. B. Jenkins, B. D. Savage, P. A. Crowther, H. W. Moos, K. R. Sembach, G. Sonneborn, and D. G. York. *ApJ*, 566:857, 2002.

H. Ungerechts, C. M. Walmsley, and G. Winnewisser. *A&A*, 88:259, 1980.

E. F. van Dishoeck and J. H. Black. *ApJ*, 334:771, 1988.

E. F. van Dishoeck and J. H. Black. *ApJS*, 62:109, 1986.

E.F. van Dishoeck. *IAUS*, 120:51V, 1987.

P. A. M. van Hoof, J. C. Weingartner, P. G. Martin, K. Volk, and G. J. Ferland. *MNRAS*, 350:1330, 2004.

L. Verstraete, J. L. Puget, E. Falgarone, S. Drapatz, C. M. Wright, and R. Timmermann. *A&A*, 315:L337, 1996.

Y. P. Viala, E. Roueff, and H. Abgrall. *A&A*, 190:215, 1988.

C. M. Walmsley, G. Winnewisser, and F. Toelle. *A&A*, 81:245, 1980.

C. M. Walmsley, G. Pineau des Forêts, and D. R. Flower. *A&A*, 342:542, 1999.

W. D. Watson. *ApJ*, 176:103, 1972.

M. S. Westley, R. A. Baragiola, R. E. Johnson, and G. A. Baratta. *Nature*, 373:405, 1995.

M. G. Wolfire, A. G. G. M. Tielens, and D. Hollenbach. *ApJ*, 358:116, 1990.

C. M. Wright, E. F. van Dishoeck, J. H. Black, H. Feuchtgruber, J. Cernicharo, E. González-Alfonso, and T. de Graauw. *A&A*, 358:689, 2000.

M. Zielinsky, J. Stutzki, and H. Störzer. *A&A*, 358:723, 2000.